Advances in actuation techniques for wind farm flow control

van der Hoek, D.C.

DOI
10.4233/uuid:56cadf8e-cc7f-4f7b-b6b0-696dd4ecb65d

Publication date
2023

Document Version
Final published version

Citation (APA)
van der Hoek, D. C. (2023). *Advances in actuation techniques for wind farm flow control*. [Dissertation (TU Delft), Delft University of Technology]. https://doi.org/10.4233/uuid:56cadf8e-cc7f-4f7b-b6b0-696dd4ecb65d

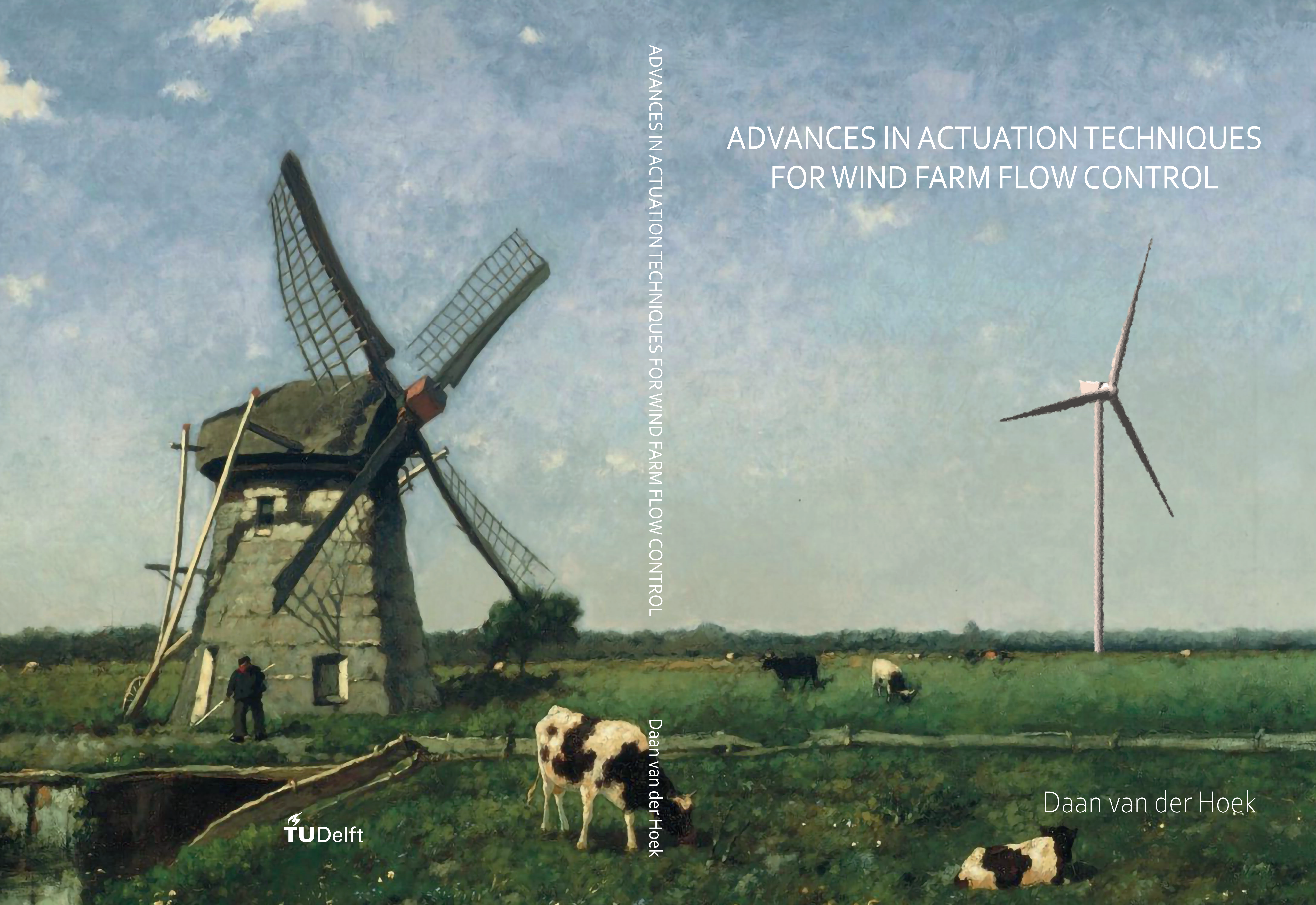

ADVANCES IN ACTUATION TECHNIQUES FOR WIND FARM FLOW CONTROL

Daan van der Hoek

ADVANCES IN ACTUATION TECHNIQUES FOR WIND FARM FLOW CONTROL

Daan van der Hoek

TU Delft

Advances in actuation techniques for wind farm flow control

Advances in actuation techniques for wind farm flow control

Proefschrift

ter verkrijging van de graad van doctor
aan de Technische Universiteit Delft,
op gezag van de Rector Magnificus prof. dr. ir. T.H.J.J. van der Hagen,
voorzitter van het College voor Promoties,
in het openbaar te verdedigen
op vrijdag 24 november 2023 om 12.30 uur

door

Daan Cornelis VAN DER HOEK

Ingenieur in de systeem- en regeltechniek,
Technische Universiteit Delft, Nederland,
geboren te Rotterdam, Nederland.

Dit proefschrift is goedgekeurd door de promotoren:

Prof. dr. ir. J.W. van Wingerden
Prof. dr. ir. C.J. Simão Ferreira

Samenstelling promotiecommissie:

Rector Magnificus,	voorzitter
Prof. dr. ir. J.W. van Wingerden,	Technische Universiteit Delft
Prof. dr. ir. C.J. Simão Ferreira,	Technische Universiteit Delft
Onafhankelijke leden:	
Prof. dr. M. Kühn,	Carl von Ossietzky Universität Oldenburg, Duitsland
Prof. dr. S. Ivanell,	Uppsala Universitet, Zweden
Prof. dr. ir. A.C. Viré,	Technische Universiteit Delft
Dr. ir. R.J.A.M. Stevens,	Universiteit Twente
Dr. ir. A. Sciacchitano,	Technische Universiteit Delft
Prof. dr. ir. B. de Schutter,	Technische Universiteit Delft, reservelid

Keywords: Wind farm flow control, wind farm power maximization, static induction control, wake mixing control, wake steering control, helix approach, wind tunnel experiments, particle image velocimetry

Printed by: Gildeprint

Cover: Original painting by Johan Hendrik Weissenbruch - Landscape with windmill near Schiedam

Style: TU Delft House Style, with modifications by Moritz Beller
`https://github.com/Inventitech/phd-thesis-template`

ISBN 978-94-6366-765-4

An electronic version of this dissertation is available at
`http://repository.tudelft.nl/`.

Voor Jules en Lou

Summary

Following the rise in global surface temperature, we are already witnessing dramatic effects caused by climate change. In an attempt to avert the impact of climate change, immediate action is required to reduce greenhouse gas emissions and limit the rise in surface temperature to 2 °C. This can be largely achieved by transitioning to renewable energy sources such as wind energy. However, transitioning to a fully sustainable energy supply is mostly hampered by financial aspects. The relatively low cost of carbon-based energy sources has made it difficult for wind energy to compete. Although recent years have seen a significant decrease in costs, further reductions are required to accelerate wind energy growth.

For economic motives, offshore wind farms are generally installed in densely spaced clusters. The small distances between turbines introduce significant losses from turbine wakes. Typical energy losses are estimated to be in the order of 10%. These low wind speed zones can be partially mitigated by enabling wind farm flow control, thereby increasing the wind farm's overall efficiency. The annual increase in energy production is generally estimated to be in the order of 1%. Consequently, a reduction in the cost of energy is achieved.

Wind farm flow control can be divided into three categories: static induction control (SIC), wake steering control (WSC), and wake mixing control (WMC). With SIC, upstream turbines are derated to create higher-velocity wakes. The losses that are incurred by derating are subsequently compensated by downstream turbines. WSC redirects the wake away from downstream turbines by misaligning a turbine with respect to the incoming wind direction. Using WMC, the wake mixing process is enhanced by continuously adjusting the operating conditions of the wind turbine. Generally, this is achieved through a periodic pitching motion of the blades. Hence, this method is often referred to as dynamic induction control (DIC).

The goal of this thesis is to *advance the state of the art of wind farm flow control techniques for maximizing wind farm power performance.* The state of the art was determined from literature based on the Technology Readiness Level of each method. Four research objectives were specified to fill the knowledge gaps that were revealed.

First, the potential of pitch-actuated static induction control for improving wind farm power efficiency was examined in a field test. While previous simulation studies and wind tunnel experiments have indicated that SIC can increase a wind farm's power output, field tests have so far been inconclusive. The field test presented in this thesis was carried out at an onshore commercial wind farm with very small turbine spacing. SIC was implemented by introducing a pitch angle offset at the most upstream wind turbines for a predetermined set of ambient conditions. After filtering and correcting the measurement data, an increase in the power production of 3.3% was observed in case of full wake interaction and below-rated wind speeds. Furthermore, measurements of the turbulence intensity at the downstream turbines indicated a decrease in structural loading when SIC was activated.

The second research objective considered the effect of wind direction variations on the estimated increase in Annual Energy Production (AEP) with wake steering control. The AEP benefit with wake steering is generally estimated using analytical steady-state models. This type of model casts a large degree of uncertainty on the actual benefit. To overcome this uncertainty, a framework was developed that incorporates both simulation results from an analytical model and large eddy simulations. Simulations of an existing offshore wind farm were carried out with time-varying wind directions to obtain a realistic representation of the ambient conditions at the wind farm site. Using Gaussian process regression, data from the two modeling approaches were combined into a single model. This model showed a 0.60% gain in AEP for the considered wind farm, which is a 76% increase compared to the estimate of the analytical model.

Next, the mechanism responsible for the accelerated wake breakdown when applying periodic dynamic induction control was investigated. The wake recovery properties of DIC have previously been validated in wind tunnel studies. However, the wake itself has not been studied extensively before. Three-dimensional Particle Image Velocimetry (PIV) was used to obtain the time-resolved wake of a turbine operating with periodic pitch excitation. The measured velocity fields showed increased levels of energy in the wake. While this increase was partially due to a lower operational thrust force with DIC, it was significantly higher than estimated by actuator disk theory. The role of tip vortex breakdown in the wake recovery process was also investigated. As these vortices become unstable and start interacting with each other, the wake is no longer shielded and energy is entrained from the surrounding flow. With DIC, the location of the tip vortex breakdown was observed to shift over time, resulting in an overall faster recovery of the wake.

Finally, a second wake mixing control strategy incorporating dynamic individual pitch control (the helix approach) was validated in a wind tunnel experiment. Using individual pitch control, the helix approach induces a helical velocity profile in the turbine wake, which has turned out to be very effective for wind farm power maximization, according to simulations. The effect of the helix approach was measured using two aligned turbines, of which the upstream was actuated using a swashplate. Tomographic PIV was used to study the wake itself. The enhanced wake recovery of the helix approach was confirmed by the measured flow fields. Similar to periodic dynamic induction control, the breakdown of blade tip vortices was observed to play an important part in the wake re-energizing process. Additionally, turbine measurements showed that the helix approach was able to increase the combined power for this particular two-turbine setup by as much as 15%.

This thesis contributed to the development of four different wind farm flow control methods that aim to maximize power performance. Each of the considered methods has both positive and negative aspects. When applying any of the wind farm flow control methods, one has to consider aspects such as the wind farm layout, ambient conditions, and wind turbine structural loads. Ideally, multiple methods should be combined to counter some of the negative aspects, while still realizing an increase in power performance. Not only can wind farm flow control increase the overall efficiency of existing wind farms, but it also offers additional degrees of freedom when considered during the design of new ones.

Samenvatting

Door de stijging van de wereldwijde oppervlaktetemperatuur worden de vergaande gevolgen van klimaatverandering steeds zichtbaarder. Om de impact van klimaatverandering te minimaliseren is onmiddellijke actie vereist. Door de uitstoot van broeikasgassen te verminderen kan de stijging van de oppervlaktetemperatuur beperkt worden tot 2 °C. Dit kan grotendeels worden bereikt door over te stappen naar duurzame energiebronnen, zoals windenergie. Het volledig overgaan naar een duurzame energievoorziening wordt voornamelijk gehinderd door financiële aspecten. De relatief lage kosten van op koolstof gebaseerde energiebronnen maken het moeilijk voor windenergie om hiertegen te concurreren. Hoewel de kosten van windenergie de afgelopen jaren aanzienlijk zijn gedaald, zijn verdere verlagingen van de energiekosten nodig om de groei van windenergie te versnellen.

Vanwege economische motieven worden offshore windturbines over het algemeen geïnstalleerd in windparken waarin de turbines dicht op elkaar gegroepeerd zijn. De kleine afstanden tussen de windturbines leiden tot aanzienlijke energieverliezen als gevolg van zogenaamde ‘zogeffecten’. Deze energieverliezen worden geschat op ongeveer 10% van de potentiële energieproductie. Zones met lage windsnelheden kunnen gedeeltelijk worden verminderd door gebruik te maken van windparkstromingsregeling. Dit zorgt ervoor dat de algehele efficiëntie van het windpark wordt verhoogd. De jaarlijkse toename in energieproductie van een windpark met deze techniek wordt over het algemeen geschat op ongeveer 1%, dit met een verlaging van de energiekosten als gevolg.

Windparkstromingsregeling kan worden onderverdeeld in drie categorieën: statische inductieregeling, zogsturing en zogmengingsregeling. Met statische inductieregeling wordt de energieopwekking van stroomopwaarts gepositioneerde windturbines gereduceerd om zoggen met hogere windsnelheid te creëren. De verliezen die worden geleden door het verminderen van de energieopwekking worden gecompenseerd door stroomafwaarts gepositioneerde windturbines. Zogsturing stuurt het zog weg van stroomafwaarts gepositioneerde windturbines door bij stroomopwaarts gepositioneerde windturbines een scheefstand ten opzichte van de inkomende windrichting in te stellen. Met behulp van zogmengingsregeling wordt het zogmengingsproces versneld door continu de regelaar van de windturbine aan te passen. Doorgaans wordt dit bereikt door de bladhoeken periodiek bij te stellen. Deze methode wordt dan ook ook vaak aangeduid als dynamische inductieregeling.

Het doel van deze thesis is het *bevorderen van de ontwikkeling van de laatste windparkstromingsregelingstechnieken, met als doel om de energieopbrengst van windparken te maximaliseren.* De huidige stand van de technologie is bepaald door middel van literatuuronderzoek aan de hand van het zogeheten Technology Readiness Level. Om de gevonden kenniskloven te dichten zijn vier onderzoeksdoelen geformuleerd.

Allereerst is in een veldtest onderzocht wat het potentieel is van statische inductieregeling met bladhoekverandering voor het verhogen van de energieopbrengst van een wind-

park. Hoewel eerdere simulatiestudies en windtunneltesten hebben aangetoond dat statische inductieregeling in staat is om de energieproductie van een windpark te verhogen, hebben veldtesten tot nu toe geen overtuigende resultaten laten zien. Het veldexperiment dat in deze thesis wordt gepresenteerd is uitgevoerd op een onshore windpark met zeer kleine afstanden tussen windturbines. Statische inductieregeling werd geïmplementeerd door een afwijking in de bladhoek in te stellen bij de meest stroomopwaarts gepositioneerde windturbines onder bepaalde omgevingsomstandigheden. Na het filteren en corrigeren van de meetgegevens werd een toename in de energieproductie van 3,3% waargenomen in geval van volledige zoginteractie en bij windsnelheden onder het nominale niveau van de windturbine. Bovendien toonden de metingen aan dat de turbulentie-intensiteit rondom de stroomafwaarts gepositioneerde windturbines afnam wanneer statische inductieregeling actief was, met als gevolg een verlaging van de structurele belastingen.

Het tweede onderzoeksdoel betrof het effect van variaties in windrichting op de geschatte toename van de jaarlijkse energieproductie als gevolg van zogsturing. De energietoename met zogsturing wordt over het algemeen geschat met behulp van analytische stabiele-toestandsmodellen. Dit soort modellen brengt een grote mate van onzekerheid met zich mee over de daadwerkelijke energietoename. Om deze onzekerheid te verminderen is een raamwerk ontwikkeld dat zowel simulatieresultaten van een analytisch model als ‘large eddy simulaties’ omvat. Simulaties van een bestaand offshore windpark werden uitgevoerd met tijdsvariërende windrichtingen om realistische omgevingsomstandigheden op de locatie van het windpark na te bootsen. Met behulp van ‘Gaussian process’-regressie werden gegevens van de twee modelleringsbenaderingen gecombineerd in één model. Dit model toonde een toename van 0.60% in de geschatte jaarlijkse energieproductie van het betreffende windpark. Dit is een verhoging van 76% in vergelijking met de schatting van het analytische model.

Vervolgens werd het mechanisme achter periodieke dynamische inductieregeling onderzocht dat verantwoordelijk is voor een versnelde afbraak van het zog. De zogherstellende eigenschappen van dynamische inductieregeling zijn eerder gevalideerd in een windtunnelexperiment. Het zog zelf is echter nog niet eerder uitgebreid bestudeerd. Aan de hand van deeltjesbeeldsnelheidsmetingen werd een driedimensionaal tijdsvariërende meting verkregen van het zog van een windturbine die met periodiek variërende bladhoeken werd aangestuurd. De gemeten snelheidsvelden lieten verhoogde energieniveaus in het zog zien. Deze toename was deels te wijten aan een lagere operationele stuwkracht bij dynamische inductieregeling. Toch was deze toename aanzienlijk hoger dan geschat aan de hand van remmende schijf theorie. De rol van tipwervels in het herstelproces van het zog werd ook onderzocht. Naarmate deze wervels instabiel worden en op elkaar in beginnen te werken, schermen ze het zog niet langer af en kan er energie uit de omringende stroming worden meegevoerd. Bij het gebruik van dynamische inductieregeling werd waargenomen dat de locatie van de tipwervel-afbraak in de loop der tijd verschuift, wat resulteert in een algeheel sneller herstel van het zog.

Ten slotte werd een tweede strategie voor zogmengingsregeling met dynamische individuele bladhoekveranderingen (de helixbenadering) gevalideerd in een windtunnelexperiment. Met individuele bladhoekregeling wordt de helixbenadering gebruikt om een helixvormig snelheidsprofiel in het zog van de windturbine te genereren. Dit is volgens simulaties zeer effectief in het verhogen van de energieopwekking van een windpark. Het

effect van de helixbenadering werd gemeten met behulp van twee uitgelijnde windturbines, waarvan de stroomopwaarts gepositioneerde turbine werd aangestuurd met behulp van een tuimelschijf. Tomografische deeltjesbeeldsnelheidsmetingen werden gebruikt om het zog te bestuderen. Het verbeterde zogherstel van de helixbenadering werd bevestigd door de gemeten stromingsvelden. Net als bij periodieke dynamische inductieregeling werd waargenomen dat de afbraak van bladtipwervels een belangrijke rol speelt in het zogherstelproces. Bovendien toonden vermogensmetingen van de windturbines aan dat de helixbenadering in staat was om het gecombineerde vermogen van deze specifieke opstelling met wel 15% te verhogen.

Deze thesis heeft bijgedragen aan de verdere ontwikkeling van vier verschillende methoden voor windparkstromingsregeling die tot doel hebben de vermogensprestaties van een windpark te maximaliseren. Elke van de overwogen methoden heeft zowel positieve als negatieve aspecten. Bij de keuze van welk van de methoden voor windparkstromingsregeling toe te passen, moeten aspecten, zoals de lay-out van het windpark, omgevingsomstandigheden en structurele belastingen van de windturbines overwogen worden. Idealiter zouden meerdere methoden gecombineerd moeten worden om enkele van de negatieve aspecten tegen te gaan, waarbij een verhoging van de vermogensprestaties behouden blijft. Windparkstromingsregeling kan niet alleen de algehele efficiëntie van bestaande windparken verhogen, maar biedt ook extra graden van vrijheid bij het ontwerp van toekomstige windparken.

Contents

1

Introduction

1.1 The global rise in temperature

Humanity's impact on the environment is becoming clearer each day, with the effects of climate change visible all around us. Recent years saw an increase in severe heat waves across Europe, with increased drought as a result (Lhotka and Kyselý, 2022). At the same time, the chances of heavy rainfall with the consequence of flooding are increasing (World Weather Attribution, 2021). Furthermore, glaciers are shrinking rapidly, impacting water resources and local ecosystems, as well as increasing the risk of flooding (Sommer et al., 2020). These are just a few examples for which the main driver is the rise in global surface temperature since pre-industrial times, as visualized in Figure 1.1.

There exists a clear correlation between increasing surface temperatures and the emission of greenhouse gasses (Stips et al., 2016). When these greenhouse gasses are released into Earth's atmosphere, for example in the process of burning fossil fuels, they trap the heat that is generated by the sun, gradually warming up the planet. The ever-increasing global population also implies that greenhouse gas emissions, and consequently the global surface temperature, will continue to rise if no action is taken to prevent this.

To limit the impact of global warming on climate change, the Paris Agreement was signed at the UN's Climate Change Conference in 2015. As part of this agreement, 196 countries pledged their contribution to a combined effort to limit the rise in global average surface temperature to well below 2 °C above pre-industrial levels, and preferably limited to 1.5 °C (United Nations, 2015). Under these thresholds, it is believed that the worst impacts of global warming on climate change can be prevented and that Earth's climate is not irreversibly damaged (IPCC, 2022).

Limiting the increase in temperature depends on reducing the emission of greenhouse gasses, of which carbon dioxide (CO2) is the primary culprit. The most recent report from the Intergovernmental Panel on Climate Change (IPCC) projects the rise in temperature for different future trajectories in the emission of greenhouse gasses (IPCC, 2023). Examples of these trajectories based on the emission of CO2 are provided in Figure 1.1. The trajectories show the estimated changes in temperature for different Shared Socioeconomic Pathways (SSPs). This figure illustrates that even for the most ambitious pathway, which requires net zero carbon emissions around the year 2050, the average temperature

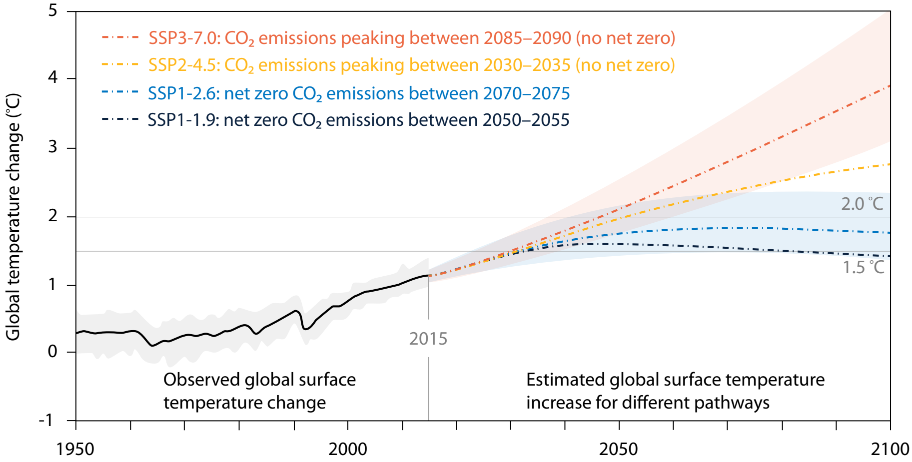

Figure 1.1: Observed and estimated global surface temperature changes. The estimated temperature increase for the remainder of this century is expressed by different Shared Socioeconomic Pathways, which are ranked by the amount of effort they require to reduce greenhouse gas emissions. Two of the pathways include confidence bounds, expressed by the shaded areas, which represent the uncertainties in current climate models, and the effect of certain policies on temperature rise. This figure is based on Figure SPM.3a from the AR6 Synthesis Report (IPCC, 2023).

will have increased by more than 1.5 °C by 2030. After the temperature has peaked it will slowly settle below 1.5 °C. Recent research incorporating a machine learning approach even suggests that the estimates from the IPCC underpredict the increasing temperature and that the SSP1-2.6 pathway has a high probability of crossing the 2 °C limit (Diffenbaugh and Barnes, 2023).

Besides providing the most recent estimates on the global temperature increase, the IPCC AR6 Synthesis report also indicated that the effect of these temperature changes has previously been underestimated. Compared to a similar report from 2014 (IPCC, 2014), the risk of adverse consequences on threatened ecosystems, extreme weather events, and large-scale singular events, among others, has increased for similar temperature changes. This means that a 1.5 °C increase in temperature will have an even larger impact than previously estimated.

The previous statements indicate just how dire the current situation is and that we are quickly approaching a point of no return. However, the IPCC report also showed that by taking appropriate action, we can still limit the global temperature increase to the target limit of 1.5 °C. A large part of the solution requires the transition from a carbon-based energy system to a low-carbon alternative driven by renewable energy sources such as solar and wind.

Earth has enough wind resources to meet the global electricity demand many times over (Eurek et al., 2017). Therefore, wind energy will play a pivotal role alongside solar energy in reducing CO2 emissions over the next decades. To reach the net zero emission scenario by 2050, the International Energy Agency estimates that wind energy generation needs to reach approximately 8,000 TWh by 2030 (IEA, 2022). Figure 1.2 presents the past

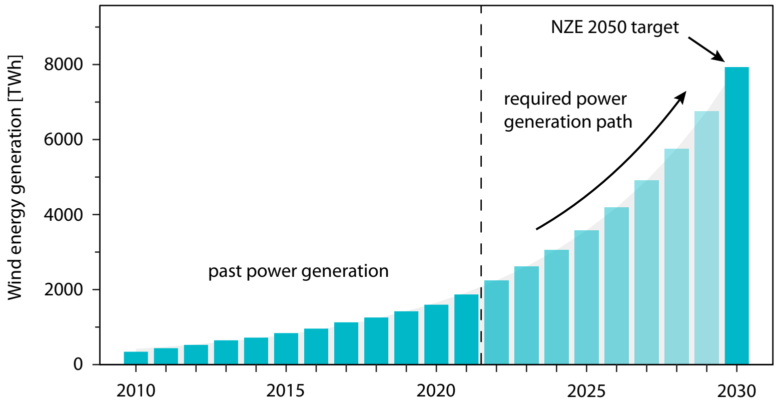

Figure 1.2: Required growth in wind power generation over the next decade, to reach Net Zero Emissions by 2050. Starting from 2022, a quadrupling of power generated by wind turbines is necessary in a period of nine years. Data for this figure was taken from IEA (2022).

and current wind energy generation, and how this relates to the 2030 target. The figure shows just how big of a challenge we face, given that wind power generation is required to quadruple within a period of just nine years.

1.2 Wind energy

The practice of harnessing energy from the wind goes back thousands of years to ancient civilizations that used windmills to grind grain or pump water. The first wind turbines appeared at the end of the nineteenth century, with most notable the designs from Brush and la Cour. Over the next century, wind turbine development continued and halted alongside the rise and fall of the oil price, with the largest resurgence taking place in the 1970s during multiple oil crises. As the oil supply returned to normal following these crises, public interest in wind energy as a viable energy source diminished once more. However, the development of various wind turbine concepts continued over the next decades. With climate concerns becoming more prominent by the end of the 20th century, wind energy saw a renewed interest as a means to reduce greenhouse gas emissions (UNFCCC, 1997).

1.2.1 Modern wind turbine and its degrees of freedom

Most modern commercial wind turbines are based on the upwind, three-bladed Danish design (Burton et al., 2001). Figure 1.3 illustrates the main components of such a wind turbine along with its actuation degrees of freedom. The wind turbine consists of a nacelle, tower, and blades. The nacelle houses the generator that converts kinetic energy into electricity. A main shaft connects the generator, optionally through a gearbox, to the hub. The latter houses the three blades, each consisting of multiple airfoil sections of varying cord length and thickness. The area that is covered by the blades over a full rotation is referred to as the rotor surface.

Wind turbines are generally operated at variable speeds to extract maximum power

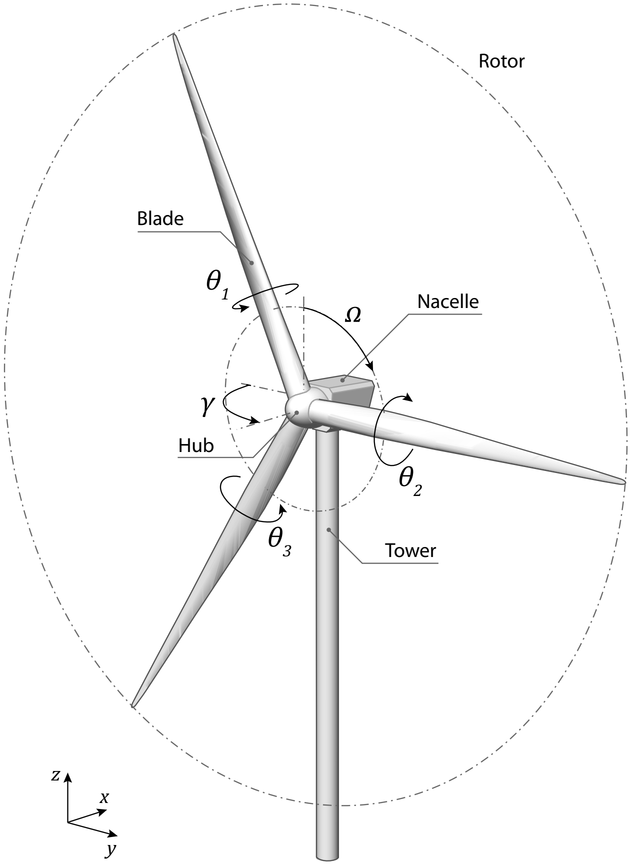

Figure 1.3: Illustration of a modern wind turbine with some of its main components. The figure indicates the different degrees of freedom the turbine has available for actuation, which are rotor speed control (Ω), (individual) blade pitch control (θ_i), and yaw control (γ).

from the wind. To achieve this, the rotor speed can either be regulated by adjusting the counter torque of the generator, or by adjusting the blades' angle of attack to reduce the aerodynamic torque exerted on the turbine. The latter is achieved through three pitch motors that are fitted inside the hub, allowing the turbine to pitch each blade individually. Besides the pitch motors, turbines are equipped with a yaw motor that connects the nacelle to the tower, allowing the turbine rotor to change its orientation and match the incoming wind direction.

Depending on the atmospheric conditions, turbines operate in different control regions, as is visualized in Figure 1.4. At low wind speeds, the turbine can rotate freely, but the generator does not give any counter torque, and hence no power is generated. Above a specific cut-in wind speed, the torque controller is activated and power production is initiated. As the wind speed increases, the generator torque is controlled in such a way that the optimal aerodynamic power is tracked. This optimal aerodynamic power is a function

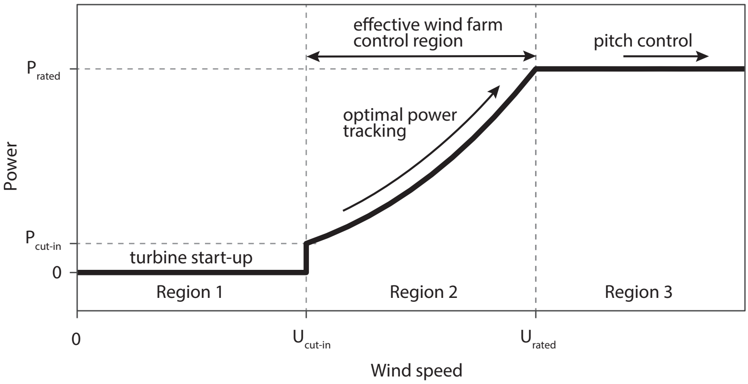

Figure 1.4: Graphical overview of a wind turbine's operating regions. At wind speeds below cut-in (region 1), the turbine is idling. When the wind speed is sufficiently high, optimal power tracking is employed to maximize the energy that can be extracted from the wind (region 2). Once the turbine is operating at rated power, pitch control is activated to regulate power and rotor speed at rated conditions (region 3).

of the pitch angle θ (°), and the dimensionless tip-speed ratio λ. The latter is defined as $\lambda = \Omega R/U_\infty$, with rotor speed Ω ($\mathrm{rad\,s^{-1}}$), rotor radius R (m), and inflow velocity U_∞ ($\mathrm{m\,s^{-1}}$). As a result, the rotational speed of the turbine varies as the atmospheric conditions change. Once the turbine reaches its maximum (rated) power production, the generator torque is held constant and blade pitch control is used to regulate the rotor speed and hence the generator output. At excessively high wind speeds, the blades are pitched completely and the turbine is put to a halt to protect it from high structural loads.

1.2.2 Offshore wind energy and the wake effect

Wind energy development initially focused on maturing onshore wind turbine designs to make them more cost-effective. By reducing the costs of energy, wind power could be seen as a viable alternative to fossil fuel-based energy sources. In this way, besides having a beneficial impact on the environment, it is also an economically attractive alternative. The most straightforward way to do so is by increasing the dimensions of a wind turbine. For every increase in rotor diameter, the power output of a turbine grows quadratically. While this results in higher capital costs for wind turbine construction, the cost of energy per MWh decreases. This trend is visible if we look at the historical development of wind turbine dimensions, which shows a change in rotor diameter from approximately 80 m in 2000 to 222 m in 2021 (Siemens Gamesa Renewable Energy, 2023).

Although increasing turbine dimensions leads to a lower cost of energy, deployment of wind turbines in urban environments quickly runs into limitations. Larger turbines have a higher visual impact on the local population, increased noise levels, as well as larger areas of land required for the installation. With the available space for wind turbines becoming more scarce, especially in densely populated countries such as The Netherlands, moving the installation to offshore environments becomes more compelling. Besides moving to larger turbine dimensions, offshore wind energy also has the benefit of higher average wind velocities and lower turbulence intensities, resulting in a higher and more stable

Figure 1.5: Foggy conditions at the Horns Rev 2 offshore wind farm off the coast of Denmark visualize the wake effect. Photo by Bel Air aviation - helicopter services.

energy production (IEA, 2019). However, the transition to offshore deployment is not trivial, as it requires stronger constructions to wither the harsher conditions, additional material resources for the turbine foundations, increased installation and maintenance costs, and grid connection through submarine cables, among others. At the moment, the cost of offshore wind still exceeds that of onshore wind energy. This is reflected by the fact that offshore wind energy was responsible for only 7% of the total wind energy production in 2021 (IEA, 2022). However, the share of offshore wind energy is expected to grow in the coming years. In the Dutch part of the North Sea alone, multiple wind farms have been commissioned and are currently being constructed, providing an additional 9.5 GW by 2030 (Ministerie van Economische Zaken en Klimaat, 2022).

Connecting offshore wind farms to the grid, along with keeping the wind turbines in operating shape through maintenance, make up a large part of the cost breakdown of offshore wind farms. To cut these costs as much as possible, most wind farms are installed in dense clusters. Unfortunately, this approach can significantly decrease the efficiency of a wind farm when wake losses occur. Wakes are characterized as large zones of low-velocity, highly-turbulent wind trailing a wind turbine, that are created as a turbine extracts energy from the wind. The wake effect is observed in Figure 1.5, where a fortunate combination of atmospheric conditions visualized the wakes trailing the turbines. As can be seen, these turbine wakes are hitting downstream turbines. Annual power production losses resulting from wake effects are typically estimated to be around 10 % (Veers et al., 2022).

1.3 Wind farm flow control

As wake losses are responsible for a large decrease in efficiency for wind farms, mitigating these losses would consequently lower the costs of offshore wind power. During the design process of a wind farm, wake effects are taken into account within the layout optimization. However, such an optimization is a multi-disciplinary effort depending on many conflicting factors, and hence wake losses cannot be avoided entirely (Veers et al., 2022). Fortunately, it is possible to reduce wake effects, at least partially, for a given wind farm layout using wind farm flow control. This potential solution only requires an adjustment to the wind turbine control structure, making it possible to implement on any wind farm. Furthermore, wind farm control can also be used as an optimization variable in the wind farm design process (Meyers et al., 2022). Different alternatives for the wind farm flow control concept are illustrated in Figure 1.6, in the case of a two-turbine array. The figure visualizes the wake shear layer as well as the horizontal velocity profile at multiple locations in the wake. Aside from power maximization, wind farm control can also be utilized to provide ancillary grid services (Aho et al., 2012; Vali et al., 2019a; Boersma et al., 2019), or alleviate loads (Kanev et al., 2018; Vali et al., 2019b; Silva et al., 2021). However, the focus of this thesis will be on improving power efficiency.

1.3.1 Greedy control

The top example from Figure 1.6 shows the standard control case, where the upstream turbine is operated in a *greedy* manner, not considering how its wake affects the turbine downstream. One can see how the wake expands and a velocity deficit appears behind the upstream turbine. When considering the operating regions from Figure 1.4, greedy control entails operating the turbine along the optimal power tracking curve and extracting the maximum amount of energy from the wind. The subsequent wind farm control concepts are only used when the turbine is operating in this control region. For higher wind speeds (region 3), the upstream turbine does not extract maximum energy out of the wind by design, meaning that the downstream turbine is not affected as much as in region 2.

1.3.2 Static induction control

This first wind farm control concept was proposed by Steinbuch et al. (1988). It assumes that the overall efficiency of the wind farm can be improved by derating the upstream turbine. This can either be achieved by pitching the blades, or operating the turbine at a sub-optimal tip-speed ratio. Instead of extracting the maximum available power from the wind, the turbine purposefully operates below the optimal power curve from Figure 1.4. This results in higher wake velocities, allowing the downstream turbine to make up for the power losses of the upstream turbine. Additionally, the structural loading of both turbines decreases, as the upstream turbine experiences lower axial loads, while the downstream turbine experiences less turbulence. The result is a potential lifetime increase, which directly contributes to a lower cost of energy.

Static Induction Control (SIC) showed potential power benefits for wind turbine arrays when evaluated with steady-state wake models (Schaak, 2006; Annoni et al., 2016; Kazda et al., 2016; Kanev et al., 2018). However, studies employing higher-fidelity models such as large eddy simulations were less optimistic, and generally reported losses in efficiency (Santoni et al., 2015; Nilsson et al., 2015; Annoni et al., 2016). Multiple wind tunnel experiments on SIC were carried out to mixed results, reporting both losses (Wang and Garcia-Sanz, 2018; Frederik et al., 2020b) and gains in overall efficiency (Corten and Schaak, 2003; Corten and Schaak, 2004a; Bartl and Sætran, 2016; Campagnolo et al., 2016b;

Adaramola and Krogstad, 2011; Bartl and Sætran, 2016; Ceccotti et al., 2016). However, most of these gains were of small magnitude and benefited from a small turbine spacing and low turbulence intensity. In scenarios where turbine spacing was increased, or the ambient turbulence was higher, SIC was no longer able to improve the overall efficiency. Early field experiments showed that derating the upstream turbine improved the performance of downstream turbines, although the overall efficiency gain was not as conclusive (Schepers and Van Der Pijl, 2007; Boorsma, 2015; Bossanyi and Ruisi, 2021). Furthermore, proper analysis of the results was hampered by a limited amount of measurement data, which was observed by the large spread in the processed measurements. Based on the previously mentioned results, we believe additional research on SIC is required to determine whether the potential benefits are sufficient for further implementation in commercial wind farms.

1.3.3 Wake steering control

This second concept relies on steering the wake away from downstream turbines, such that these experience undisturbed inflow conditions. There are multiple ways to achieve this effect, although most examples in the literature consider a yaw misalignment to be the most effective method. By introducing a yaw misalignment, a transverse loading component is exerted on the incoming flow, which deflects the wake away from the dominant wind direction. Additionally, the yaw misalignment creates a pair of counter-rotating vortices at the top and bottom of the rotor, which transforms the wake into its characteristic kidney shape as it travels downstream (Howland et al., 2016). Although the power output of the yawed turbine decreases, the loss is compensated by the additional power generated by the downstream turbines.

Wake deflection through a yaw misalignment was first studied in several wind tunnel experiments that measured the wake of a scaled wind turbine model (Clayton and Filby, 1982; Grant et al., 1997; Parkin et al., 2001). Next, Medici and Dahlberg (2003) demonstrated how wake steering could be employed to improve the overall efficiency of a wind turbine array or wind farm. The potential of wake steering control for wind farm power maximization was further explored for utility-scale turbines using large eddy simulations (Gebraad et al., 2014b; Fleming et al., 2015). Following more successful demonstrations in wind tunnel experiments (Campagnolo et al., 2016c; Bastankhah and Porté-Agel, 2019) and high fidelity simulations, several field tests were carried out at commercial wind farms (Fleming et al., 2017b; Fleming et al., 2019a; Howland et al., 2019; Doekemeijer et al., 2021; Howland et al., 2022). Each of these field tests demonstrated that wake steering improved the overall efficiency when turbines were operating in waked conditions.

While the previous work showed the potential of wake steering control for wind farm power maximization, applying it to a commercial wind farm requires a lot of additional effort. Wake steering's success depends on many factors, such as the wind farm layout, ambient conditions, and the selected yaw misalignments. Optimizing the wake steering performance for these parameters requires many thousands of iterations, which makes simplified analytical wake models a necessity. Recent years have seen many developments in these surrogate models related to wake velocity models (Jensen, 1983; Larsen, 1988; Frandsen et al., 2006; Bastankhah and Porté-Agel, 2014), wake recovery due to turbulence (Ainslie et al., 1990; Crespo and Hernandez, 1996), interaction between multiple turbine wakes (Katić et al., 1987; Gebraad et al., 2014a), and modeling the effect of yaw misalignments (Jimenez et al., 2009; Bastankhah and Porté-Agel, 2016; Martínez-Tossas et al., 2019), among others. All these models share a common steady-state nature, which makes them computationally efficient and hence suitable for wind farm optimization. When optimizing the yaw misalignments for all ambient conditions (wind speed, wind direction, turbulence intensity) at an arbitrary wind farm site, these models estimate a potential increase in Annual Energy Production (AEP) in the order of 1% (Kanev et al., 2018; King et al., 2021).

Successful demonstration of wake steering control through simulations and field experiments has already resulted in a commercial product offered by a wind turbine manufacturer (Siemens Gamesa Renewable Energy, 2019). However, the previously mentioned research does not consider wake steering in a dynamic environment, where wakes are affected by changes in wind speed and wind direction. As these conditions change, the optimized operating setpoints might no longer be valid, potentially resulting in efficiency losses due to wake steering. Considering uncertainties in the yaw optimization process offers a partial solution to this challenge (Rott et al., 2018; Quick et al., 2020). This solution can be further improved by viewing wake steering as a closed-loop control problem. Doekemeijer et al. (2020) used wind turbines as sensors in combination with a steady-state wake model to estimate the current ambient conditions. Subsequently, the yaw misalignments could be optimized for the current conditions, ensuring that wake steering is only active when power gains are available. Closed-loop control can be even further improved when one considers dynamic wake models (Gebraad et al., 2014a; Shapiro et al., 2018; Becker et al., 2022; Broek et al., 2022).

1.3.4 Wake mixing control

The two previous wind farm flow control methods both considered optimal steady-state adjustments to the wind turbine's operational settings, which are only adjusted when the ambient conditions have changed sufficiently. Wake Mixing Control (WMC) employs continuous adjustments of the wind turbine's actuators, through pitch, torque, or yaw control, to mitigate wake effects (Westergaard, 2015). This type of actuation introduces additional instabilities to the wake, that cause it to break down at a faster rate and affect downstream turbines less. Dynamic yaw control is generally considered too slow and taxing on the structural loads for effective wake mixing. In this thesis, we mainly consider WMC by pitch actuation, often referred to as Dynamic Inducion Control (DIC). Figure 1.6 illustrates the concept of DIC using a collective periodic pitch action, which results in a wake that subsequently expands and contracts.

Goit and Meyers (2015) employed large eddy simulations to dynamically optimize the induction factor of each wind turbine and increase the overall wind farm efficiency. Their results showed that a dynamic variation of the induction can yield much higher gains than its static counterpart. A more pragmatic approach to dynamic induction variations was made by only considering periodic changes in the form of a sine wave, at the cost of a small drop in efficiency (Munters and Meyers, 2018). Next, Frederik et al. (2020b) carried out wind tunnel experiments with a three-turbine array, where the most upstream turbine operated with a periodic pitch variation to achieve changes in the induction over time. This experiment confirmed that DIC is capable, under the right ambient conditions, of improving the power performance of a wind farm.

Building on the previous work, Frederik et al. (2020a) extended the idea of periodic dynamic induction control to include individual pitch actions. This technique was labeled *the helix approach*, due to the helical velocity profile that appears in the wake. The helix approach uses Dynamic Individual Pitch Control (DIPC) to create yaw and tilt moments on the rotor plane, by making a part of the rotor less transparent to the incoming wind. At this location on the rotor surface, the induction is highest and hence results in the largest velocity deficit. By moving the combined yaw and tilt moment over the rotor surface, the helical wake shape is created. Large eddy simulations indicated that this technique is more effective than periodic dynamic induction control in increasing the overall power efficiency of two turbines. Although it is not covered in this thesis, the additional structural loading that results from continuously adjusting the turbine's operating setpoint is of special concern, both on the upstream and downstream turbines (Wang et al., 2020; Croce et al., 2022a; Frederik et al., 2020b).

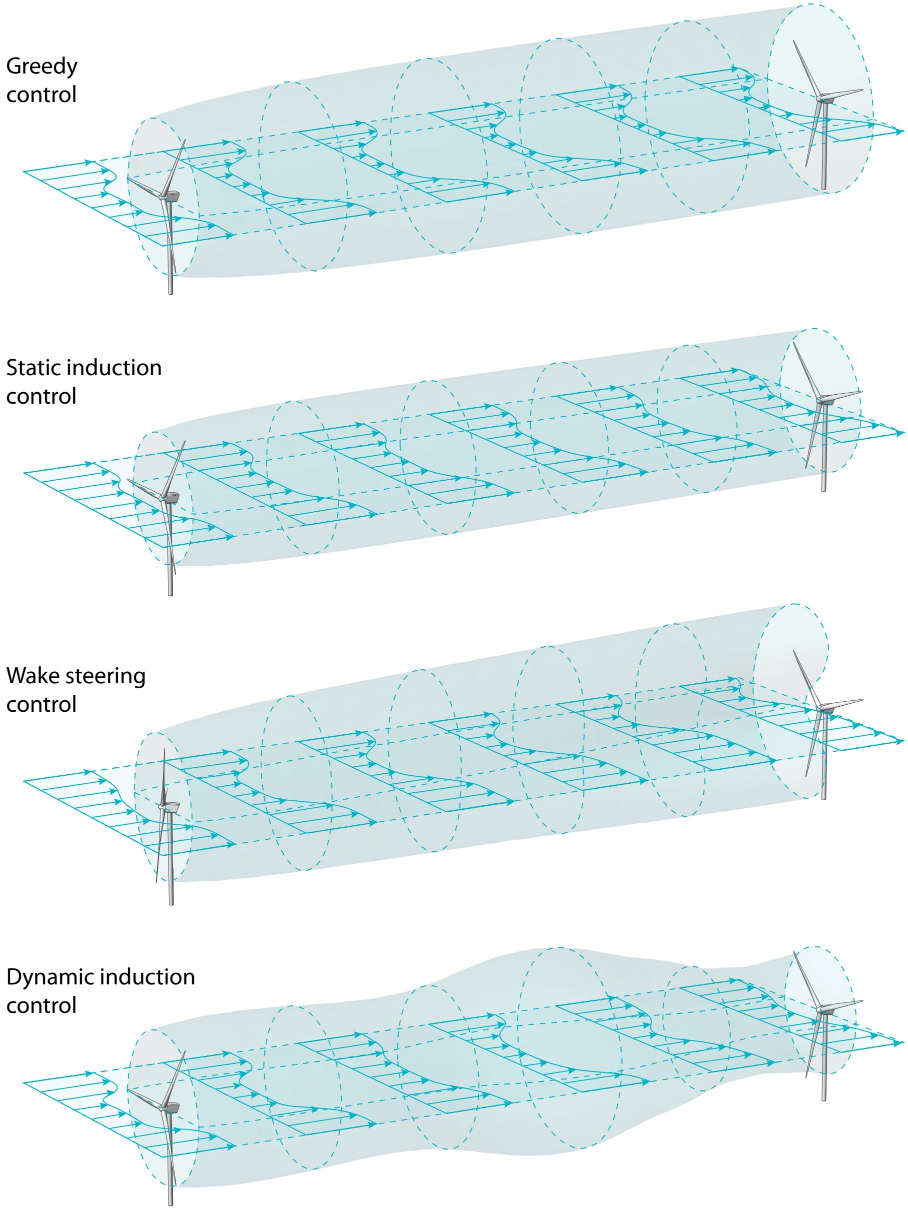

Figure 1.6: Schematic overview of different wind farm flow control concepts in the case of two aligned wind turbines. The figure visualizes the boundary of the wake, as well as horizontal velocity profiles at multiple locations in the wake. With *greedy control*, the upstream turbine is prioritizing its own power production, resulting in a low-velocity, highly-turbulent wake hitting the downstream turbine. By derating the upstream turbine, *static induction control* lets the upstream turbine extract less energy and leave more for downstream turbines. *Wake steering control* introduces a yaw misalignment with respect to the incoming wind, to steer the wake away from downstream turbines. Finally, continuous adjustments of the turbine's operating setpoints allow *dynamic induction control* to improve wake mixing and accelerate the breakdown of the detrimental wake.

1.4 Goal of this thesis

Three wind farm flow control concepts, including four different actuation techniques, were discussed in the previous section, highlighting the state of the art for each of these techniques. Based on this overview, it is clear that each method has both advantages as well as disadvantages. To further decrease the cost of wind energy, we focus on further developing each of these techniques. Hence, the goal of this thesis is the following:

Thesis goal: Advance the state of the art of wind farm flow control techniques for maximizing wind farm power performance.

The literature overview from the previous section made it clear that each of the wind farm control concepts that were discussed are at different stages in their development cycle. In an attempt to assess at which stage of the development cycle the wind farm control methods are, one can use the Technology Readiness Level (TRL) metric first introduced by NASA (Office of Aeronautical and Space Technology, 1991) and later adopted by the European Comission (2014) for its Horizon 2020 program. The TRLs can act as a guide for developing new ideas based on the observation of a specific phenomenon (TRL 1) to a commercial product or application (TRL 9). Applying this metric to a selection of the literature from the previous section results in the development overview given by Figure 1.7. This thesis covers static induction control, wake steering control, and two wake mixing control methods, namely periodic dynamic induction control and dynamic individual pitch control. For each of these methods, a knowledge gap in the development cycle was identified and investigated accordingly.

1.4.1 Research objectives

The first research objective that is considered concerns static induction control. At the time of this research, several initial field trials had been executed. While these experiments indicated some level of efficiency gain for downstream turbines, the overall power results were inconclusive. This indicates that additional research is required to determine whether SIC is an effective method for maximizing the power of a wind farm. Therefore, the first research objective is the following:

Research objective I: Examine the potential of pitch-actuated static induction control for improving wind farm power efficiency in a field test.

Next, wake steering control is studied. While this concept is already being offered as a commercial product by one wind turbine manufacturer, there remain many open questions in the literature, mostly concerning the effect of varying conditions on power performance. One of the proposed solutions to this challenge is given by closed-loop control, which generally uses the available turbine measurements in combination with an analytical wake model to optimize the turbine yaw angles for changing conditions. Solving the closed-loop control problem is a large challenge on its own. However, even in the case of perfect reconstruction of the ambient conditions, and the subsequent yaw misalignment optimization, there are practical limitations to changing the yaw setpoints. Furthermore, the same steady-state analytical wake models are used to determine the potential benefits of wake steering on the AEP. The relatively low fidelity of such models introduces uncertainties on the estimated benefits, especially due to the lack of dynamics. Accounting for these dynamics in the AEP calculation would reduce the amount of uncertainties in the estimated power gains due to wake steering control. Thus, the next research objective is formulated as:

Research objective II: Determine the effect of wind direction variations on the estimated increase in Annual Energy Production with wake steering control.

Compared to wake steering, dynamic induction control is a relatively recent development. So far, high-fidelity simulations have indicated that this technique shows great potential. The first wind tunnel experiments confirmed that periodic dynamic induction control can improve the overall efficiency of a three-turbine array. However, its success depends on multiple factors, such as the frequency and amplitude of the pitch actuation, the spacing between turbines, and the ambient turbulence intensity. Furthermore, some questions remain regarding the mechanism that causes the wake to break down faster. Therefore, the following research objective will be examined:

Research objective III: Investigate the mechanism responsible for the accelerated wake breakdown when applying periodic dynamic induction control.

The helix approach is an even more recent innovation in the wind farm control field. Consequently, a large number of questions remain concerning its use for maximizing wind farm power. While large eddy simulations indicated improved performance compared to periodic dynamic induction control, it has yet to prove itself in an experimental environment. The next step in the development is to validate the method in the wind tunnel, resulting in the following research objective.

Research objective IV: Validate the potential gain in wind farm power efficiency using dynamic individual pitch control (the helix approach) in a wind tunnel environment.

By treating these four research objectives, this thesis aims to aid in the development of the different wind farm control concepts, thereby achieving the goal of this thesis as specified at the start of this section.

1.4.2 Thesis outline

The core of this thesis comprises four chapters, each treating one of the four research objectives. All chapters consist of previously published articles, allowing an independent reading of each chapter. Consequently, each of the chapters contains an introduction that reviews the recent literature at the time of writing the article. As such, some parts of these introductions might appear outdated. Furthermore, many of the concepts and literature presented in Chapter 1 are repeated. Finally, each chapter has been added to the TRL graphic in Figure 1.7, indicating where this thesis contributes to the wind farm control development cycle.

Chapter 2 analyzes the results of a field test incorporating pitch-actuated static induction control on an onshore commercial wind farm. The control settings were optimized using a steady-state wake model, and applied automatically for a specific set of ambient conditions. The performance is compared to that estimated by the wake model, both in terms of power efficiency and load reduction potential. Finally, the difficulty in validating wind farm control concepts in field trials is discussed.

Chapter 3 presents a framework that can be used to update Annual Energy Production estimations using high-fidelity simulations. The framework employs more realistic (i.e. with wind direction changes) large eddy simulations, and uses these results to correct an analytical steady-state wake model, thereby providing higher confidence to the estimated potential power gains. The framework is applied to a previously used example of a real-life offshore wind farm.

Chapter 4 investigates how dynamic induction control using periodic pitch actuation breaks down the wake at an accelerated rate. PIV is employed to obtain time-resolved measurements of the near wake of a scaled wind turbine model. The level of wake recovery is evaluated for different actuation frequencies. The relation between tip vortex interaction and wake breakdown is investigated. Furthermore, the challenges involving wind tunnel experiments are discussed, of and the lessons learned will be implemented in the wind tunnel experiment from Chapter 5.

Chapter 5 presents the results of a wind tunnel experiment that aims to validate the capabilities of the helix approach to maximize wind farm power output. The experiment consists of collecting measurements with a two-turbine array, as well as PIV measurements of the wake of the upstream turbine.

Although each chapter contains a conclusion section of its own, these conclusions are reiterated in **Chapter 6** to address the research objectives that were presented in this chapter. Additionally, some overall conclusions on the implementation of wind farm flow control are presented. Finally, a set of recommendations is provided that can guide future research into these topics.

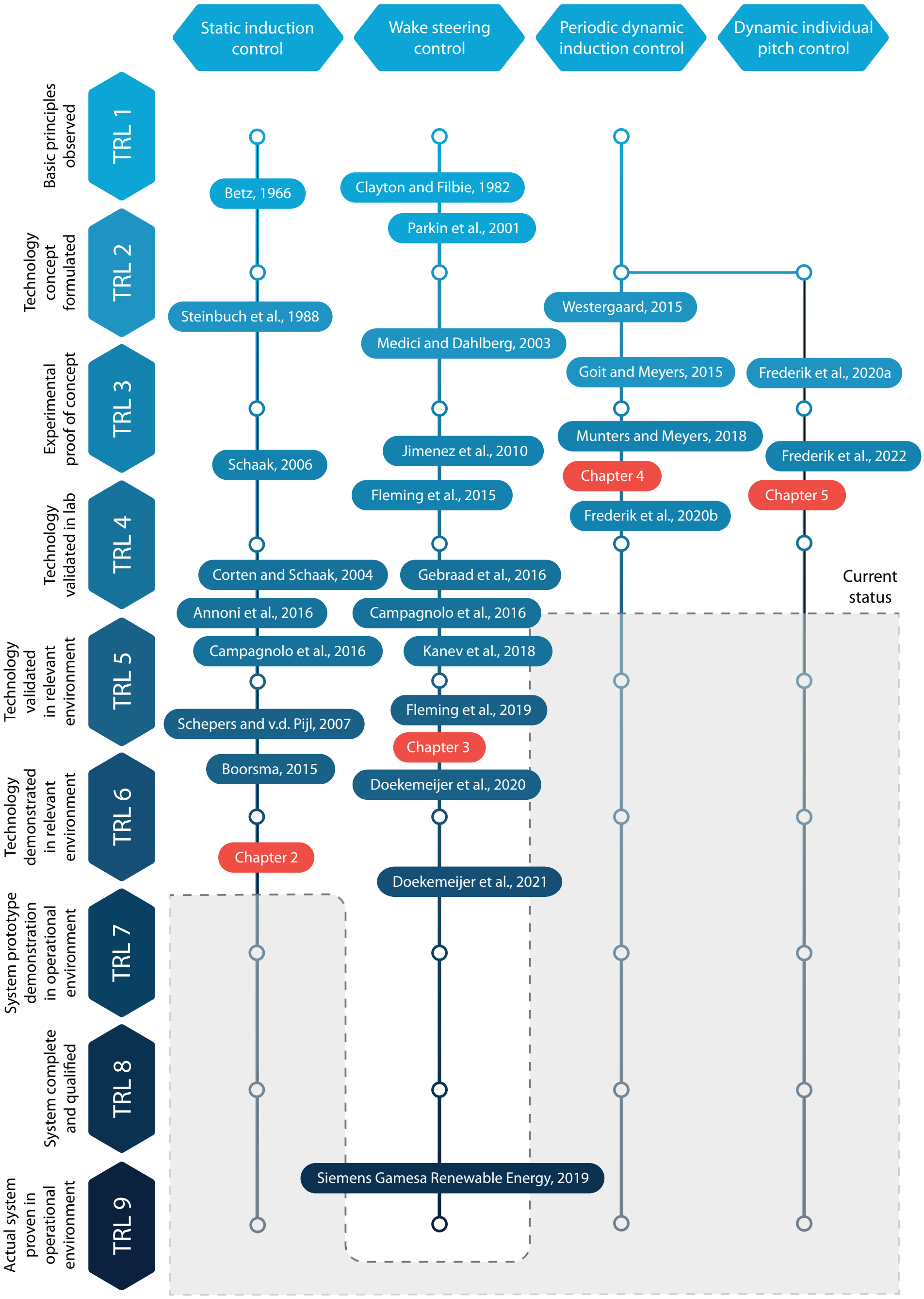

Figure 1.7: Development of wind farm flow control concepts expressed by their Technology Readiness Levels. The overview contains a selection of the key publications discussed in Section 1.3, as well as the contributions of this thesis.

2

Testing static induction control on a commercial wind farm

Recent years have seen an increased interest in literature in Active Wake Control (AWC) strategies, which aim to reduce wake losses in wind farms to increase the energy yield and/or decrease loading. This chapter presents the results from field tests with one of the AWC strategies, called static induction control, at a commercial wind farm. To this end, the pitch angle offset for the most upstream wind turbines was optimized for each wind direction to maximize the power capture of the whole farm. This optimization was performed using the wake model FARMFLOW, a code based on parabolized Computational Fluid Dynamics (CFD). After calibration of the wind direction measurement and implementation of the optimized pitch settings, a measurement campaign of one year was carried out. The analysis of the measurements indicates that static induction control results in increased energy production.

The contents of this chapter have previously appeared as a separate research article:
🗎 Hoek, D. van der, Kanev, S., Allin, J., Bieniek, D., and Mittelmeier, N. (2019). "Effects of axial induction control on wind farm energy production - A field test". *Renewable Energy* 140, pp. 994–1003. DOI: `https://doi.org/10.1016/j.renene.2019.03.117`.

2.1 Introduction

For the design of a wind farm, multiple factors are considered with the goal of finding an optimal balance between energy production and costs. In this complex optimization problem, there are numerous constraints (construction, operational, grid, environmental, financial, etc.) that play a role in the farm design and, consequently, there are currently many areas in which research organizations and industry are looking for possibilities to further reduce the Levelized Cost of Energy (LCoE). The work in this chapter is motivated by the current practice of operating wind turbines located in a wind farm individually, each one aiming to maximize its own energy production, without regarding its effect on the output of surrounding turbines. It is believed by the wind energy community that such an approach is not optimal for the overall energy production of the wind farm. Following the increasing number of wind farms worldwide, researchers have started developing new strategies for cooperative operation of the turbines in wind farms (Knudsen et al., 2015; Spruce, 1993; Kanev et al., 2018), aiming to maximize the energy production of the wind farm and/or decrease the fatigue loading of individual turbines. These strategies are referred to here as Active Wake Control (AWC). The reader is referred to (Boersma et al., 2017) for a recent overview on AWC literature.

AWC methods can be divided into two classes. The first class of AWC methods is called wake redirection control and consists of steering the wakes away from downstream wind turbines. Wake redirection can be achieved most efficiently by operating the wind turbines with a yaw misalignment (Corten et al., 2004; Gebraad et al., 2014b; Kanev et al., 2018). This approach to AWC has received a lot of attention recently, with publications ranging from modeling the effects from yaw misalignment (Shapiro et al., 2018; Bastankhah and Porté-Agel, 2016), to including loads into the optimization (Dijk et al., 2017), to layout optimization (Gebraad et al., 2017), to using flow-measurements in a feedback control setting (Raach et al., 2017). Recently, NREL published the first measurement results from a test with wake redirection on a few offshore wind turbines (Fleming et al., 2017b). Besides a yaw misalignment, other approaches have also been studied in the literature, including rotor tilting, yaw-oriented and tilt-oriented individual pitch control, and even wind turbine repositioning (Fleming et al., 2014; Fleming et al., 2015).

The second class of AWC methods is called axial induction control and contains strategies that aim to reduce the wake deficit downstream by reducing the axial induction factor of upstream wind turbines. This can be achieved by down-regulating the turbines at the windward side, either by increasing the blade pitch angle (Corten and Schaak, 2003; Corten and Schaak, 2004b; Kanev et al., 2018) or operating at a suboptimal tip-speed ratio (Hoek et al., 2018). The concept of axial induction control is compared to normal operation in Figure 2.1. By operating the upstream turbine to maximize its own power, it is seen that the wind velocity in its wake decreases, leaving less energy in the wind to be extracted by the downstream turbine. The right side of the figure demonstrates axial induction control. In this case, the upstream turbine is operated with an increased blade pitch angle. While the energy production of the down-regulated wind turbine decreases, the wind velocity in its wake increases. This allows for higher energy production at downstream wind turbines that could potentially raise the overall wind farm production. In the last years, a wide variety of approaches have been proposed in the literature, such as (Annoni et al., 2016; Ciri et al., 2016; Munters and Meyers, 2016; Rotea, 2014; Gebraad and Wingerden,

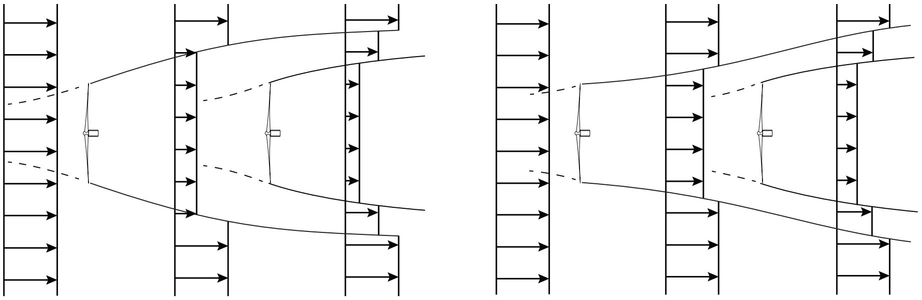

Figure 2.1: Schematic overview of two wind turbines aligned with the wind in normal operation (left) compared to axial induction control (right). Figure adapted from (Corten and Schaak, 2003).

2015; Vali et al., 2017a) to mention a few.

Initial experiments in a wind tunnel (Corten and Schaak, 2003; Corten and Schaak, 2004a) at a very small scale (rotor diameter of 0.25m), and in the field (Boorsma, 2015) have shown that the energy production of a wind farm may potentially increase using axial induction control. However, more recent high-fidelity simulations (Annoni et al., 2016) and wind tunnel tests (Campagnolo et al., 2016a) were unable to confirm these power benefits, which could be due to several reasons (see e.g., the discussions in Boorsma, 2015; Campagnolo et al., 2016a; Ciri et al., 2016). These results question the feasibility of axial induction control and call for additional testing on large-scale wind turbines.

The purpose of this chapter is to present the results from a detailed measurement campaign with axial induction control, performed at the Goole Fields wind farm, a commercial wind farm located in England consisting of 16 Senvion 2050 kW wind turbines with a diameter of $D = 92.5\,\mathrm{m}$. The duration of the measurement campaign was over one year, and axial induction control was implemented by operating upstream turbines with a pitch angle offset. The pitch offset was toggled on and off every half a week. The optimal pitch angle settings for the wind turbines were determined using the wake model FarmFlow. The data has been carefully post-processed by applying filtering (ensuring only the right operating conditions are taken in the analysis) and corrections (to avoid differences in air density, turbulence intensity, and axial induction effects on the wind measurement contaminating the analysis). The results of the measurements indicate a potential energy increase of around 3.3% for a range of below-rated wind speeds.

The chapter is organized as follows. In Section 2.2, the wind farm layout is provided and the optimized pitch settings are presented. Section 2.3 explains the filtering and correction steps that were applied to the data and explains the method used for the analysis of the power measurements. Furthermore, the measured (normalized) power curves of the wind turbines are presented. The results of the experiments are further discussed in Section 2.4 and additional comments are given on the execution of the measurements. The chapter is concluded with some final remarks in Section 2.5.

2.2 Field experiment setup

The field test with axial induction control was performed at the Goole Fields onshore wind farm located in England and operated by Innogy SE. The wind farm is located in flat terrain, surrounded by minor vegetation, and consists of 16 Senvion wind turbines ($D = 92.5\,\mathrm{m}$) with a rated power of 2050 kW each. The wind farm has an irregular layout with turbines being positioned in two rows of 5 turbines and one row of 6 turbines with each row having a slightly different angular orientation. Furthermore, the turbines from each row are not exactly in line with each other. An overview of the layout is given in Figure 2.2, with the distances between the turbines expressed in terms of the rotor diameter D. For the three rows, the distance between turbines varies between 2.3 and 3.1 D. Furthermore, it can be seen that a met mast is located in the wind farm near turbine T6. Due to the row-wise layout with closely spaced turbines, the Goole Fields wind farm is well qualified for testing the effects of axial induction control.

The axial induction control pitch settings were optimized using the wind farm model FarmFlow, which consists of a 3D parabolized Navier-Stokes code that uses a k–ϵ turbulence model to account for turbulent processes in the wake (Bot, 2015). The parabolization is achieved by neglecting the pressure terms in the Navier-Stokes equations. Atmospheric stability is accounted for via the Monin-Obukhov length parameter. For a given wind direction, the optimization process starts by performing a reference calculation using the nominal pitch settings for all below-rated wind speeds, in which FarmFlow computes the wake parameters at each turbine location. An example of such a calculation is given in Figure 2.3, where the wind speed and turbulence intensity are given for a wind direction aligned with a row of turbines. It can be observed that the wind speed decreases by approximately 25% in the wake of the upstream turbine, while the turbulence intensity increases significantly. The next step in the optimization process consists of identifying rows of turbines for the considered wind direction and optimizing the pitch settings for each of these rows. It should be noted that only the pitch settings of the most upstream turbines are optimized in this process, since earlier studies with FarmFlow have indicated

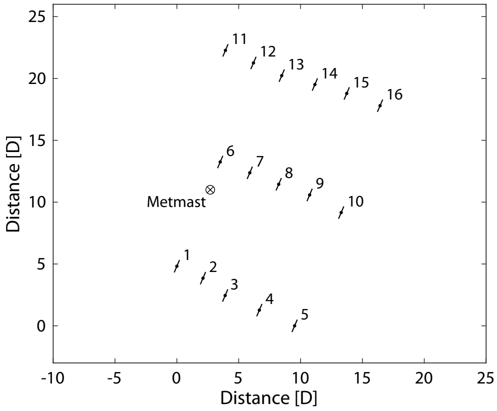

Figure 2.2: Overview of the wind farm layout including met mast. The distances between turbines are expressed in number of rotor diameters (D).

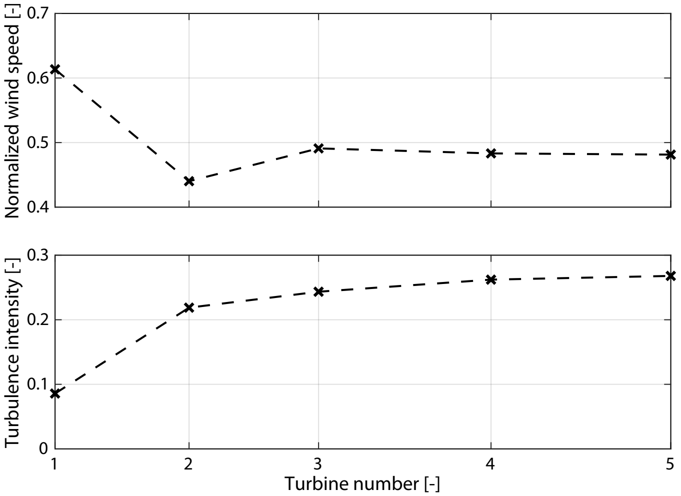

Figure 2.3: Wind speed and turbulence intensity at multiple turbine locations as calculated by FarmFlow. The simulation was performed for wind coming from the northwest aligned with the row with a normalized wind speed of $U = 0.62$.

that increasing the pitch angle of additional turbines downstream does not improve the energy yield.

Simulations of the Goole Fields wind farm showed that there are benefits to be gained in energy production using axial induction control. These benefits are largest for wind coming from the North-West and South-East, when the wind is aligned with the three rows of turbines. A more detailed look at the benefits of axial induction control predicted by FarmFlow simulations is given in Figure 2.4. Both power and wind speed have been normalized with conditions close to rated power. According to the simulations, the power of the first turbine drops when axial induction control is activated, which is expected since the pitch angle offset reduces the aerodynamic efficiency of the blades. For all the remaining turbines of the row, an increase in power can be observed, resulting from the increased wind speed in the wake of the first turbine. In the case of the entire row for this particular wind direction and wind speeds below the rated wind speed, axial induction control results in approximately 5.6% energy increase according to the simulations. The estimated energy increase of the other two rows is in the same order of magnitude.

Besides affecting energy production, AWC also reduces the turbulence intensity in the wake of the upstream turbine. This can be observed in Figure 2.4, in which the turbulence intensity at the location of each turbine in row T1-T5 is given for baseline operation and in the case of AWC for the most beneficial wind direction. After the wind passes the first turbine, the turbulence intensity increases significantly at each turbine. In the case when axial induction control is used, an increase in turbulence intensity is still visible, though it is much lower compared to baseline operation. Given the relationship between turbulence intensity and fatigue loads of a wind turbine, i.e., fatigue loads increase almost linearly for increasing turbulence intensity (Kanev and Savenije, 2015), this is a major benefit of AWC.

As a result of the wind farm optimization, the optimal pitch settings are generally

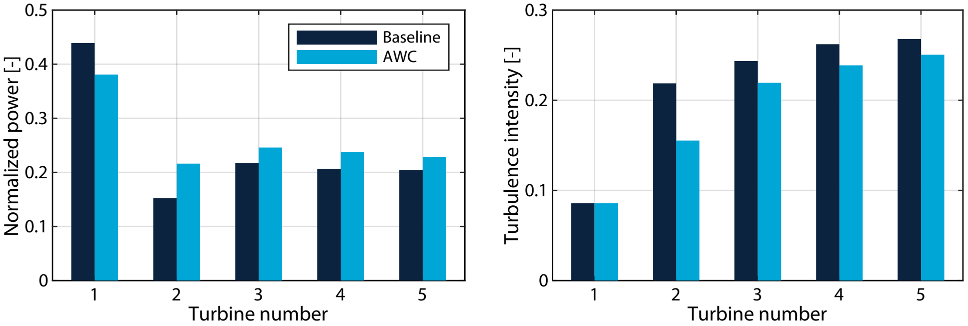

Figure 2.4: Normalized power (left) and turbulence intensity (right) of turbines in row T1-T5 for north-western wind, and a normalized wind speed of $U = 0.62$ in case of baseline operation and axial induction control.

different for each wind direction (see solid line in Figure 2.5). To simplify implementation, it was required to limit the number of pitch angle offsets to two. Therefore the optimized pitch settings were approximated with a discrete function containing two pitch sections as visualized in Figure 2.5. Subsequently, three sectors are defined with different pitch settings: one full wake sector where only the high pitch action is performed and two partial wake sectors where the smaller pitch angle is used. A schematic representation of these sectors is given in Figure 2.6. According to simulations, the largest effects of axial induction control are present in a full wake situation.

The measurement campaign started in May 2016 and ended in June 2017. Axial induction control was implemented only in the wind directions aligned with the three rows as seen in Figure 2.2 (i.e., the North-West and South-East directions), since these directions show the greatest benefits for energy production optimization due to the shorter distances between the turbines. In the North-West direction, the pitch settings were used until January 2017, at which time an extension of the wind farm was started to the North-West of the existing turbines. The pitch settings for the South-East direction were used during the entire measurement campaign. The wind turbine controller turns on the axial induction

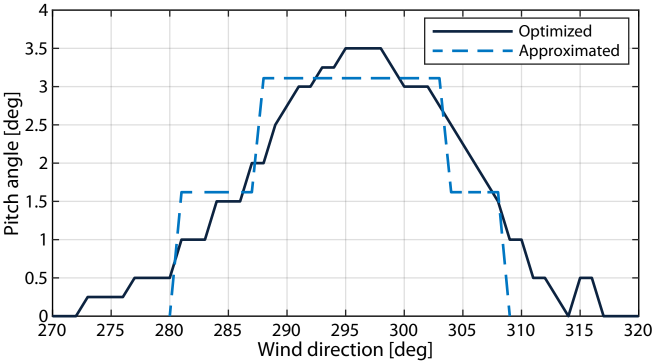

Figure 2.5: Optimized and approximated pitch settings for axial induction control.

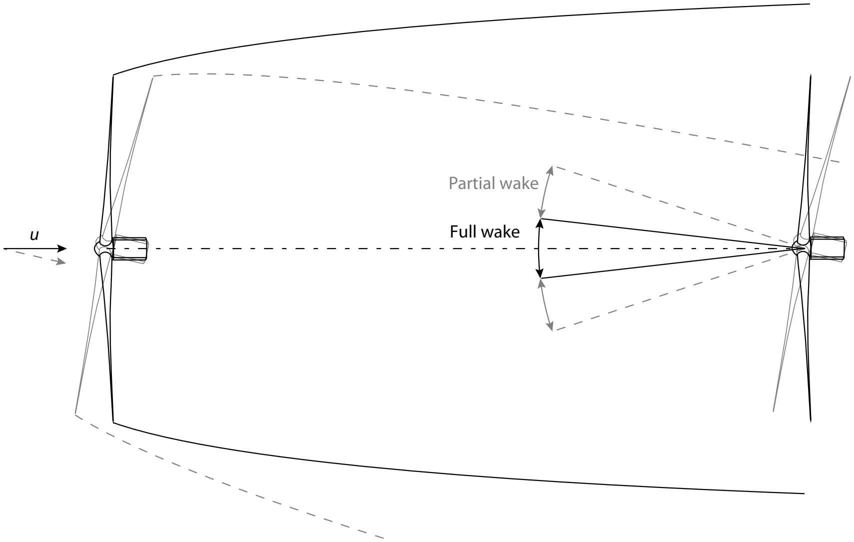

Figure 2.6: Top view representation of the full and half wake sectors as used for the implemented pitch settings.

control settings at the start of a week and turns them off after 3.5 days. This process is repeated during the entire measurement campaign. In the case when axial induction control is active, the pitch settings of the upstream wind turbine are activated only when the wind is oriented in one of the sectors indicated in Figure 2.6. These pitch settings only affect the power production until the regular pitch commands of the turbine controller exceed the optimized pitch offsets.

Prior to the start of the measurement campaign, a calibration was performed to ensure accurate measurements of the wind direction, which is essential for the proper operation of axial induction control. The calibration offsets were implemented by adjusting the pitch settings.

The measurements that were collected during the field test consist of 10-minute average SCADA data from each wind turbine along with data from the met mast indicated in Figure 2.2. This data includes the electrical power, blade pitch angles, generator speed, nacelle orientation, wind turbine operational state (e.g., operational, idling, etc.), wind direction, wind speed, outdoor temperature, air pressure, and relative humidity.

2.3 Results

To properly analyze the effects of axial induction control on the wind farm's energy production, the measurement data needs to be filtered and corrected wherever necessary. In this section, the applied filtering and corrections on the measurement data are presented. Subsequently, these filters and corrections are applied to the measurement data to compare measured wind speeds and power during normal operation in partial load with operation using axial induction control.

2.3.1 Filtering measurement data

The first step is to investigate the overall wind conditions at the wind farm by looking at the distribution of the wind direction using measurements with wind speeds in partial load. This process results in the wind rose given in Figure 2.7. It can be observed that the North-West sector experiences a decent amount of wind. However, the southeast sector barely sees any wind and can therefore not be used for analyzing the effects of axial induction control.

Clearly, for successful testing of induction control, an accurate wind direction measurement is essential to ensure that the pitch angle offsets will be applied when the wake location is correct with respect to downstream turbines. Therefore, before the start of the campaign, a calibration was performed on wind direction measurements at the six turbines located at each end of the three rows[1]. For a given upstream turbine (say, T1), this calibration was performed by using the power deficit measurement at the turbine in its wake (T2). The power deficit consists of the power of the second turbine in a row divided by the power of the first turbine. The calibration offset is the difference between the measured wind direction with the highest power deficit and the geometric orientation of the line along these two turbines. These calibration offsets are then implemented directly into the lookup tables for the pitch angle offsets, modifying the input of the tables from the actual wind direction to the (biased) measured wind direction.

Based on the measurement data collected during the test campaign, the accuracy of the wind direction measurements has been evaluated using the same approach involving power deficit measurements. If, for whatever reason, the bias in the wind direction measurements has changed significantly during the measurement campaign, the corresponding measurements need to be excluded from the analysis. Figure 2.8 depicts the results

---

[1] Notice that the wind direction is not directly measured in the turbines but constructed by using the measurement of the nacelle orientation and the yaw error measured by the wind vane.

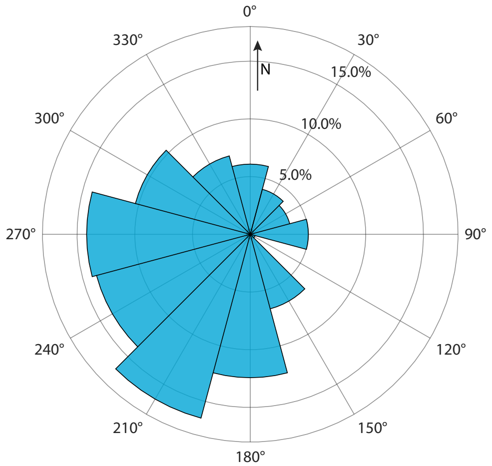

Figure 2.7: Wind rose created from met mast measurement data collected during the trial period for below-rated wind speeds.

from the verification of the calibration settings for turbine T1 by analyzing the wind direction (measured at T1) at which T2 experiences the highest power deficit (black vertical line in the figure). The red vertical line represents the corresponding value obtained during the initial calibration. The difference is just around 1.5°, which is considered small enough to include row T1-T5 in the analysis. However, for T6 the verification process identified a difference of 12° between the wind directions of the highest wake deficit at T7 derived from the initial calibration and the measurement campaign. This implies that the pitch angle offsets at T6 have mostly been applied at wind directions for which T7 is not fully in the wake of T6, making the data acquired from row T6-T10 not useful for analyzing the benefits of induction control. The difference for the row T11-T16 is found to be 7°, which means that only a small sector remains for analysis. Table 2.1 provides a summary of the calculated differences (measurement bias) between the wind direction measurements during the test campaign and the values used in the initial calibration. The table also provides the wind direction sectors and pitch angle offsets as an outcome of the induction control optimization, as well as the corrected full wake wind direction sector used in the analysis. Notice that the correction of the sector is applied only at one side of the original sectors, since the pitch offsets have only been applied incorrectly at that side. Table 2.1 does not contain the partial wake sectors with corrections, since it was found that the amount of measurement data within these sectors was too small to perform an accurate analysis.

The next step is to filter out all the data that is not relevant for comparing the performance of axial induction control with baseline operation. For this purpose, the following filtering criteria were applied to the measurement data:

- Wind direction: the measurements are filtered to only contain data for the desired (corrected) wind directions sector given in Table 2.1.
- Wind direction variation: In reality, the wind direction is varying constantly, while the settings for induction control are optimized for constant wind directions. To per-

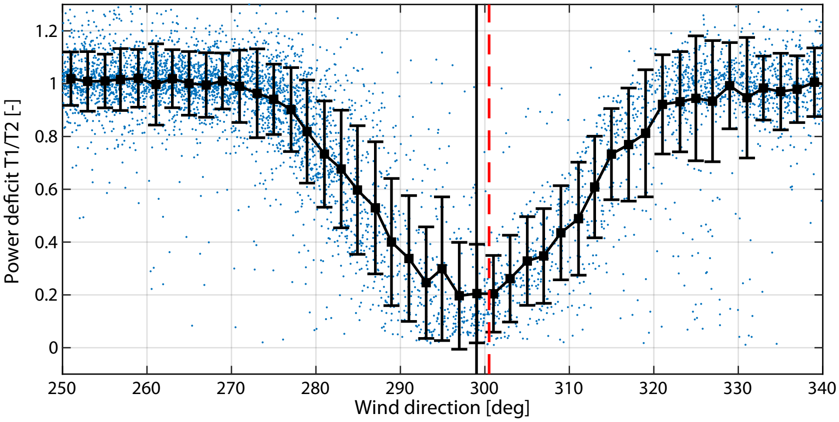

Figure 2.8: Power deficit of turbine T2 with respect to turbine T1, as a function of the wind direction measured at T1. The vertical black line indicates the wind direction with the highest power deficit based on the validation data, while the dashed line represents the direction with the highest deficit used in the initial calibration.

Table 2.1: Blade pitch settings in degrees for axial induction control before and after correction of the wake sectors.

	Sector	Pitch offset	Measurement bias	Sector for analysis
Row T1-T5	285.0-292.5 292.5-308.5 308.5-314.0	1.62 3.11 1.62	1.5	292.5-307.0
Row T6-T10	294.0-299.5 299.5-315.5 315.5-320.0	1.59 3.07 1.59	12.0	-
Row T11-T16	280.0-285.5 285.5-299.5 299.5-307.0	1.86 3.23 1.86	7.0	285.5-292.5

form an accurate assessment of the effects of induction control, wake meandering should be kept to a minimum. This is done by limiting the standard deviation of the wind direction measured at the nacelle of the most upstream turbine to a maximum of 5°.

- Generator speed: axial induction control is only expected to result in increased energy production when the turbines operate in partial load (i.e., below-rated wind speed). This condition is met by filtering for rotor speeds between the minimum and maximum values.

- Operational status: using this signal it is possible to determine if the upstream wind turbine is operational and whether AWC has been activated during the 10-minute interval.

- Pitch action: to make sure that the pitch settings were active or inactive for the entire 10-minute interval, the pitch angles are analyzed. If the 10-minute average pitch angle is the same as one of the pitch angles given in Table 2.1, then AWC has been active throughout the whole 10-minute interval. If the pitch angle is smaller than 0.2°, the turbine was operating with the nominal pitch angle.

- Yaw action: for a proper analysis it is important that the turbine has not experienced significant yaw action over the 10-minute interval. Therefore, the standard deviation of the turbine yaw angle is limited to 5°.

- Turbulence intensity: the turbulence intensity is computed using the standard deviation and mean value of the wind speed measured at the met mast. It is important to filter for turbulence intensity since it has a noticeable impact on energy production. Subsequently, very low and high turbulence intensities in the undisturbed wind are filtered out by only keeping the data with a turbulence intensity between 2.5 and 9%. Ideally, the measurement results should be presented for multiple ranges of turbulence intensity, as it also affects the wake recovery. However, splitting the current range into smaller parts or decreasing its size results in an insufficient amount of measurement data to allow a proper analysis.

- Missing data: for some periods, data from either the wind turbine or met mast is missing. When this is the case, then all the measurement data from that period is removed from further analysis.

2.3.2 Correcting measurement data

Filtering has been applied to reduce the amount of data to only relevant measurements. However, there are still differences between the measurement data that require some corrections. This specifically refers to corrections on the measured wind speed, which are listed below.

- Air density: two measurements of the same wind speed at different time instances will likely have a different air density. Since generated power is linearly related to air density, the measurement with the higher density will likely result in higher generated power. To correct for such occurrences, the measured wind speed $U_{10\text{min}}$ is normalized using the following equation (International Electrotechnical Commission (IEC), 2005):

  $$U_n = U_{10\text{min}} \left(\frac{\rho_{10\text{min}}}{\rho_0} \right)^{\frac{1}{3}}, \tag{2.1}$$

  where ρ_0 is the reference air density and $\rho_{10\text{min}}$ is the measured density. Since air density is not measured directly, it needs to be computed using other measurements. This has been done using measurements collected by the met mast of the barometric pressure, the temperature, and the relative humidity (International Electrotechnical Commission (IEC), 2005).

- Turbulence intensity: similar to the air density, the turbulence intensity also has a direct effect on the energy production of a wind turbine. Higher turbulence generally leads to higher energy production. Consequently, a correction factor is also used to normalize the wind speed at the nacelle of the first turbine with respect to turbulence intensity. This correction is given by the following equation (Wagenaar and Eecen, 2011):

  $$U_{\text{corr}} = U_n \left(1 + 3 \left(\frac{\sigma_{U_{\text{MetMast}}}}{U_{\text{MetMast}}} \right)^2 \right)^{\frac{1}{3}}, \tag{2.2}$$

  where U_n is defined in Equation (2.1).

- Axial induction effects: for the analysis of axial induction control, the power and wind speed measured by the nacelle anemometers are used. The nacelle anemometers are preferred over the met mast, since the latter is some distance away from the two rows of turbines. It is expected that the wind speed measured by the anemometers will differ when axial induction control is active. To quantify this effect, the wind speeds measured at the upstream turbine are compared with wind speed measurements from the met mast. Such a comparison is presented in Figure 2.9 using

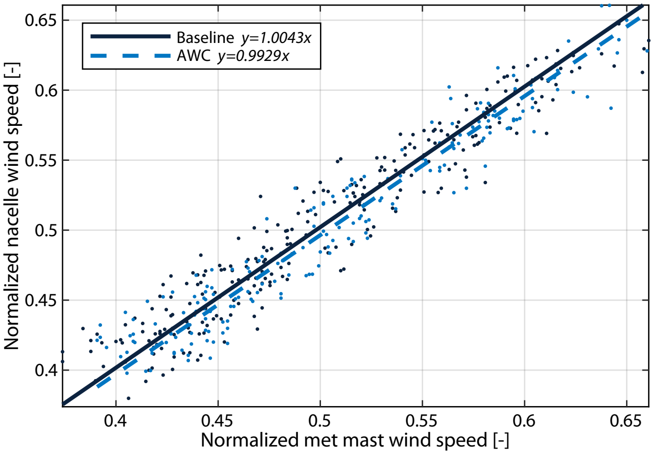

Figure 2.9: Effect of axial induction control on the wind speed measured at a wind turbine nacelle.

measurements from turbine T6. This turbine is selected since it is in close proximity to the met mast. Before the measurements of both the nominal and induction control settings are compared, the wind speed measurements of the nacelle are first corrected for air density and turbulence intensity as indicated above. Next, a linear regression is performed for both sets of measurement data. It can be observed that a slightly higher wind speed is measured at the nacelle under baseline operation. This is probably the result of the higher axial induction at the outer part of the rotor under baseline operation. Due to the resulting blockage effect, the wind velocity close to the blade roots, and thus the anemometer, is higher than in the case of induction control. To compensate for this difference in wind speed measurement, the wind speed U_{AWC} measured at the nacelle during operation with induction control is corrected as follows:

$$U_{\mathrm{AWC,corr}} = U_{\mathrm{AWC}} \left(\frac{a_{\mathrm{bl}}}{a_{\mathrm{AWC}}} \right), \tag{2.3}$$

with a_{bl} and a_{AWC} representing the slopes of the linear regression $y = a \cdot x$, for the baseline and induction control cases, respectively. The difference between both slopes is in the order of 1%. It is assumed that similar relations exist for the other two rows of turbines and that the corrections are approximately the same for similar pitch angle offsets. The same correction factor is thus used for rows T1-T5 and T11-T16 as well.

2.3.3 Turbine measurement results

Once the measurement data for rows T1-T5 and T11-T16 had been filtered and corrected, it was used for analyzing the power performance. The amount of data for both rows that is left after filtering is given in Table 2.2. It can be observed that a very large part of the measurement data has been omitted as a result of filtering. The amount of data remaining for row T11-T16 is deemed too low to allow for accurate analysis and therefore only the results for row T1-T5 are presented.

Table 2.2: Amount of measurement data for the two rows of turbines.

	Baseline data points (hours)	AWC data points (hours)
Row T1-T5	125 (20.8)	201 (33.5)
Row T11-T16	25 (4.2)	61 (10.2)

The results of the measurement campaign are presented by determining the measured power curve, which is created by binning the wind speeds in bins of $0.5\,\mathrm{m\,s^{-1}}$ and by calculating the mean values of the normalized wind speed and normalized power output for each bin according to IEC standards (International Electrotechnical Commission (IEC), 2005). Besides computing the power curve using the binned averages, the standard error is computed to indicate the accuracy of the power curve. The measured power curves are computed for both baseline operation and axial induction control and subsequently compared to analyze the effect on energy production. Furthermore, this effect is quantified by weighting the bins from the measured power curve with the measured wind speed distribution for the considered wind direction sector to estimate the impact on the overall energy production. The distribution that is used for this process is given in Figure 2.10.

The measured power curve of the entire row T1-T5 is presented in Figure 2.11. The bars represent the standard uncertainty of the power for each wind speed bin. It is observed that the measured power curve with axial induction control lies on or above the baseline curve for almost every wind speed. By combining the power curve with the wind speed distribution, the total energy of the row for operation in partial load is computed. By comparing the total energy of the baseline data and the axial induction control data, it is found that axial induction control results in a 3.3% increase in energy. The effects of induction control on the power performance were also examined without applying the axial induction correction from Section 2.3.2 to the measured wind speed. This resulted in an even greater benefit in energy production, though we consider the analysis including

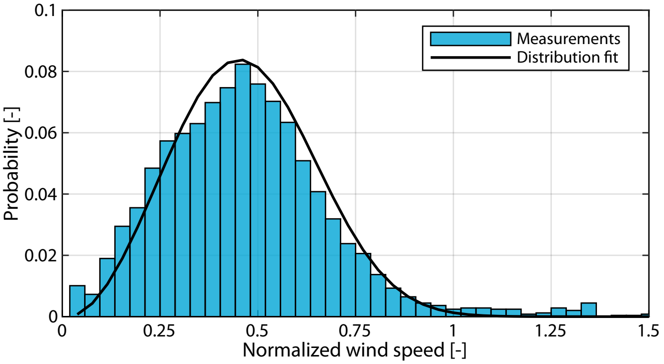

Figure 2.10: Wind speed distribution for the full wake sector of turbine T1.

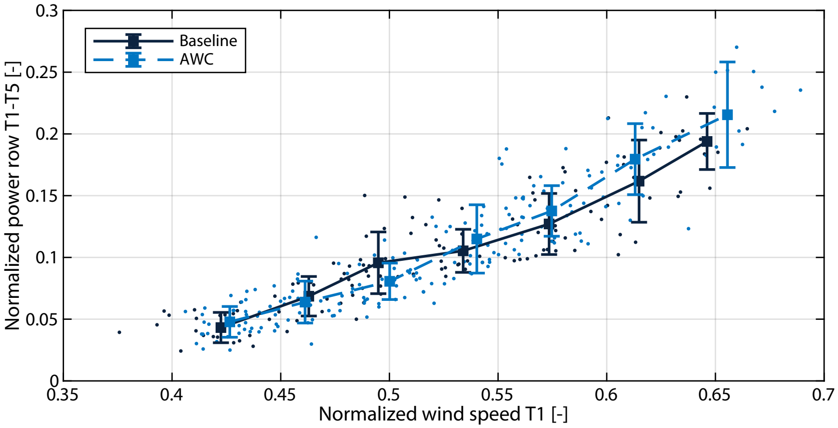

Figure 2.11: Normalized measured power curve for row T1-T5 under baseline operation and with axial induction control.

the correction to be more realistic.

To see what the effects of axial induction control are on a wind turbine level, the measured power curves for each of the turbines in row T1-T5 are given in Figure 2.12. In the first plot, it can be seen that with induction control the measured power curve is lower than the baseline measured power curve. This result is expected due to the increased pitch angle and also agrees with the simulation data (Figure 2.4).

At the second turbine (T2) it can be seen that the power curve with induction control is greater than that of the reference case. This is the direct result of the increased pitch angle of the first wind turbine, which reduces the wind speed deficit and thus results in higher wind speeds at the second turbine. So far, this result is in line with the simulation data. However, when the measured power at $U = 0.62$ is compared to the simulation data from Figure 2.4, it can be seen that the power is much lower than the estimate from FarmFlow.

At the third turbine (T3) an increase in power is still observed when axial induction control is applied, but with the measurements showing a significant spread. It seems that the turbine is either not operating, or is generating even more power than the second turbine. It is assumed that this is due to the location of the third turbine, which is not fully in line with the rest of the row (see Figure 2.2). As a result, the turbine sometimes finds itself in the full wake of the previous turbine and will thus have a lower energy production, while at other times it experiences only part of the wake and can generate more power.

Looking at the fourth turbine (T4) it can be observed that it generates more power on average under baseline operating conditions. This is not what was expected from simulations, meaning that the effect of induction control on the wind speed in the wake has been overestimated. At the fifth turbine (T5) the effect of induction control is also not visible anymore, with power being approximately the same.

Since the wind turbines at the test site were not equipped with any load measurement devices, it was not possible to directly analyze the effects of axial induction control on the fatigue loads of the turbines. However, it is possible to analyze the effects on turbulence intensity. In Section 2.2, it was already stated that there is a direct relationship between

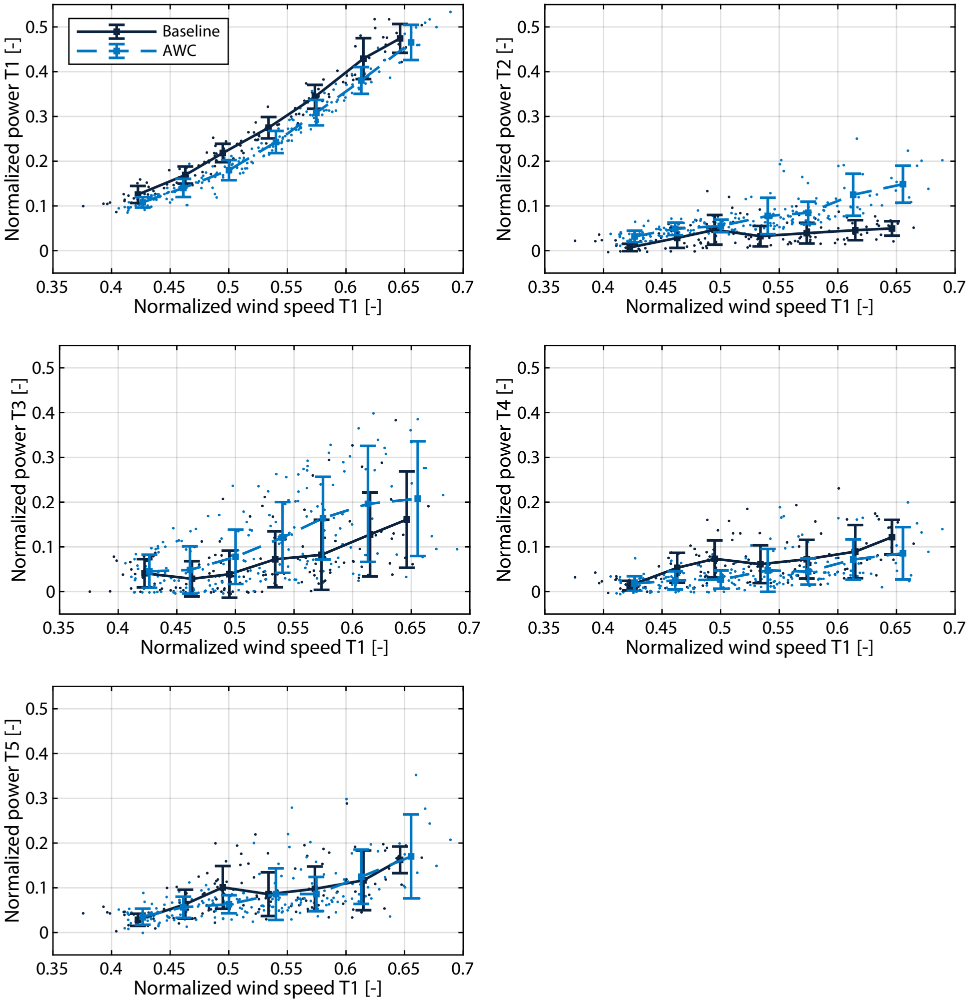

Figure 2.12: Normalized measured power curves for turbines T1 to T5 under baseline operation and with axial induction control.

turbulence intensity and fatigue loads of a wind turbine. Therefore, it is possible to comment on the load trends of the turbines by looking at the turbulence intensity derived from the nacelle anemometer measured wind speeds at each turbine. In Figure 2.13, the average turbulence intensity at each turbine is given for both baseline operation and induction control for the normalized wind speed of $U = 0.62$. As expected, in both cases the turbulence intensity is similar for the upstream turbine and increases further downstream. For the second and third turbine, a significant reduction in turbulence intensity is visible when induction control is used, and therefore it is expected that the fatigue loads of these turbines will decrease. This effect is no longer visible for the fourth and fifth turbines, where the turbulence intensity is approximately the same.

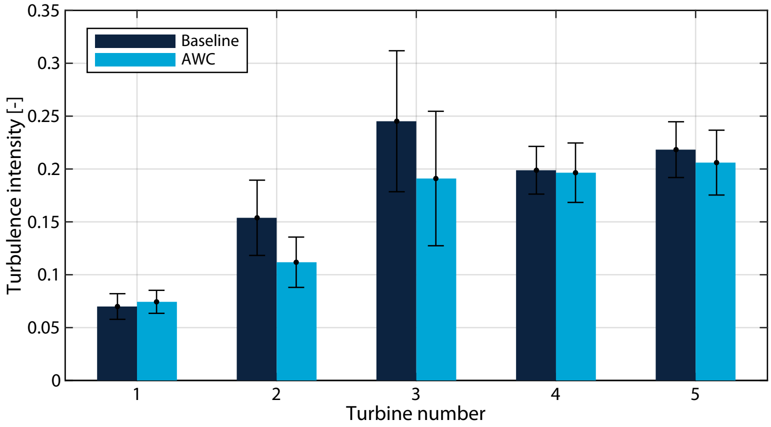

Figure 2.13: Average turbulence intensity with standard uncertainty measured at the turbine nacelles for a normalized wind speed of $U = 0.62$.

2.4 Discussion

In Section 2.2, it was stated that the expected benefit in energy production for a single row is approximately 5.6% according to simulations. The measurement results from the previous section are lower than this figure but do indicate a potential benefit. Looking at the results for individual turbines, some differences are visible between the simulations and measurements. By comparing the normalized power production from FarmFlow in Figure 2.4 with the measured power curves in Figure 2.12, it can be seen that FarmFlow has overestimated the wind speed and thus the generated power at the second turbine. This is due to the fact that the underlying wake model in FarmFlow has been optimized for offshore wind farms where the distances between turbines are larger. For very short distances, as with the Goole Fields wind farm, the near wake region model is known to be less accurate (Bot, 2015). In the first one to two rotor diameters distance downstream, the turbulent mixing in the wake is negligible. In this region, FarmFlow overestimates the mixing due to the k–ϵ turbulence model, which is not accurate in the near wake. In FarmFlow the k–ϵ model is tuned in the near wake region to get accurate results at distances of $5D$ downstream and beyond. For smaller distances downstream however, FarmFlow overestimates the mixing and therefore underestimates the wake effects. As a result, the current pitch offsets are probably not optimal. In case of future experiments, it is advised to optimize the pitch settings with a FarmFlow model that has been tuned for the considered wind farm.

An additional factor that contributes to the discrepancy in simulation and measurement results is given by the difference in yaw behavior. The simulations have been performed with a constant yaw orientation. In reality, the yaw angle of the turbine can change significantly within a 10-minute interval. Therefore, the measurement data was filtered by limiting the maximum standard deviation of the yaw angle. However, within the selected measurement data there are still periods where the downstream turbines are not operating in full wake but in partial wake, which leads to lower overall energy gains.

From the simulated and measured power production, another difference can be observed from the trends of power production for the individual turbines. The trend is in agreement with the simulation data from FarmFlow for the first three turbines. If we look at the effect of induction control on the power production of the fourth and fifth turbine, an increase in power is estimated by FarmFlow. However, this effect is not visible in the power curves of these turbines measured during the field test. The fourth turbine shows a decrease in power production due to induction control, while the fifth turbine does not seem to be affected by it at all. A possible explanation for these two results could be given by slower wake recovery due to reduced turbulence intensity at the third turbine and less wake meandering. This last phenomenon is also a result of axial induction control, caused by a reduced shear force exerted by the most upstream turbine on the wake due to the reduced axial induction. The downwind turbine will therefore spend more time in a wake situation than when induction control is not active, leading to a slower recovery of the wind speed. Additionally, the location of the third turbine, which is not exactly in line with the other turbines, could play a role. To verify these possible explanations, a more detailed measurement of the wakes is required.

The effect of axial induction control on the turbulence intensity in the wake was also analyzed. If we compare the simulation and measurement data, it can be seen that both show an increased turbulence intensity in the wake of the upstream turbine but that induction control leads to a relative decrease in turbulence intensity. In the simulations, this reduction was visible for every downstream turbine, while measurements only showed this effect for the first two turbines in the wake. Furthermore, the absolute level of turbulence intensity in the wake differed between the simulation and measurement data. This could be due to the fact that FarmFlow was not optimized for wind farms with very closely spaced turbines, or because the turbulence intensity was measured using the nacelle anemometer, which usually results in a less accurate measurement.

To compare the performance of axial induction control with baseline operation, the amount of measurement data was reduced to only contain relevant measurements. The consequence of the filtering process was that the measurement data for row T11-T16 could not be used for accurate analysis. While there was more data available for row T1-T5, there is still some uncertainty in the measured power curve for several wind speeds. The reason for this limited amount of data is also related to the layout of the wind farm, which is generally chosen such that the wind directions with dominant wake effects do not coincide with the main wind direction at the site. In the case of a new measurement campaign, it is therefore advised to increase the duration of the experiment to gather sufficient data for analysis.

In Section 2.3, it was also examined whether the settings for axial induction control were activated in the correct wind sectors by performing a power deficit analysis. It was observed that the row T6-T10 showed a large offset between the calibrated and measured wind sectors, causing the measurement data from this row to be omitted from the analysis. The lesson that can be learned from this for future measurement campaigns, is to regularly check the wind direction measurements and recalibrate them whenever necessary.

When analyzing the effect of axial induction control on the energy production of a row of turbines, it was found that the analysis was very sensitive to small changes in measured wind speed. This fact, along with the measurements from Figure 2.9, indicate that an accurate measurement of the wind speed is required to improve the precision and accuracy of the analysis. In this campaign, the anemometer from the wind turbine nacelle was used for wind speed measurement, which can sometimes lead to inaccurate measurements. A possible solution for this would be the use of LIDARs for ambient wind speed measurements.

The measurement results that were presented in this study indicate that with axial induction control, the energy production of a wind farm could potentially be increased. In this case, only the energy production of a single row in a small wind direction sector was examined. In terms of AEP, the increase is expected to be much lower since the benefit is achieved only for some wind directions which are less prominent in the wind rose and for wind speeds during partial load. Nevertheless, even a small increase in energy production can be interesting for large wind farms.

2.5 Conclusion

In this chapter, the performance of axial induction control on the energy production of a row of wind turbines was examined using field measurements from the Goole Fields onshore wind farm operated by Innogy SE. The wind farm consists of three rows of 2050 kW Senvion turbines of which measurements were taken for a period of one year. Prior to the measurement campaign, the optimal pitch settings for axial induction control were computed using the wind farm simulation tool FarmFlow. After implementation, these induction control settings were then activated at the start of a week and deactivated after 3.5 days. During the time induction control settings were activated, the controller started pitching the blades when the turbine was oriented in a specified wind direction sector. These sectors consist of three parts, a full wake sector with high pitch angles and two partial wake sectors with lower pitch angles. Before the effects of axial induction control could be analyzed, it was required to filter out irrelevant data and correct measurements where necessary. As a result of these actions, it was only possible to analyze the performance of induction control for a single row of turbines. After computing the measured power curves in the case of baseline operation and with AWC, the benefit of induction control was quantified by weighting the power curves with the measured wind speed distribution. In doing so, it was found that the application of induction control during partial load on a single row of turbines resulted in a 3.3% increase in energy for the considered wind direction sector and wind speeds. Using simulations it was estimated that the energy benefit for the entire farm, considering all wind speeds and directions, lies at 0.37%. Since only a part of the farm has been analyzed using measurement data, it is not possible to come up with an accurate figure for the benefit of the entire farm. However, based on the evaluated row of turbines, it is expected that the actual energy benefit for the entire Goole Fields wind farm will be below 0.37%.

3

Predicting the impact of wake steering on the annual energy production

In recent years, wake steering has been established as a promising method to increase the energy yield of a wind farm. Current practice in estimating the benefit of wake steering on the Annual Energy Production (AEP) consists of evaluating the wind farm with simplified surrogate models, casting a large uncertainty on the estimated benefit. This chapter presents a framework for determining the benefit of wake steering on the AEP, incorporating simulation results from a surrogate model and large eddy simulations to reduce uncertainty. Furthermore, a time-varying wind direction is considered for a better representation of the ambient conditions at the real wind farm site. Gaussian process regression is used to combine the two data sets into a single improved model of the energy gain. This model estimates a 0.60% gain in AEP for the considered wind farm, which is a 76% increase compared to the estimate of the surrogate model.

The contents of this chapter have previously appeared as a separate research article:
🗎 Hoek, D. van der, Doekemeijer, B., Andersson, L. E., and Wingerden, J. W. van (2020). “Predicting the benefit of wake steering on the annual energy production of a wind farm using large eddy simulations and Gaussian process regression”. *Journal of Physics: Conference Series* 1618.2. DOI: `https://doi.org/10.1088/1742-6596/1618/2/022024`.

3.1 Introduction

Currently, research on wind farm control mainly focuses on improving the energy yield of a wind farm. One promising method to achieve this is wake steering, in which upstream turbines are misaligned with the inflowing wind in order to redirect their wake away from downstream machines (Jimenez et al., 2009). Consequently, the downstream turbines experience a higher wind speed and produce more power, at the cost of a small reduction in power at the upstream turbines. This leads to a net increase in power production of the farm. The optimal yaw misalignments required to steer the wake are generally obtained using a simplified surrogate model of the wind farm (Boersma et al., 2017). To validate the hypothesized energy gains from surrogate models, the control solutions are either implemented in high-fidelity simulations (Gebraad et al., 2014b), wind tunnel experiments (Campagnolo et al., 2016c) or field tests (Fleming et al., 2017b; Howland et al., 2019).

Field tests are expensive to perform, carry a certain risk, and are difficult to validate. Furthermore, wind tunnel experiments only allow limited validation due to the scale and conditions that can be replicated. Simulations offer a cheaper and more practical solution and allow better control of the tested conditions, but they suffer from being very computationally expensive. For these reasons, wake steering is generally only validated for a small number of cases, and therefore does not provide an estimate of the potential increase in AEP for a wind farm. Instead, such predictions often rely on the surrogate model that was used for the yaw setpoint optimization in combination with statistical data obtained from measurements at the wind farm site (Fleming et al., 2016b; Gebraad et al., 2017; Kanev et al., 2018). While these approaches predict energy gains in the order of 1% for specific wind parks, the relatively low fidelity of such a surrogate model compared to reality casts a large uncertainty on these gains.

Besides model mismatches that can influence the estimated AEP gain, the aforementioned approach does not take a dynamic implementation of wake steering and its additional challenges into account. These challenges include the estimation of ambient conditions for determining the optimal yaw angle, a realistic yaw setpoint tracking controller, evaluating the effects of wake steering on turbine loads, and robustness to time-varying ambient conditions. While often unaddressed, these aspects can have a major impact on the AEP benefit of wake steering.

This chapter evaluates the benefit of wake steering on the AEP of a large offshore wind farm using high-fidelity simulations and Gaussian process regression (Rasmussen and Williams, 2006). It extends the work presented in Churchfield et al. (2015), where several Large Eddy Simulation (LES) results of a simple wind park were used to fit a curve of the expected energy gain. The main contribution of this chapter is a framework that combines both low- and high-fidelity simulations into a single model of the energy gain, as a function of wind direction and wind speed. A surrogate wake model is used to predict the general trends for wake steering, while high-fidelity simulations are used to obtain a quantitative evaluation of wake steering for specific conditions. By combining these two approaches, a more realistic estimate of the potential gain for all ambient conditions is obtained, while running only a subset of high-fidelity simulations.

The outline of this article is as follows. Section 3.2 introduces the wind farm that is the main subject of this case study, as well as the simulation environments that will be used.

In Section 3.3, the framework for estimating the annual energy gain will be presented. Simulation results of both low and high-fidelity models, along with the final estimate on the AEP are presented in Section 3.4. Finally, the results are discussed and the article is concluded in Section 3.5.

3.2 Case study

The case study in this work is performed with the Princess Amalia Wind Park. This wind park has been the topic of previous studies on the effect of wake steering on the annual energy production, where different steady-state wake models predicted an increase in the AEP between 1.10–1.28% (Fleming et al., 2016b; Kanev et al., 2018). These studies will serve as a benchmark to which we compare our results later on.

3.2.1 Princess Amalia Wind Park

The Princess Amalia wind park is located near the western coast of the Netherlands and consists of 60 Vestas V80-2.0 MW wind turbines. The layout of the wind park is presented in Figure 3.1. Since the model and controller of the original Vestas V80 wind turbine are not publicly available, the turbines are replaced with the NREL 5 MW wind turbine model (Jonkman et al., 2009). To make a fair estimate of the potential increase in energy for the real wind farm, the layout is scaled according to the dimensions of the NREL 5 MW turbine.

Measurements taken from a nearby met mast for a period of one year prior to the construction of the wind farm were used to determine the wind speed and wind direction

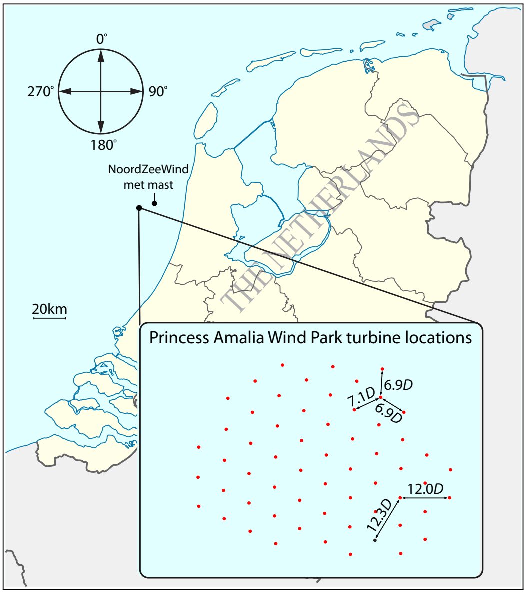

Figure 3.1: Location and layout of the Princess Amalia wind park (Gebraad and Wingerden, 2015).

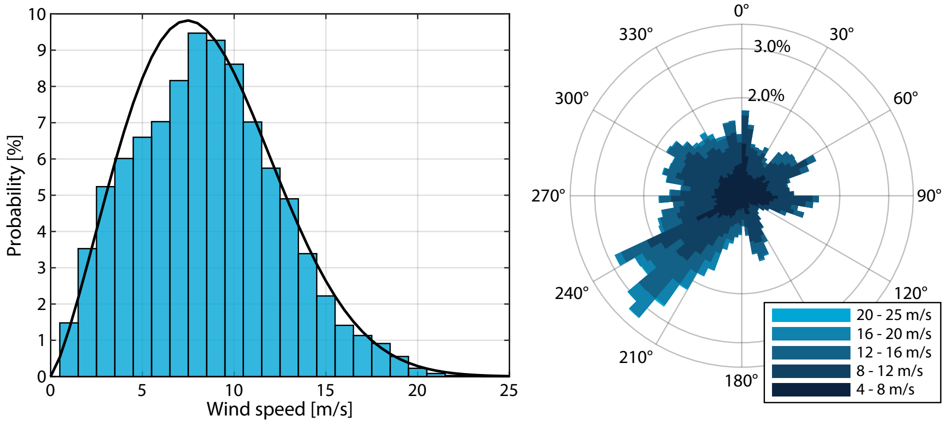

Figure 3.2: Wind speed distribution for all wind directions with accompanying Weibull fit (left) and wind rose (right) from measurements collected with a met mast near the location of the wind farm.

distributions at the wind farm site (NoordzeeWind, 2005-2006), as seen in Figure 3.2. The average turbulence intensity at below-rated wind speeds is close to 6%. The turbulence intensity is assumed to be constant for all wind speeds during the simulations. Additionally, the standard deviation of the wind direction was found to be approximately 3°.

3.2.2 Wind farm models

The surrogate model FLOw Redirection and Induction in Steady-state (FLORIS) is used to optimize the yaw angles for below-rated ambient conditions (Doekemeijer and Storm, 2020). For a given inflow wind field, FLORIS computes the time-averaged flow field and turbine performance inside a wind farm as a function of the turbine control settings. Parameters of the FLORIS model were tuned to high-fidelity simulation data in previous work (Doekemeijer et al., 2019). For more information on FLORIS, the reader is referred to the work of Gebraad et al. (2014b) and Doekemeijer et al. (2019).

The optimal yaw setpoints that are obtained using FLORIS are evaluated with Simulator fOr Wind Farm Applications (SOWFA), which is an LES model for wind farms developed at the National Renewable Energy Laboratory (NREL) (Churchfield et al., 2012; National Renewable Energy Laboratory (NREL), 2018). The flow is simulated by solving the three-dimensional unsteady Navier-Stokes equations over a discretized domain. The wind turbines are modeled in SOWFA using a Rotating Actuator Disk Model (ADM-R) (Wu and Porté-Agel, 2011). The original wind farm layout is scaled to match its properties to the NREL 5 MW turbine. An overview of the simulation settings is given in Table 3.1.

3.2.3 Time-varying wind direction

To replicate realistic operating conditions at the wind farm site, the simulations are performed using an inflow wind field with a time-varying wind direction. This is achieved in SOWFA by adjusting the boundary pressure gradients. The wind direction profile that is used for the simulations is based on high-frequency measurements from an onshore met

Table 3.1: SOWFA simulations settings.

Parameter	Value
Timestep	0.5 s
Simulation length	3000 s
Atmospheric stability	Neutral
Domain size	9.0 km x 9.0 km x 1.0 km
Cell size (outer region)	20.0 m x 20.0 m x 20.0 m
Cell size (up to 240.0 m altitude)	10.0 m x 10.0 m x 10.0 m
Blade epsilon	20.0 m
Free stream wind speed U_∞	6.0, 8.0, and 10.0 $\mathrm{m\,s^{-1}}$
Free stream turbulence intensity I_∞	5%
Free stream wind direction (average) ϕ	240.0°

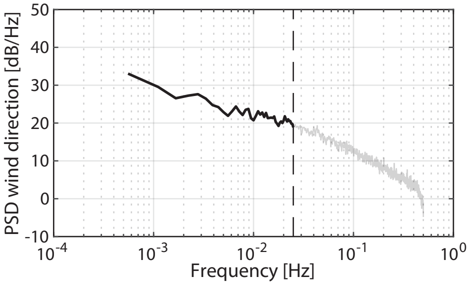

Figure 3.3: Power spectral density of the wind direction variation based on 1-Hz measurement data.

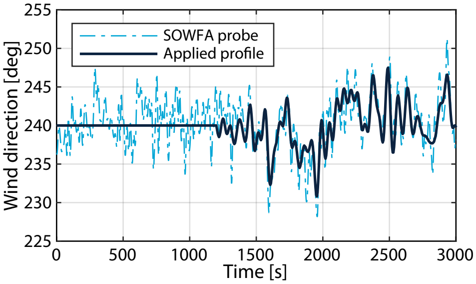

Figure 3.4: Wind direction profile as implemented in SOWFA (solid) compared to a point measurement of the flow field (dashed).

mast. Multiple thirty-minute time series of the measured wind direction were collected to compute the power spectral density given in Figure 3.3. This spectrum is subsequently used to generate a random wind direction profile based on the low-frequency content of the measurements, similar to Simley et al. (2020). Furthermore, the profile is scaled to match the 3° standard deviation of the wind direction that was obtained from the met mast data near the Princess Amalia wind farm site. High-frequency wind direction changes are not taken into account for this profile, as this is largely the result of local turbulence that is already present in the simulated wind field, as can be seen in Figure 3.4.

3.3 Framework for estimating the annual energy gain

This section describes the overall framework for estimating the annual energy gain due to wake steering. First, a short description of Gaussian processes is given in Section 3.3.1. Section 3.3.2 discusses the optimization of the yaw angles. Section 3.3.3 presents how the simulation results from FLORIS and SOWFA are integrated.

3.3.1 Gaussian processes

A Gaussian process can be described as a non-parametric model consisting of a mean and covariance function. It assumes that a set of function values belongs to a multivariate

Gaussian distribution. The correlation between function values is determined by a covariance function based on the respective inputs and a set of hyperparameters. In this work, the squared exponential covariance function is used. For a given set of training data, a Gaussian process can infer function values at new input locations. One of the strengths of Gaussian processes is their ability to estimate their uncertainty, which inherently allows them to deal with uncertainty in the training data. This aspect is relevant for our AEP prediction framework, as we combine simulation results from models with different uncertainty levels. For a more detailed explanation of Gaussian processes, the reader is referred to Rasmussen and Williams (2006). Gaussian processes can subsequently be used as a surrogate model for Bayesian optimization (Shahriari et al., 2016). This property will be used in Section 3.3.2 to optimize the yaw misalignments for all wind turbines.

3.3.2 Yaw angle optimization

The wind turbine yaw angles are optimized over the entire wind rose for 1° wind direction increments and below-rated wind speeds ranging from 4 to $13\,\mathrm{m\,s^{-1}}$. Simulation results from FLORIS are used to obtain a Gaussian process model of the wind farm power as a function of the yaw misalignments. This model is subsequently used to optimize the yaw misalignments.

The search space of the yaw misalignments is limited to positive angles with a maximum of 30°, for several reasons. Firstly, the search space is significantly reduced, thereby requiring fewer evaluations of FLORIS for convergence. Secondly, when optimizing the yaw angles for both positive and negative yaw misalignments, the optimal solutions might result in an absolute change of yaw orientation of over 50° for a 1° wind direction change (Kanev et al., 2018). Such a steep change in the yaw orientation could lead to a large increase in yaw activity. Additionally, it has been demonstrated in high-fidelity simulation studies and field experiments that negative yaw misalignments result in higher loads for yawed turbines compared to positive yaw misalignments (Fleming et al., 2014; Damiani et al., 2018; Gebraad et al., 2014b). Finally, high-fidelity simulations have shown that negative yaw misalignments are less effective than positive misalignments for increasing the power output of a wind farm. This is thought to be a combined effect of the clockwise rotation of the turbine rotor (around the horizontal axis) and the Coriolis effect (in the northern hemisphere) (Gebraad et al., 2014b; Archer and Vasel-Be-Hagh, 2019).

The yaw misalignments are optimized robustly to account for the time-varying wind direction (Rott et al., 2018). This consists of optimizing over multiple wind directions using a weighted sum of the power signals P_j with a probability density function $\rho(\phi)$:

$$\boldsymbol{\Gamma}^{opt}(\phi) = \arg\max_{\boldsymbol{\gamma}} \int_0^{2\pi} \rho(\phi) \sum_{j=1}^{n} P_j(\gamma_j, \phi)\mathrm{d}\phi. \tag{3.1}$$

In practice, the Gaussian distribution is discretized at five wind directions consisting of the mean direction, and $\pm\sigma$ and $\pm 2\sigma$ from the mean wind direction. In this study, $\sigma = 3°$ as determined from the measurement data, is used for the optimization. While robust optimization will reduce the potential increase in energy for a single wind direction, it will make the yaw setpoints less sensitive to changes in wind direction.

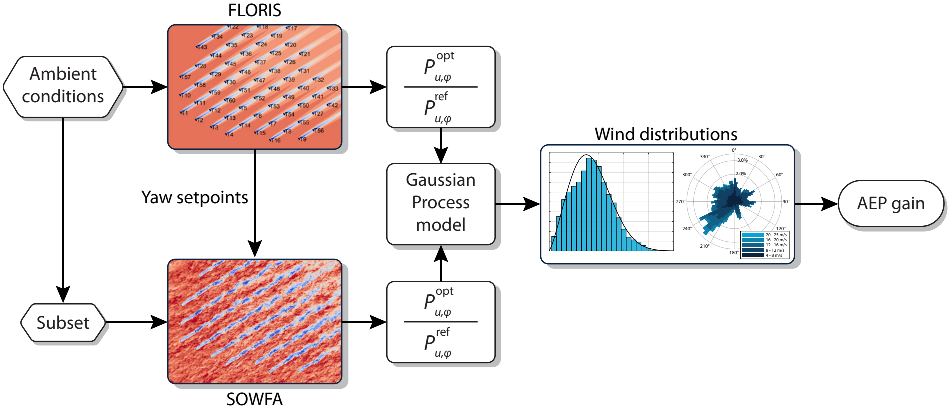

Figure 3.5: Flowchart for computing the improved AEP gain. Given a set of ambient conditions, FLORIS is used to optimize the yaw misalignments for wake steering and provide an estimate of the power gains. A selection of the ambient conditions is simulated in SOWFA using the yaw setpoints from FLORIS, resulting in an additional set of power gains. The results from both simulation tools are subsequently combined in a Gaussian process model of the power gain, as a function of wind speed and wind direction. Multiplying these power gains with the wind speed and direction distributions provides an improved estimate of the AEP gain.

3.3.3 Improving the annual energy gain prediction

The entire framework for improving the prediction of the AEP benefit is given as a flowchart in Figure 3.5. First, the surrogate wind farm model FLORIS is used to optimize the yaw angles for a range of ambient conditions. A subset of these ambient conditions is simulated in SOWFA with the previously obtained yaw setpoints. The resulting thirty-minute time series is divided into multiple five-minute time series to increase the amount of data points, as well as incorporate the variance of the power gain resulting from a varying wind direction in the Gaussian process. Next, the power gains of both the FLORIS and SOWFA simulations are computed and combined into a single dataset. A Gaussian process model of the power gain as a function of wind speed and wind direction is subsequently computed from the training data. This model is combined with the wind distributions of the wind farm site to estimate the AEP benefit.

3.4 Results

This section presents the results of the AEP gain prediction framework applied to the Princess Amalia wind farm. Section 3.4.1 discusses simulations results from SOWFA. In Section 3.4.2, a Gaussian process model of the energy gain is obtained and the overall AEP gain is computed.

3.4.1 High-fidelity simulations

The Princess Amalia wind farm is simulated in SOWFA for 50 different sets of ambient conditions. In Figure 3.6, the relative power gains over time for different ambient conditions are given. The first 1200 seconds of the simulation are not considered in order to let

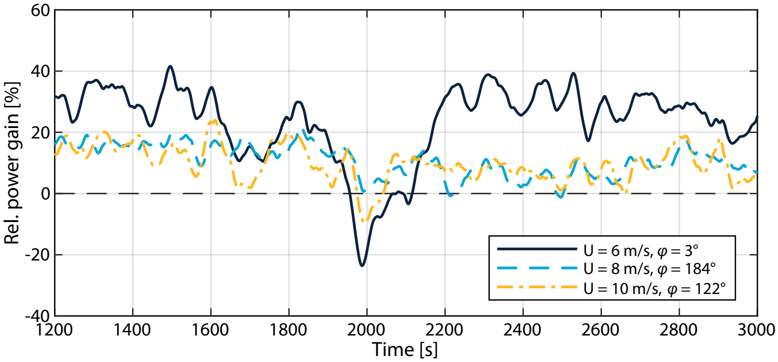

Figure 3.6: The relative power gain of the wind farm with wake steering over time for different ambient conditions.

the wakes propagate and remove any turbine start-up behavior. It can be seen that especially for wind speeds of $6\,\mathrm{m\,s^{-1}}$, wake steering shows larger gains than for higher wind speeds. This is believed to be partially the result of the turbine controller implementation of the NREL 5 MW turbine, which operates the turbine at a sub-optimal tip-speed ratio for wind speeds near cut-in. As the wind speed increases, the turbine starts operating closer to the optimal tip-speed ratio, thereby increasing the efficiency of the turbine. In this case, wake steering not only reduces the wind speed deficit for waked turbines, it also lets them operate more efficiently.

Wake steering can achieve large gains in power at specific time instants. In Figure 3.7, baseline operation is compared to wake steering for one of these instants. The figure clearly shows that wake steering is able to deflect the wake away from downstream turbines. Large negative gains are also observed for some periods of time in Figure 3.6. Due to the time-varying wind direction, the wind farm operates with unfavorable yaw orientations at times. This is visualized in Figure 3.8, where it can be seen that the yawed turbines redirect the wake into downstream turbines, resulting in a temporary decrease in power compared to baseline operation. Overall, the relative power gain remains significant, even in the presence of a time-varying wind direction.

3.4.2 Annual energy gain

To estimate the annual energy gain, the performance is evaluated robustly (Rott et al., 2018) (i.e., the optimal yaw angles are evaluated for different wind directions using the approach from Section 3.3.2). The resulting power gains computed with FLORIS are presented in Figure 3.9. The steady-state simulation results show six principal wind directions, corresponding to a turbine spacing of $7\,D$, where large gains in power are predicted. At an ambient wind speed of $4\,\mathrm{m\,s^{-1}}$, several turbines are not generating any power under baseline operation. However, with wake steering the wind speed increases above cut-in, resulting in large gains.

Next, the combined results from FLORIS and SOWFA are used to obtain a model of the energy gain through Gaussian process regression. Figure 3.10 presents the resulting Gaussian process model of the energy gain. The improved model shows increased gains

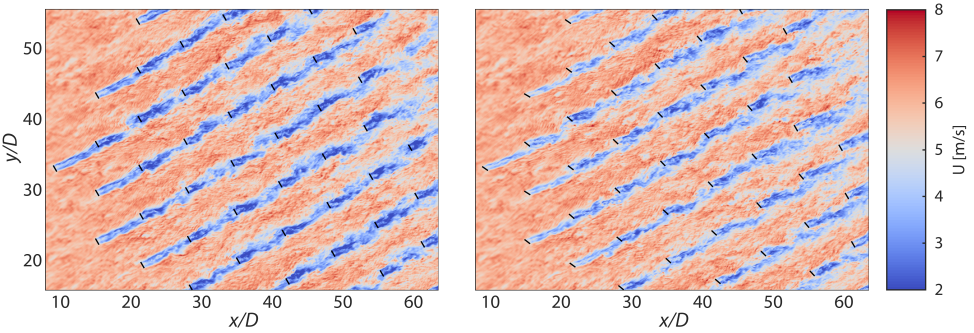

Figure 3.7: Streamwise velocity profile at turbine hub height of part of the wind farm with baseline operation (left) and wake steering (right) at time instant $t = 2250\,\mathrm{s}$, for $U_\infty = 6\,\mathrm{m\,s^{-1}}$ and $\phi_{avg} = 3°$.

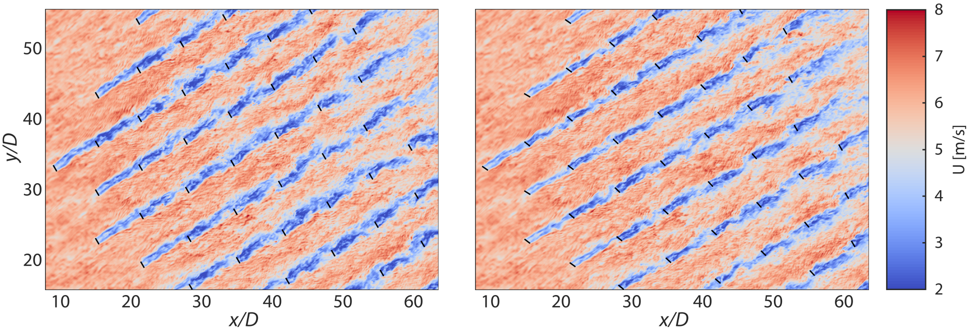

Figure 3.8: Streamwise velocity profile at turbine hub height of part of the wind farm with baseline operation (left) and wake steering (right) at time instant $t = 1980\,\mathrm{s}$, for $U_\infty = 6\,\mathrm{m\,s^{-1}}$ and $\phi_{avg} = 3°$.

for wind speeds of $6\,\mathrm{m\,s^{-1}}$ and above when compared to FLORIS. The Gaussian process model gives slightly smaller gains at lower wind speeds due to the regression with the SOWFA simulation data at $6\,\mathrm{m\,s^{-1}}$.

A more detailed comparison of the two models is provided in Figure 3.11. This figure shows the energy gain as a function of wind direction for a single wind speed. For wind directions where FLORIS predicted a high gain in power, the Gaussian process model shows gains that are up to twice as high. This large difference in power between the two simulation models can potentially be ascribed to the secondary steering effects (Martínez-Tossas et al., 2019), which are not modeled in our implementation of FLORIS. For the remaining wind directions, the simulation results from both simulation models are more in line.

Finally, the energy gains predicted by both models are combined with the wind distribution data to provide an estimate of the AEP benefit with wake steering. The resulting gains are presented in Table 3.2. The AEP benefit according to FLORIS is smaller compared to previously estimated values for the Princess Amalia wind farm, which were in the range of 1.10–1.28% (Fleming et al., 2016b; Kanev et al., 2018). This is because the AEP was evaluated robustly to account for a varying wind direction. With the improved energy gain model, the AEP benefit shows a 76% increase compared to FLORIS. This demonstrates

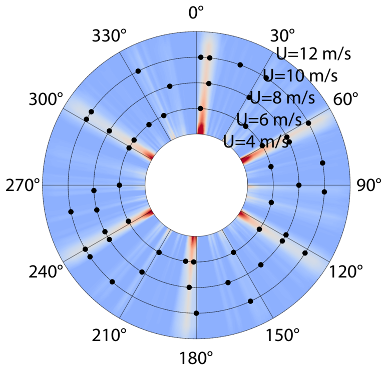

Figure 3.9: Power gains from wake steering acquired by robust evaluation of FLORIS. The black dots represent the cases that were evaluated in SOWFA.

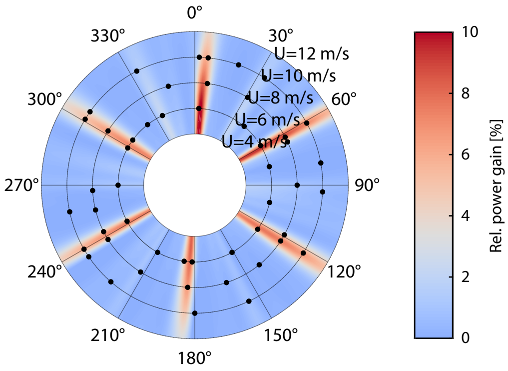

Figure 3.10: Power gains obtained through Gaussian process regression using the results from FLORIS and large eddy simulations. The black dots represent the cases that were evaluated in SOWFA.

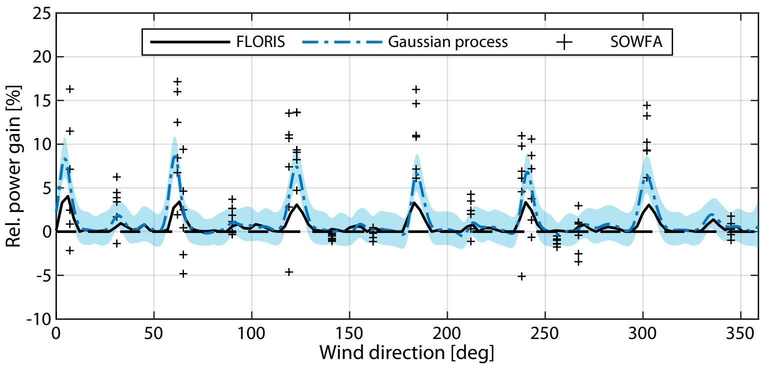

Figure 3.11: Relative power gain of the wind farm due to wake steering as a function of the wind direction, for a wind speed of $8\,\mathrm{m\,s^{-1}}$ and turbulence intensity of 5%. The light blue region indicates the 95% confidence bounds of the Gaussian process regression model.

the capability of the proposed framework for determining the AEP benefit. Furthermore, the difference between the two models emphasizes the need for further improvements to FLORIS, especially for large wind farms. Finally, it shows that wake steering can still be successful with a time-varying wind direction. In this study, the yaw setpoints were fixed for the entire duration of the simulation. By updating the yaw angles as the wind direction changes, higher power gains could be achieved.

Table 3.2: AEP benefit with wake steering according to FLORIS and the Gaussian process regression model.

Model	AEP gain
FLORIS	0.34%
Gaussian process model	0.60%

3.5 Conclusion

In this chapter, a novel framework was developed for determining the benefit of wake steering on the annual energy production of a large offshore wind farm. The framework used a simplified surrogate model to optimize the yaw angles and provide an initial estimate of the energy gain. Next, large eddy simulations incorporating a time-varying wind direction profile were performed for a subset of ambient conditions, to obtain a more accurate evaluation of wake steering. Simulation results from both models were subsequently used to fit a model of the energy gain through Gaussian process regression. The improved model showed a 0.60% gain in annual energy production. This is a 76% increase compared to the estimate obtained with the surrogate model. It is expected that higher gains can be achieved when the yaw angles are updated as the wind direction changes.

4

Experimental analysis of the effect of dynamic induction control on a wind turbine wake

Dynamic Induction Control (DIC) has proven to be an effective method of increasing the power output for a wind farm in both simulation studies and wind tunnel experiments. By pitching the blades of a wind turbine periodically, the recovery of the low-velocity wake is accelerated, thereby increasing the energy available to downstream turbines. The wake itself of a turbine operating with DIC has not yet been studied experimentally. This chapter presents a wind tunnel experiment where the wake of a wind turbine under periodic excitation is investigated. Using three-dimensional particle image velocimetry, the velocity field behind the turbine was reconstructed. Analysis of the velocity fields indicated that the available power in the wake increases when using DIC. This increase was partially due to a lower average thrust force experienced by the turbine with DIC. However, a large difference was seen between measurement results and actuator disk theory, indicating that enhanced recovery of the wake is contributing to the increased energy. Instantaneous measurements visualizing the development of blade tip vortices also showed how the location of vortex breakdown, which is directly related to re-energizing the wake, shifts over time with DIC. We believe this shifting location is contributing to the enhanced wake recovery of DIC, providing more energy to downstream wind turbines.

The contents of this chapter have previously appeared as a separate research article:
🗎 Hoek, D. van der, Frederik, J. A., Huang, M., Scarano, F., Simao Ferreira, C. J., and Wingerden, J. W. van (2022). “Experimental analysis of the effect of dynamic induction control on a wind turbine wake”. *Wind Energy Science* 7.3, pp. 1305–1320. DOI: `https://doi.org/10.5194/wes-7-1305-2022`.

4.1 Introduction

The area that is covered by (offshore) wind farms is often limited by technical or economic reasons, resulting in closely spaced wind turbines. While placing turbines close to each other leads to lower installation and maintenance costs, it also introduces energy losses due to the aerodynamic interaction between turbines. As a turbine extracts energy from the wind, a slower and more turbulent airflow is left in its wake. When multiple turbines are aligned with the incoming wind direction, they will experience the wake from upstream turbines. Current industry practice is to operate each wind turbine individually, so-called greedy control, thereby disregarding the impact of wakes on nearby turbines. This results in sub-optimal power production and increased structural loading of downstream turbines (Barthelmie et al., 2010; Kanev and Savenije, 2015).

Wake losses in wind farms can be partially mitigated by actively manipulating the wakes of upstream turbines using wind farm control (Boersma et al., 2017). Wind farm control methods can generally be categorized into wake redirection control and axial induction control (Kheirabadi and Nagamune, 2019). Wake redirection control usually refers to purposefully misaligning a turbine with the wind (e.g., Kanev et al., 2018). This changes the direction of the force applied by the turbine on the incoming airflow, thus deflecting the wake away from downstream turbines. While the misaligned turbines produce less power, the overall power generated by a farm increases (e.g., Gebraad et al., 2014b; Campagnolo et al., 2016a; Fleming et al., 2017a; Fleming et al., 2019a). Axial induction control distinguishes between static and dynamic methods. With SIC, the upstream turbine is derated to extract less energy from the wind, leaving more for downstream turbines (Kanev et al., 2018). Although steady-state wake models indicate a potential increase in power production using SIC (Annoni et al., 2016), high-fidelity simulations and field tests have shown either limited or no benefits (Annoni et al., 2016; Campagnolo et al., 2016a; Hoek et al., 2019; Frederik et al., 2020b). More promising results have been obtained using DIC, where the induction factor of a turbine is varied over time. This action is thought to induce additional turbulence in the wake of a turbine, which enhances mixing and subsequently results in faster wake recovery (Frederik et al., 2020b).

High-fidelity simulations have shown that it is possible to improve the power production of a wind farm by optimizing the control inputs for dynamic induction (Goit and Meyers, 2015; Munters and Meyers, 2017). However, finding the optimal excitation sequence is very computationally intensive. Goit and Meyers (2015) first applied this approach in large eddy simulations. The optimal thrust coefficient of the turbines over time was determined using the adjoint-based gradient, and implemented using a receding horizon approach. This turned out to be highly successful, increasing energy extraction by 16%. However, this method has several features that make it impossible to implement directly in a real-world environment. First, the objective function used in the optimization sequence requires perfect knowledge of the flow, which is not available in real life. Second, the computational time necessary for the gradient calculation was substantially larger than the receding horizon time window, which makes real-time implementation infeasible. Third, the authors controlled the turbine's thrust coefficient directly, whereas in practice it depends on multiple parameters, both internal (e.g., pitch angle, tip-speed ratio) and external (e.g., wind speed, turbulence).

Munters and Meyers (2018) addressed the first two challenges by introducing periodic thrust variations. Although this approach reduces the potential power gain slightly, it is more practical to implement. As the optimization is now limited to finding the optimal thrust amplitude and frequency, the computationally expensive optimization sequence is no longer needed. The final challenge is to translate the thrust coefficient variation into a control signal for the wind turbine. Frederik et al. (2020b) proposed a straightforward approach where a periodic variation of the pitch angle is superimposed on the baseline controller. While this approach slightly alters the applied thrust variation, wind tunnel experiments with a three-turbine array showed a similar wake mixing effect, leading to a 2–4% gain in power (Frederik et al., 2020b).

The experiments by Frederik et al. (2020b) demonstrated the potential benefit of DIC, but they only considered power measurements taken directly from the wind turbines. To the best of our knowledge, no experiments have been conducted thus far that characterize the aerodynamic behavior of a wind turbine wake in the DIC regime, which is vital to gain a better understanding of its physical working principle. The goal of this study is to investigate the effect of dynamic induction control on a wind turbine wake. To do this, the wake of a small-scale wind turbine model is measured using three-dimensional PIV, a technique used successfully in wind tunnel experiments to characterize the wake of scaled wind turbine models (e.g., Rockel et al., 2014; Lignarolo et al., 2014, among others).

The chapter is organized as follows. Section 4.2 presents the setup used for carrying out the experiments, which includes the turbine model, control strategy, and PIV system. In Section 4.3, the measurement results are shown in the form of flow fields. Some of the key measurement results are discussed further in Section 4.4. Finally, conclusions on the performance of DIC are given in Section 4.5.

4.2 Experimental setup

4.2.1 Wind tunnel and turbine model

The experiments were done in the Open Jet Facility (OJF) of the Aerospace Engineering Faculty at TU Delft. This is a closed-loop open jet wind tunnel with an octagonal outlet of 2.85 m by 2.85 m. The wind tunnel has a contraction ratio of 3:1, and can reach a free stream velocity of $35\,\mathrm{m\,s^{-1}}$ with a Turbulence Intensity (TI) between 0.5 and 2% (Lignarolo et al., 2015). The current experiments were conducted at a wind speed of $U_\infty = 4\,\mathrm{m\,s^{-1}}$.

The turbine model used for the experiments was the MoWiTO-0.6 developed at the University of Oldenburg (Schottler et al., 2016). This turbine has a rotor diameter of $D = 0.58\,\mathrm{m}$ and is equipped with a generator that allows torque control to regulate the rotor speed. A stepper motor attached to a spindle is used to pitch the blades collectively. An overview of the model including relevant dimensions is provided in Figure 4.1. To measure the deformation of the tower, strain gauges were applied at the bottom on the front and back in a full Wheatstone bridge configuration. The strain gauges were calibrated by hanging weights on the back of the nacelle, mimicking the force moment around the tower base originating from the thrust force. This process resulted in a linear expression of the tower moment as a function of the strain gauge voltage. This expression was used to reconstruct the thrust force acting on the rotor from the measured voltage. For additional information on the design of the wind turbine, see the paper by Schottler et al. (2016).

Communication between the wind turbine and computer was arranged with a *dSPACE*

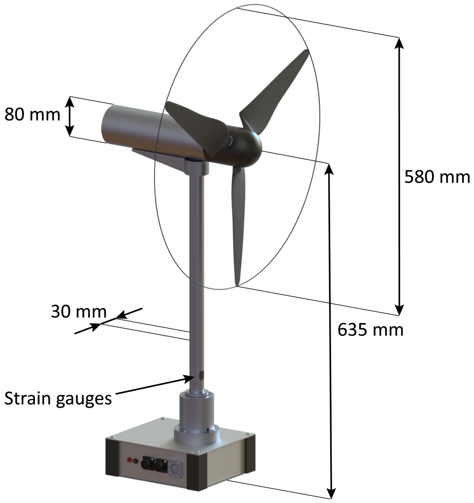

Figure 4.1: MoWiTO-0.6 wind turbine model including relevant dimensions.

MicroLabBox. The frequency for communication was set to 10 kHz, while measurements were recorded at a frequency of 1 kHz. Recorded turbine signals included the rotor speed, pitch angle, generator current, and strain at the tower base.

The steady-state aerodynamic coefficients, electrical power C_{P_e} and thrust C_T, were determined experimentally at the start of the measurement campaign for different tip-speed ratios and pitch angles. The electrical power P_e could be reconstructed from the generator current using a generator-specific constant (Schottler et al., 2016). The thrust force T was acquired by measuring the strain at the tower base and relating this to the linear calibration function. The measurements indicated that the turbine performed optimally for a tip-speed ratio of $\lambda_* = \Omega R/U_\infty = 5.5$, with rotor speed Ω, rotor radius R and wind speed U_∞. The coefficients C_{P_e} and C_T for this tip-speed ratio are given in Figure 4.2 for a range of pitch angles. The 0° pitch angle was defined as the most outward position that the blades could reach. For a blade pitch angle of $\theta_* = 9^\circ$ optimal power was achieved, while simultaneously guaranteeing a reasonable thrust coefficient. The contribution of the tower and nacelle to the thrust force was measured by removing the blades from the turbine, and was observed to consist of approximately 3% of the total thrust force at the optimal operating settings.

4.2.2 Dynamic induction control strategy

The wind turbine was operated with two different control methods. First, we used the classical *greedy* control approach, where a turbine maximizes its power output without considering interaction with other turbines. This control strategy served as a baseline for the second method, which was dynamic induction control.

For the baseline case, we implemented the simple *K-omega-squared* control strategy from (Bossanyi, 2000) to regulate the rotor speed. In this case, a generator torque is applied

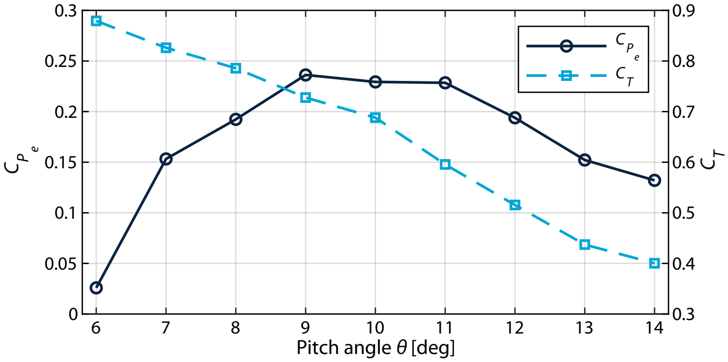

Figure 4.2: Experimentally determined power (C_{P_e}) and thrust (C_T) coefficients of the MoWiTO-0.6 for different pitch angles θ at the optimal tip-speed ratio $\lambda_* = 5.5$.

to the turbine according to the control law

$$Q_e = K\Omega^2, \tag{4.1}$$

where Q_e is the electrical torque. The desired torque was applied by the generator, which was in turn controlled by a shunt resistor. The controller gain K was based on the following relation for the optimal operating settings:

$$K = \frac{\rho_{\text{air}} \pi R^5 C_{P_e}(\lambda_*, \theta_*)}{2\lambda_*^3}, \tag{4.2}$$

with ρ_{air} indicating air density. Using this control law, the turbine should be operating at the top of its power coefficient curve (see Figure 4.2). The blade pitch was kept constant at the optimal value. Note that during the experiment, the turbine was only operated in the partial load region for which this control law is valid.

A similar controller to the one used by Frederik et al. (2020b) was implemented for dynamic induction control. This controller also used the control law from Equation (4.1) to regulate the rotor speed. Additionally, by imposing a sinusoidal signal on the collective blade pitch angles, the thrust coefficient of the turbine could be varied over time. The amplitude and frequency of these variations were limited by the bandwidth of the pitch motor.

Previous studies have indicated that the optimal pitch frequency is found for a particular range of Strouhal numbers, where the Strouhal number is defined as

$$\text{St} = \frac{fD}{U_\infty}, \tag{4.3}$$

with f the excitation frequency. Munters and Meyers (2018) used large eddy simulations to optimize the Strouhal number for periodic DIC and found a value of St = 0.25. Wind tunnel experiments carried out by Frederik et al. (2020b) used Strouhal numbers ranging from 0.1–0.4, and observed that the total power peaked for St values between 0.2–0.3. Note that the Strouhal definition implies that the excitation frequency scales with the turbine rotor diameter. For large wind turbines with rotor diameters of up to 180 m, this optimal Strouhal number results in a very low frequency (typically $\ll 0.1\,\mathrm{Hz}$). The corresponding pitch frequency for the MoWiTo-0.6 model is equal to $f = 1.72\,\mathrm{Hz}$. Initial testing with the turbine showed a maximum pitching speed around $16\,^\circ\,\mathrm{s}^{-1}$, limiting the pitch amplitude to 2.3° at St = 0.25. To ensure that a range of different frequencies around this reported optimal frequency could be tested, we varied the blade pitch angle between 8–12°. Note that this variation was not centered around the pitch angle of $\theta = 9^\circ$ that is used to achieve optimal power production. This steady offset in pitch angles between baseline operation and DIC is consistent with the implementation of Frederik et al. (2020b). Similar to their experiment, the original plan was to include a second turbine in the wake of the first turbine. This would have allowed us to directly measure the effect of DIC on the power of a downstream turbine. Due to some issues we experienced with the experiment setup, this turned out to be infeasible. Another reason for the steady offset in pitch angle was to ensure a higher thrust variation and a smaller loss of power according to the aerodynamic coefficients from Figure 4.2.

The periodic pitch signal resulted in a varying thrust coefficient with values between 0.52–0.79, which was a slightly lower amplitude than the cases presented in Frederik et al. (2020b). We expect smaller wake mixing effects due to the smaller variation in thrust. However, Frederik et al. (2020b) conducted their experiments at TIs of 5 and 10%, whereas the experiments presented here were conducted at a lower TI. A higher TI results in a higher amount of natural wake mixing, regardless of the wind turbine control action. Therefore, the low TI conditions ensured that only a small pitch action was needed to observe significant perturbations in the wake.

The evolution of the thrust coefficient over time with this sinusoidal pitch reference is depicted in Figure 4.3. This figure is based on the steady-state thrust coefficient from Figure 4.2, and merely illustrates the varying thrust signal. During the experiment, we expect slightly altered signals, since the thrust force is affected by dynamic inflow. Compared to the baseline case, a thrust coefficient above 0.72 is considered *over-inductive*: the induction is higher than the optimal in terms of steady-state energy capture. A similar variation from over-inductive to under-inductive thrust coefficients was used in previous research (Munters and Meyers, 2018; Frederik et al., 2020b). It is expected that these variations lead to increased turbulence in the wake and, subsequently, faster wake recovery.

The wind tunnel experiments from Frederik et al. (2020b) did not show a clear optimum over the Strouhal numbers. However, small differences in power gain were observed for different frequencies. In our experiment, we applied DIC at Strouhal numbers of 0.19, 0.24, and 0.29, deeming these sufficient for including the optimal Strouhal number with this particular setup.

4.2.3 Three-dimensional velocity measurements

The wake of the turbine was measured using a large-scale PIV system. An overview of the setup is shown in Figure 4.4. Helium-Filled Soap Bubbles (HFSBs) were used as flow tracers (Scarano et al., 2015). An aerodynamic seeding rake at the outlet of the open jet released a continuous stream of particles into the incoming flow. The seeder introduced additional disturbances to the flow (see e.g., Jux et al., 2018), but its position was deemed necessary for sufficient seeding of the measurement volume. Three *LaVision LED Flash-*

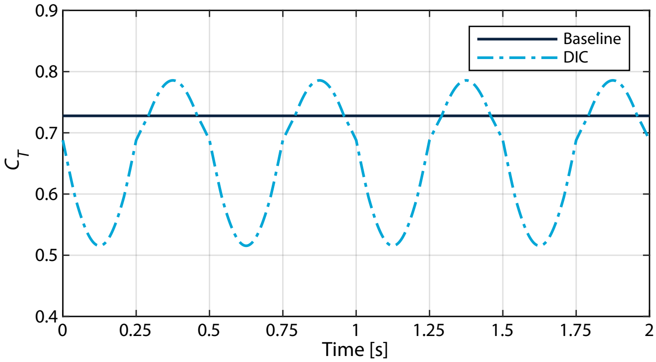

Figure 4.3: Thrust coefficient reference for baseline control and periodic dynamic induction with a frequency of 2 Hz (St = 0.29).

lights were used to illuminate the particles in the turbine wake. A setup consisting of three *Photron FASTCAM SA1.1* high-speed cameras recorded the light scattered by the seeding particles at a frequency of 500 Hz, with a resolution of 1024 by 1024 pixels. The Field of View (FOV) covered by the cameras was approximately $0.75 \times 0.5 \times 0.75\,\text{m}^3$. A *High-Speed Controller* from *LaVision* was used to synchronize the illumination and imaging. Each recording lasted 10 s, resulting in 5000 images for each measurement.

Processing the recorded images consisted of several steps. First, a high-pass filter was applied to the raw images to remove any undesired background light (Sciacchitano and Scarano, 2014). The filtered images were subsequently processed with the *DaVis 10* software from *LaVision*. This process included a self-calibration using recorded images to correct any misalignments between cameras and the measurement volume (Wieneke, 2008). Next, the motion of the tracers was obtained by tracking them individually (particle tracking velocimetry) using the efficient Shake-The-Box (STB) algorithm from Schanz

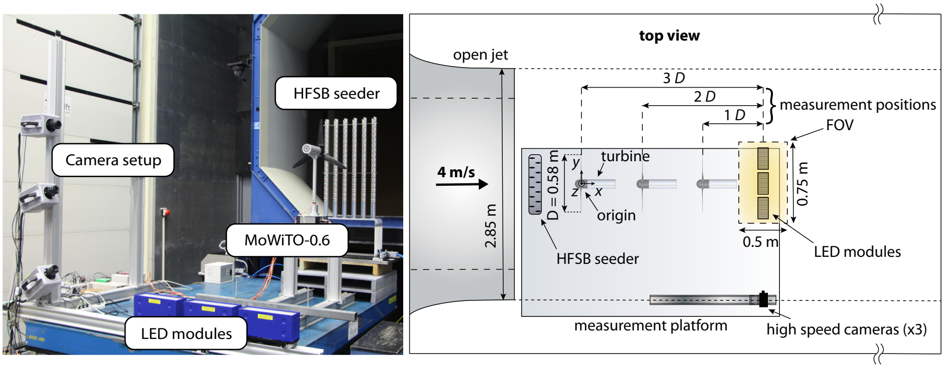

Figure 4.4: Experimental setup for measuring the wake using particle image velocimetry (left) and a schematic overview of the setup highlighting the different components and turbine locations used for measuring the wake (right).

et al. (2016). This algorithm reconstructs the particles' trajectories from the recorded data based on the principle of Lagrangian Particle Tracking (LPT), providing the velocity vector along trajectories in a three-dimensional domain. Finally, the scattered data from the particle positions and velocities was reduced onto a Cartesian grid by spatially averaging over small cubic cells (binning). Time-averaged velocity fields were rendered using a bin size of $50 \times 50 \times 50\,\mathrm{mm}^3$. A 75% overlap among neighboring bins yielded a final vector spacing of 12.5 mm. Instantaneous velocity fields were acquired using the Vortex-In-Cell Plus (VIC+) method (Schneiders and Scarano, 2016; Jeon et al., 2018). This method uses data assimilation, combining particle tracks with the vorticity transport equation, and offers more accurate results with a higher spatial resolution.

By moving the turbine to three different positions, as indicated in Figure 4.4, multiple regions along the wake were measured. The distance between the rotor plane and the center of the FOV was varied between one and three diameters D downstream, obtaining an effective measuring range of 0.5–$3.5\,D$. Repositioning the turbine instead of the measurement system was done to save time when carrying out the experiments, as this removed the need to calibrate the PIV system when different parts of the wake were measured. Lignarolo et al. (2014) measured the properties of the open jet for different locations downstream and found that the inflow velocity and turbulence intensity were affected due to the shear layer of the jet. Based on their analysis, we do not expect large deviations in mean inflow velocity but possibly a minor change in turbulence intensity when moving the turbine from 1–$4\,D$ with respect to the outlet of the jet. The presence of the HFSB seeder was expected to have a larger impact on the conditions upstream of the turbine, however, it is unknown how significant these changes were.

4.3 Results

This section presents the results obtained from the measurements described in the previous section. Section 4.3.1 contains the thrust coefficient measured at the turbine. In Section 4.3.2, we show the time-averaged flow fields at multiple distances behind the turbine. The velocity fields are averaged over the DIC pitch cycle in Section 4.3.3, providing a measure of the available power in the wake over time. Finally, instantaneous measurements are used to visualize the development of the blade tip vortices in Section 4.3.4.

4.3.1 Turbine thrust coefficient

The performance of the turbine at the three measurement positions was compared using the thrust force measured by strain gauges at the tower base. The measured thrust forces were transformed to thrust coefficients using

$$C_T = \frac{T}{\frac{1}{2}\rho\pi R^2 U_\infty^2}, \tag{4.4}$$

with thrust force T, air density ρ, and rotor radius R. A constant inflow velocity of $U_\infty = 4\,\mathrm{m\,s^{-1}}$, used for operating the wind tunnel, was used for the computation. Figure 4.5 shows C_T for the baseline case and one of the DIC cases (St = 0.24). We observe that the average C_T in both cases (baseline and DIC) was up to 20% lower compared to the expected values from Figure 4.3, which were based on the steady-state thrust coefficient.

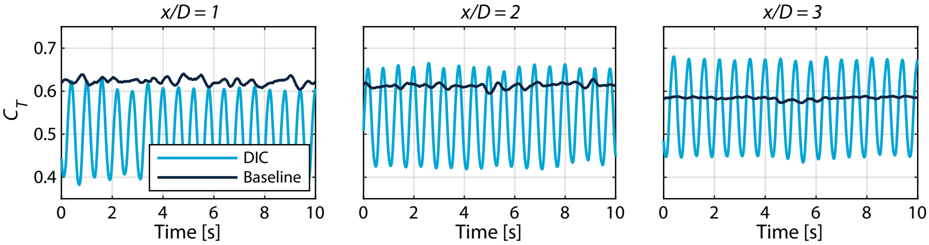

Figure 4.5: Thrust coefficient of the turbine for different measurement positions. The results are based on a single measurement for each distance using either baseline control or DIC with St = 0.24.

Furthermore, we see that the difference in average thrust coefficient between baseline and DIC varied depending on the location of the turbine. The average C_T decreased for the baseline case, whereas it increased for the DIC case.

We believe there are several explanations for the variations in the measured C_T. First, the HFSB seeding rake was not present when the aerodynamic coefficients from Figure 4.2 were obtained. This could indicate that the seeding rake affected the incoming flow. Furthermore, we expect that the influence of the seeding rake changes depending on how close the turbine is positioned to it. Measurements of the wind field without a turbine were taken at a distance of $4\,D$ from the seeder, indicating a largely unaltered mean inflow velocity and an average turbulence intensity of 5%. Unfortunately, there is no information on the actual inflow conditions at each of the turbine positions. Second, the relatively low wind speed used for the experiments introduced some unsteadiness in the inflow, and was also more susceptible to measurement errors in the wind speed at the outlet of the open jet. Finally, the turbine controller was designed using the aerodynamic coefficients that were obtained without the seeding rake. In the DIC case, the rotor speed varied periodically due to the pitch action, making it more difficult for the controller to operate the turbine at the optimal tip-speed ratio.

The measurements shown in Figure 4.5 make it clear that the flow fields from different turbine positions should be evaluated carefully. Due to the relative difference in C_T between the baseline case and DIC, we are comparing different cases at each turbine location. However, we believe the principles behind dynamic induction control can still be investigated through these measurements, in particular the effect of DIC on tip vortex development, which we believe to be independent of the average thrust force, that is addressed in Section 4.3.4.

4.3.2 Time-averaged flow fields

Time-averaged flow fields were obtained from the binning procedure described in Section 4.2.3, using all the particle data from each measurement. Contours of the stream-wise velocity field at multiple cross-sections downstream are presented in Figure 4.6. A clear difference in the velocity deficit was observed between baseline control and DIC with St = 0.24. The results of the other pitch frequencies are not shown, as the relative differences in average velocity were minor. The coordinate system used in these figures is the same as specified in Figure 4.4. Due to the combination of a lower average induction factor

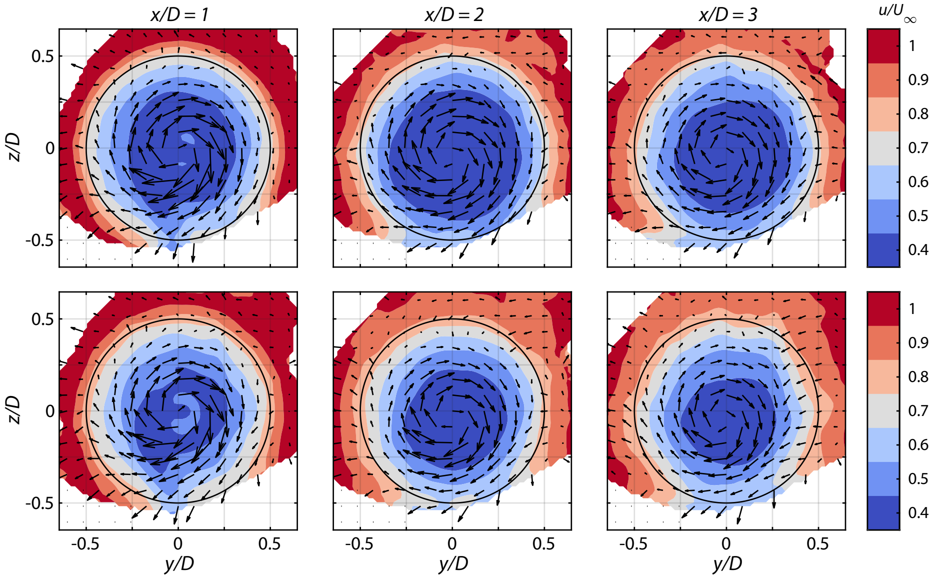

Figure 4.6: Cross-sections of the wake at distances ranging from 1 to 3 diameters downstream of a turbine operating with baseline control (top) and DIC with St = 0.24 (bottom). The contours show the average normalized stream-wise velocity component, while the arrows indicate the cross-stream velocity components. The black circles indicate the relative location of the rotor disk of the model wind turbine.

and the periodic excitation, the average stream-wise velocity in the wake of the turbine operating with DIC was higher than in the baseline control case. This is seen for all three measurement locations.

The measurements from different locations are merged into a single velocity field in Figure 4.7. Data from the different measurement positions does not overlap, but the transitions between these measurements seem relatively smooth, even though the turbine experienced different thrust levels. When subtracting the flow fields from the baseline and DIC case, we see clearly that there is a lower velocity deficit in most parts of the wake as a result of DIC. The increase in velocity is primarily concentrated at the edges of the wake, except at one side ($y/D < 0$) around $x/D = 3$. This asymmetry in the wake might be related to the development of the tower wake, which will be addressed later on.

The time-averaged velocity fields show that the velocity, and hence the energy in the wake increased when DIC was used. Using these flow fields, we cannot discern the contributions to the increased velocity of the periodic excitation or the lower average thrust force. However, we can get an indication of how DIC affects the recovery of the wake by inspecting the turbulence intensity. The turbulence intensity is defined relative to the undisturbed inflow velocity U_∞ as

$$\mathrm{TI} = \frac{\sqrt{\frac{1}{3}\sum_{i=1}^{3} \overline{u_i' u_i'}}}{U_\infty}, \tag{4.5}$$

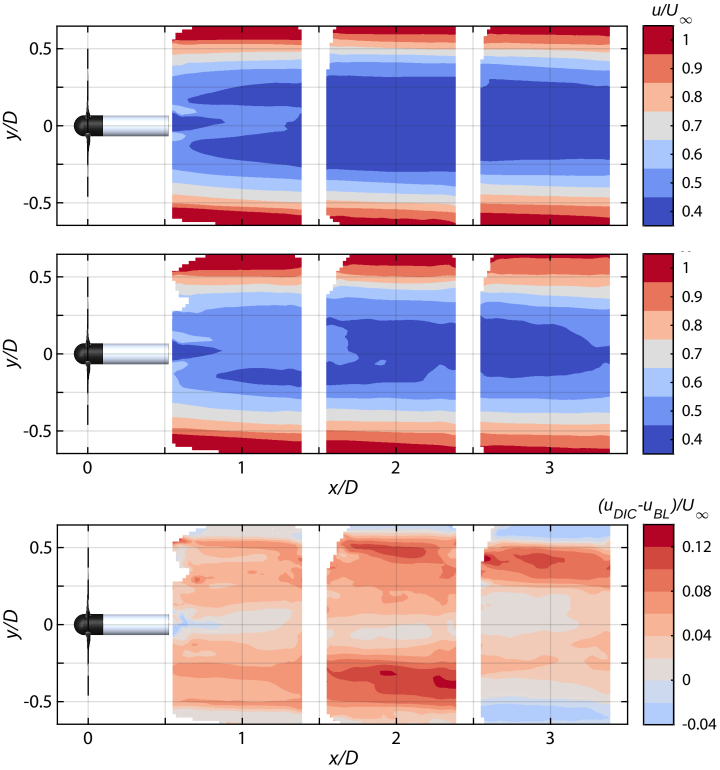

Figure 4.7: Contours of the stream-wise velocity component u/U_∞ in the wake of the turbine at hub height ($z/D = 0$), operating with baseline control (top) and DIC (St = 0.24) (middle). The difference in velocity field between the two control methods is visualized in the bottom figure.

with

$$\overline{u_i' u_i'} = \frac{\sum_{k=1}^{N} \left(u_i(t_k) - \overline{u_i}\right)^2}{N} \tag{4.6}$$

indicating the variance for each of the three velocity components. The TI at multiple locations in the wake is presented in Figure 4.8. For the baseline case, we observe high TI values concentrated at the edge of the wake due to vortices released at the blade tips. The effect of these vortices spread out further downstream as the vortices started interacting with each other. Furthermore, high turbulence levels were present behind the turbine nacelle and tower. Although the influence of the tower seemed to diminish when moving downstream, the lower left quarter of the wake shows that vortices shed by the tower started interacting with the blade tip vortices. Comparing the contours from the baseline operation with DIC, similar TI values were found at $x/D = 1$. From a distance of $x/D = 2$ and onwards, increased turbulence levels for DIC are visible in large parts of the wake, and moving towards the center.

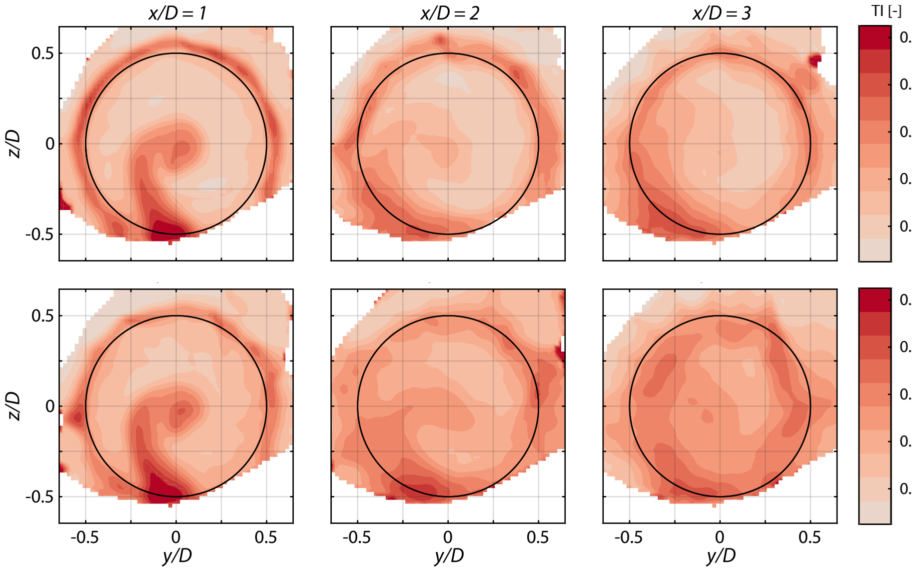

Figure 4.8: Turbulence intensity (TI) contours at multiple locations in the wake of a turbine operating with baseline control (top) and DIC with St = 0.24 (bottom).

4.3.3 Periodically averaged velocity and available power

This section investigates the effect of DIC on the velocity in the wake over a pitch cycle. Using the function of Available Power (AP) from Vollmer et al. (2016), we can quantify how the energy in the wake varied over time. The periodically averaged flow fields were obtained by dividing the instantaneous velocity fields over different phases of the pitch cycle. For a turbine pitching at a frequency of 2 Hz (St = 0.29), this resulted in 250 measurements for a single pitch cycle (i.e., the pitch cycle was discretized in 250 phase segments). For each of these pitch phases, the data of all pitch cycles was subsequently averaged using the following equation to obtain a higher statistical convergence:

$$u_{\mathrm{pa}}(\theta_{\mathrm{ph}}, x, y, z) = \frac{1}{n_{\mathrm{c}}} \sum_{\theta_{\mathrm{ph}}} u(\theta(t), x, y, z). \tag{4.7}$$

Here, u_{pa} is the periodic average of the velocity for a phase of the pitch cycle θ_{ph}, n_c represents the number of pitch cycles, and u is the velocity as a function of the pitch angle θ at any time t. Depending on the Strouhal number, this means that the number of pitch cycles used for averaging ranged from 13–20. Phase-locked measurements are generally acquired with particle image velocimetry by timing the imaging with the principle frequency of excitation, which is usually the rotational frequency of the turbine (e.g., Lignarolo et al., 2014). However, since the pitch frequency did not always coincide with the rotor frequency, and the latter was not constant when DIC was activated, this was not a valid option for this experiment.

The result of the periodical averaging approach is shown in Figure 4.9. For the baseline case, the averaging was done over a single revolution of the rotor. The resulting velocity field looks quite similar to the ones from the time-averaged figures. The velocity fields with DIC are shown at three different phases of the pitch cycle, which are indicated by the relative angle of the blades. Large differences in the velocity field over time were observed. Following a low pitch angle, corresponding to a high thrust force, the wake expanded, and a region of high-velocity deficit (dark blue) was induced behind the turbine. As thrust decreased, the wake contracted while a comparatively lower velocity deficit was induced behind the turbine.

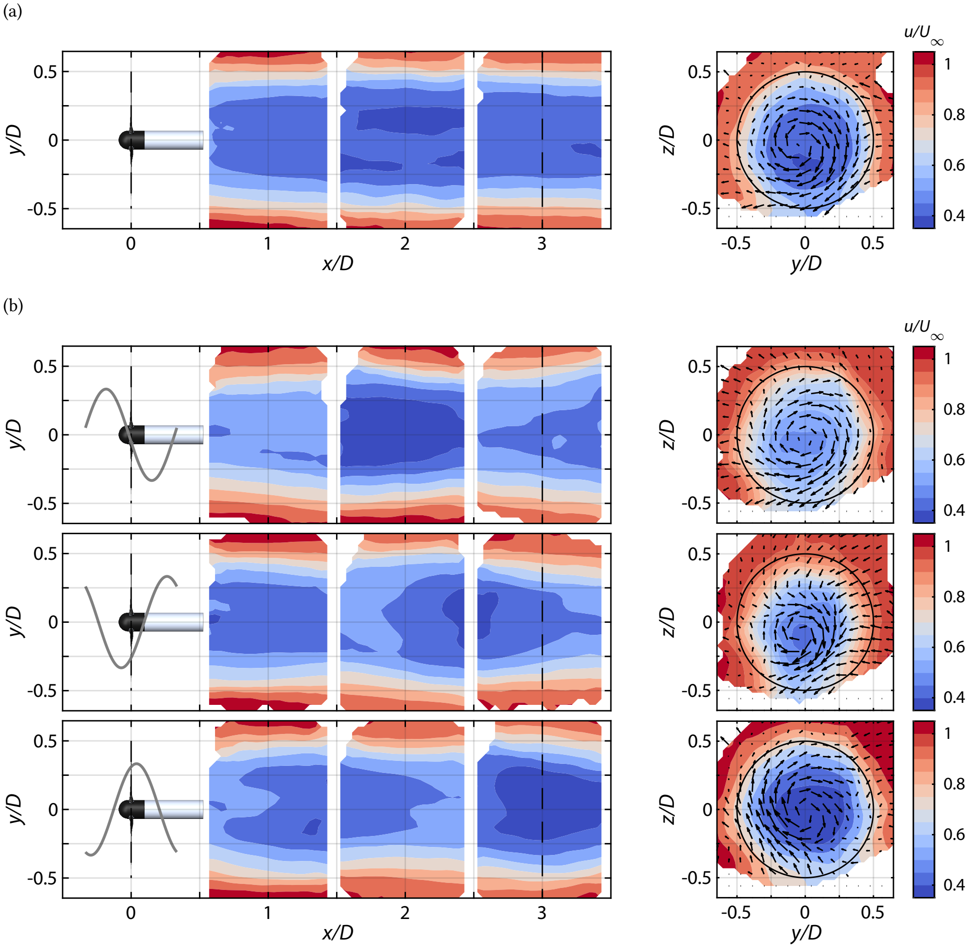

Figure 4.9: Cross-section of the periodically averaged wake at hub height ($z/D = 0$) and at three diameters downstream of a turbine operating with (a) baseline control and (b) DIC (St = 0.24). The contours show the normalized stream-wise velocity components and the arrows indicate the cross-stream velocity components. The grey line indicates the pitch angle at different phases of the pitch cycle.

Next, the effect of DIC was evaluated using the fraction of AP as defined by Vollmer et al. (2016):

$$f_{\mathrm{AP}}(x) = \int_0^{2\pi} \int_0^R u_{\mathrm{pa}}^3(x, r, \psi)/U_\infty^3 r \mathrm{d}r \mathrm{d}\psi. \tag{4.8}$$

Here, x denotes the distance downstream, while r and ψ indicate the radial distance and azimuth angle. The equation provides the power available to a hypothetical downstream wind turbine with respect to the upstream turbine that is driven by an undisturbed flow. By applying this equation to the phase-averaged data at a distance of $x/D = 3$ downstream, the f_{AP} over time is obtained in Figure 4.10 for all Strouhal numbers. From the figure, it is clear that the AP downstream increased significantly for each implementation of DIC, compared to baseline operation. Small differences were observed between the different Strouhal numbers, such as the minima and maxima of the f_{AP}. Furthermore, it seems the pitching frequency affected the average traveling speed of the low-velocity wake region, as can be seen from the time shift of the signals.

The fraction of AP was subsequently computed for the entire measurement volume and averaged over time to obtain Figure 4.11. The figure indicates that the AP was initially still relatively high, since the wake had not fully expanded yet. The available power reached its minimum between $x/D = 1.5–2$, after which it started to recover slowly. The different pitch frequencies for DIC showed only small differences on average; no clear optimum for the Strouhal number is observed based on the present results. The first two measurement positions, $x/D = 1$ and 2, showed a similar trend in the difference between the baseline controller and DIC. However, at $x/D = 3$ we see a relative increase in the f_{AP} for the baseline case. This was something that could be expected when looking at the turbine thrust measurements from Figure 4.5, where the relative thrust coefficient between baseline and DIC was a lot smaller at this measurement location.

Using the average AP from Figure 4.11, we can also make a simplified calculation of the efficiency of a potential two-turbine array. By assuming that the hypothetical downstream turbine is operating with the optimal C_{P_e} from Figure 4.2, the power of the downstream turbine can be determined and added to the power of the upstream turbine to obtain a measure of the array power efficiency. The individual and total power coefficients for a hypothetical turbine located at $x/D = 3$ are given in Figure 4.12. Note that the average

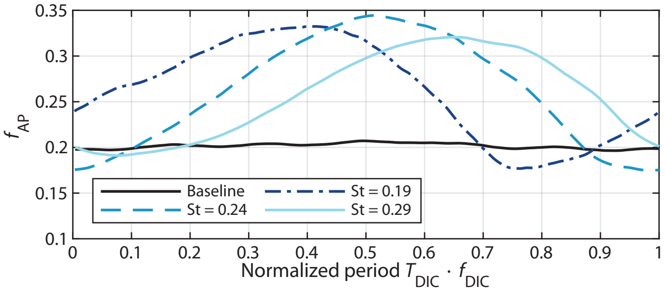

Figure 4.10: Available power f_{AP} over time at a distance of $x/D = 3$. The results have been normalized over time using the corresponding pitch frequencies to compare the results over a single pitch cycle. The different measurements have been synchronized using the pitch reference signal.

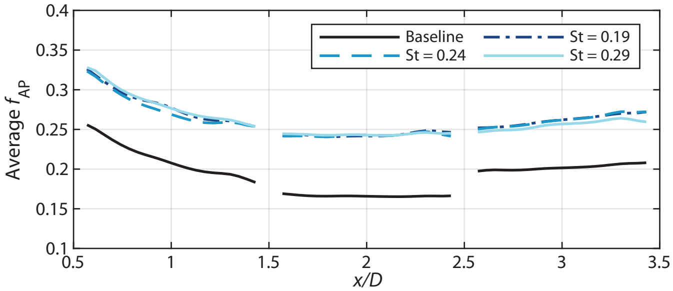

Figure 4.11: Average available power $\bar{f}_{AP}$ in the wake of a turbine operated with DIC compared to baseline operation. The $\bar{f}_{AP}$ is based on cross-sections of the measured stream-wise velocity field.

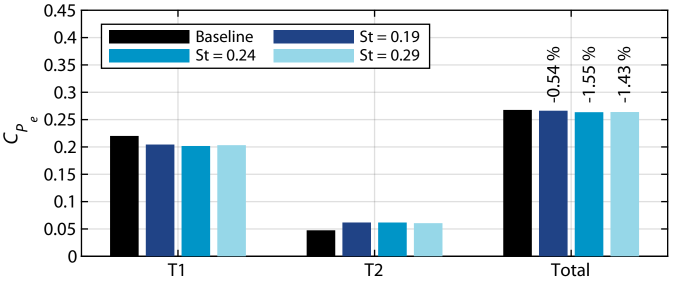

Figure 4.12: Average power coefficient C_{P_e} comparing baseline control with DIC for three different frequencies. The first column shows the power of the measurement turbine, the second column shows the power of a hypothetical turbine located at a distance of $x/D = 3$ in the wake, and the final column shows the combined power of T1 and T2.

thrust force of the two control methods was almost equal at this location, allowing a more straightforward comparison of their individual results. When comparing the total power coefficient of the baseline case to DIC, we see that DIC was slightly less effective. This was mostly due to the amount of energy lost at the operated turbine, which was higher than in other studies (Frederik et al., 2020b).

The comparison of the total power coefficient from Fig. 4.12 provides some insight into the effectiveness of DIC, but it relies on several assumptions. An additional evaluation can be made using one-dimensional actuator disk theory to compare the measurement results to a simple theoretical framework. In this case, the velocity in the wake of the turbine is assumed to depend solely on the induction factor, and recovery due to turbulence is neglected. The induction factor and corresponding wake velocity are given by

$$a = \frac{1}{2}\left(1 - \sqrt{1 - C_T}\right), \tag{4.9}$$

$$u_w^{\mathrm{AD}} = (1 - 2a)U_\infty, \tag{4.10}$$

where a is the induction factor and u_w^{AD} is the wake velocity according to actuator disk theory. For this theoretical wake velocity, we also determined the f_{AP} to compare it to the measurement results. The comparison between actuator disk theory and the PIV measurements is provided in Table 4.1. The average difference between the measured thrust forces among the various measurement cases is seen to be very small, resulting in very similar f_{AP} values for the actuator disk model. We do see some differences in the amplitude of the different DIC frequencies, indicating that the pitch frequency is also affecting the thrust amplitude. Regarding the f_{AP} from the PIV measurements, much larger differences are observed between baseline and DIC. Here, a clear increase in the AP is found when DIC is being used. The difference in values between actuator disk theory and the PIV measurements seems to suggest that a large part of the increased energy in the wake is due to enhanced wake recovery induced by the periodic excitation from DIC.

Table 4.1: Comparison of wake properties for a hypothetical turbine at $x/D = 3$ downstream with DIC compared to baseline operation. The different columns indicate values of the Strouhal number St, average thrust coefficient $\bar{C}_T$, thrust amplitude ΔC_T, average induction factor a, wake velocity based actuator disk theory $u_{\mathrm{w}}^{\mathrm{AD}}$, fraction of AP based on actuator disk theory $f_{\mathrm{AP}}^{\mathrm{AD}}$, and fraction of AP based on the PIV measurements $f_{\mathrm{AP}}^{\mathrm{PIV}}$.

Control strategy	St	$\bar{C}_T$	ΔC_T	a	$u_{\mathrm{w}}^{\mathrm{AD}}$	$f_{\mathrm{AP}}^{\mathrm{AD}}$	$f_{\mathrm{AP}}^{\mathrm{PIV}}$
Baseline	-	0.58	-	0.18	2.57	0.27	0.20
DIC	0.19	0.57	0.13	0.17	2.60	0.28	0.26
	0.24	0.56	0.12	0.17	2.64	0.29	0.26
	0.29	0.56	0.10	0.17	2.64	0.29	0.26

4.3.4 Tip vortex development

The phase-averaged velocity fields allowed us to investigate some of the periodic behavior inside the wake. However, a large part of the dynamics is lost due to the averaging procedure. An additional study of the instantaneous data was made to find more information on the wake mechanics of DIC. Processing the measurements using VIC+ (Schneiders and Scarano, 2016; Jeon et al., 2018), we were able to obtain time-resolved velocity fields at a grid spacing of 15 mm. After processing the PIV measurements, the Q-criterion was computed from the acquired velocity components to identify the vortical structures in the wake (Hunt et al., 1988). This allowed us to visualize the vortices generated at the tips and roots of the blades in Figures 4.13 and 4.14. The first figure shows the development of the vortices over time for baseline operation, while the second figure shows how the vortices develop over time at different stages of the pitch cycle with DIC. In the baseline case, we observe how each of the vortices shed by the blades traveled downstream without much interaction around $x/D = 1$. However, moving further downstream it becomes apparent that starting at $x/D = 2$, the first two vortices started interacting. At this point, the vortices were so close to each other that they started having a reciprocal influence, causing them to roll up around one another. This process is called leapfrogging, due to the phenomenon where the first vortex jumps back underneath the two trailing vortices. The leapfrogging event continued around $x/D = 3$, where we observe that the first two vortices have rolled up underneath the last trailing vortex. Leapfrogging plays an important role in the recovery of a wind turbine wake. The wake turbulence induced after the vortex breakdown has been shown to lead to positive entrainment of kinetic energy into the wake (Lignarolo et al., 2014).

Since the breakdown of the tip vortices has a strong influence on the recovery of the wake, it is interesting to look at the difference in the leapfrogging process with DIC. The first time instant from Figure 4.14 shows the wake as the pitch angle is traveling from its minimum position, which is associated with the highest thrust force. Initially, we observe that the vortices start interacting at a later stage than in the baseline case. However, as the stronger vortices that were shed when the thrust force was at its peak traveled downstream, it is seen that the leapfrogging location moved upstream. Furthermore, the figure shows that the leapfrogging process is no longer sequential, but that the three vortices start rolling up all at once. At the third frame, a single vortex is observed before $x/D = 3$, consisting of three successive tip vortices. As the pitch angle increased and thrust force went down, the strength of the vortices decreased and the location of the leapfrogging event shifted downstream again. From these visualizations, it becomes evident that DIC has a large influence on the breakdown of tip vortices and the accompanying re-energizing of the wake.

4.4 Discussion

The results from the PIV measurements were investigated from three different perspectives: from a time-averaged, periodic, and instantaneous point of view. Especially for the time-averaged results it should be recalled that there was a steady offset in the thrust coefficient experienced by the turbine during baseline operation and DIC. Hence, the improved velocity fields for DIC do not provide sufficient evidence for the effectiveness of this control approach. However, it should be noted that during the experiment the difference in average thrust levels was smaller than anticipated (see Figure 4.5). Due to the changing wind turbine position, small differences in adjacent parts of the velocity fields were observed. This is particularly the case when we examine the difference in streamwise velocity at $x/D = 3$ in Figure 4.7.

The time-averaged data did show increased TI levels towards the center of the wake as a result of applying DIC (see Figure 4.8). Since atmospheric turbulence is a key driver for wake recovery, we believe that the additional turbulence induced by DIC stimulates wake mixing, leading to a higher energy content. The TI contours also made it apparent that the influence of the wind turbine's tower and nacelle on the wake was significant and not exclusive to the lower half of the wake. We observe how high turbulence levels behind the tower were sucked upward to around hub height due to the rotation of the wake. This observation corroborates findings from high-fidelity simulations (Santoni et al., 2017) and field measurements (Abraham et al., 2019), which showed that both tower and nacelle play an important role in the recovery of the wake, especially in the far wake. The results presented in this study not only visualize these effects, but also show that the turbulence caused by the tower and nacelle is enhanced by DIC. We believe this to be an important observation, one that should be taken into account in future studies into axial induction control. This holds especially true for high-fidelity simulation studies, which often omit the nacelle and tower structures for practical reasons.

Periodically averaged velocity fields were used to determine the hypothetical available power for a second turbine at $x/D = 3$. This measurement was subsequently averaged over time to obtain the total power of an array with a second hypothetical turbine. The difference in the total power turned out to be minor and in favor of the baseline operation.

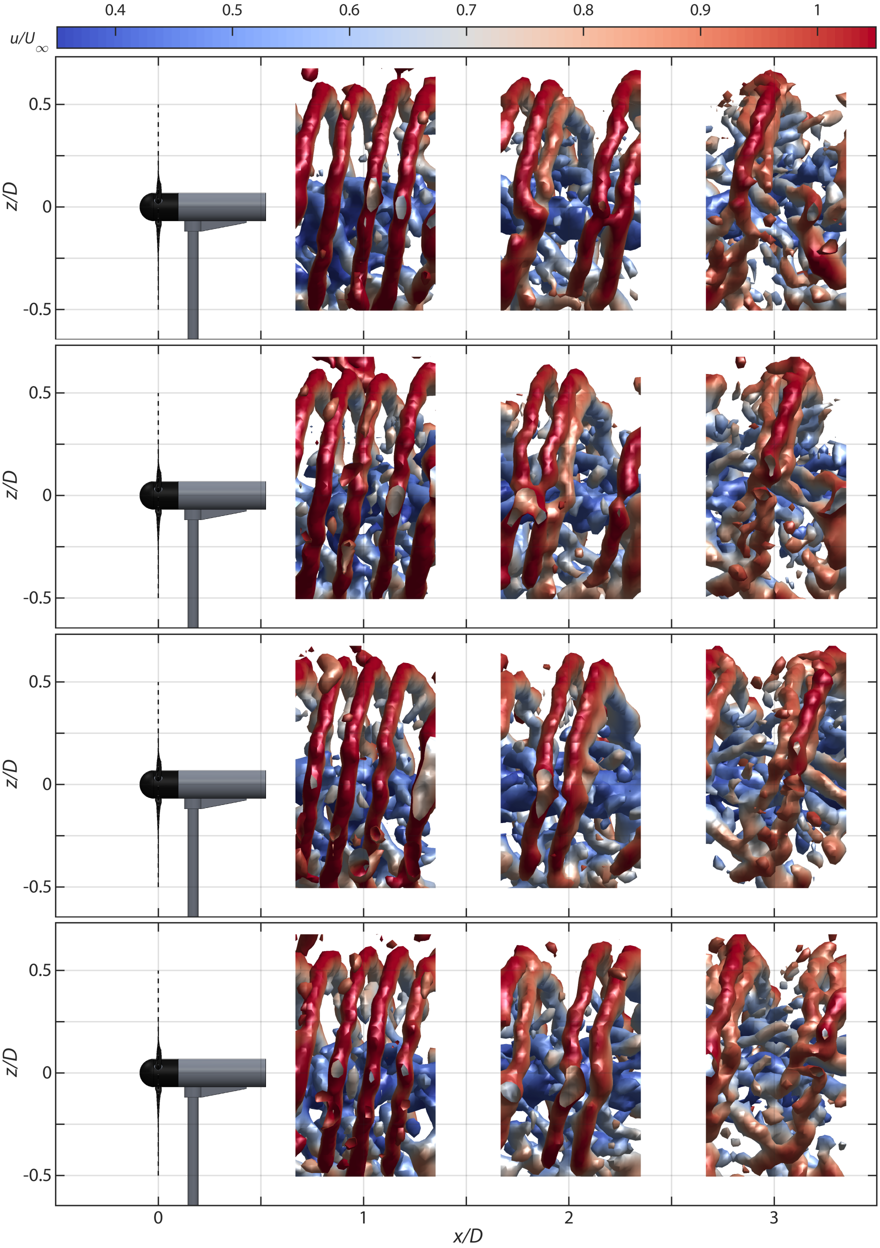

Figure 4.13: Isosurfaces of the instantaneous normalized Q-criterion ($QD^2/U_\infty^2 = 1$) visualizing the blade tip vortices for baseline operation. The different snapshots are separated by $\Delta t = 0.02\,\mathrm{s}$, coinciding with $t/T_r = [0, 0.24, 0.48, 0.72]$. Here, T_r represents the time it takes to complete one full rotation. The colors of the isosurfaces correspond to the normalized stream-wise velocity component.

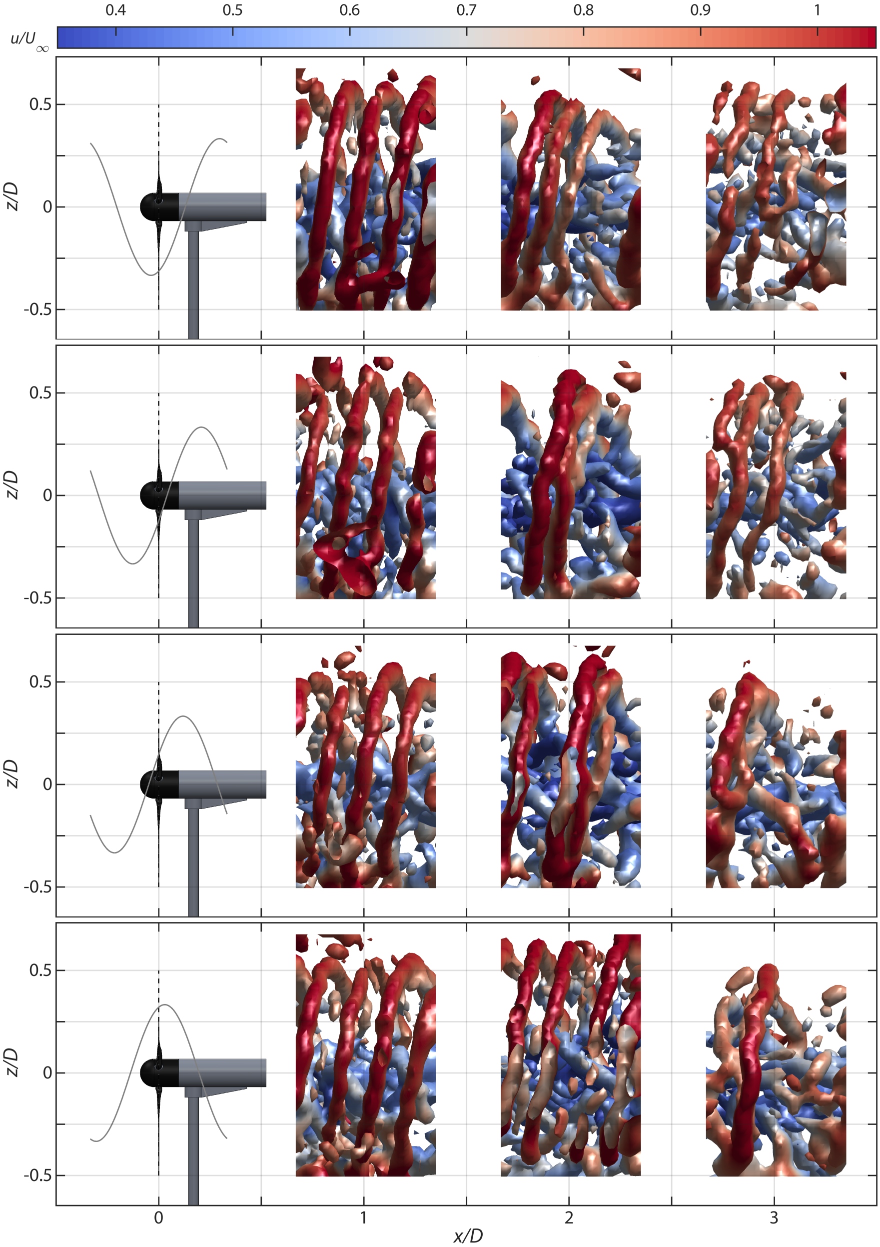

Figure 4.14: Isosurfaces of the instantaneous normalized Q-criterion ($QD^2/U_\infty^2 = 1$) visualizing the blade tip vortices for operation with DIC (St = 0.19). The different snapshots are separated by $\Delta t = 0.1\,\mathrm{s}$, coinciding with $t/T_e = [0, 0.13, 0.27, 0.4]$. Here, T_e refers to the time it takes to complete a single DIC cycle. The colors of the isosurfaces correspond to the normalized stream-wise velocity component, while the grey line indicates the current pitch angle.

This was partially due to the relatively high power loss (approximately 10%) of the model wind turbine when it was pitching. We expect the power loss to be lower for large-scale wind turbines, which have less steep power curves. Furthermore, the loss can be partially ascribed to the f_{AP} of the baseline control case at $x/D = 3$, which was above the expected trend of the AP obtained from the measurements at $x/D = 1$ and 2. As mentioned before, we believe this trend break was a result of the varying average thrust experienced at the different measurement positions.

Based on the phase-averaged velocity fields we can conclude that the stream-wise velocity increased when a periodic forcing component was applied to the flow. Furthermore, the results presented in Table 4.1 show that the increase in mass flow or energy was higher than expected based on the average thrust levels. The exact cause behind the increased energy levels in the wake is difficult to pinpoint. However, simulations and experiments have indicated that wake recovery is related to the location of the blade tip vortex breakdown (Lignarolo et al., 2014; Lignarolo et al., 2015; Marten et al., 2020). From the instantaneous measurements we can observe that the leapfrogging event for the baseline case was completed around $x/D = 3$. When applying DIC, we see how the strength of the vortices was affected directly. The stronger vortices accelerated the instability that led to the leapfrogging event and the subsequent vortex breakdown. As a result, we see that the location of the vortex breakdown changed over time, ranging from $x/D \approx 2$ to $x/D > 3$. Based on these observations, we believe that the wake recovery starts at an earlier stage at some time instants and is spread out over a larger part of the wake when DIC is used. In contrast, the wake starts recovering at a fixed location for the baseline case, achieving a lower overall recovery. While the difference in average thrust between baseline and DIC makes it difficult to directly compare all measurement results, we believe the analysis of the tip vortices is not affected heavily. If anything, implementing DIC at a higher average thrust would likely have triggered the leapfrogging event at an earlier stage.

Finally, we will also use this section to briefly discuss some of the challenges that were encountered during the experiment. Our desire for large-scale PIV measurements meant a turbine of limited size, while also being capable of exciting the wake through a pitch action of the blades. The turbine used in this experiment was able to meet this desire, but due to limitations of the pitch actuators it was not possible to measure at inflow wind speeds $U_\infty > 4\,\mathrm{m\,s^{-1}}$. Operating the open jet at this velocity introduces some unsteadiness to the flow, and the true wind speed measurement at the outlet of the jet is susceptible to measurement errors. The large measurement volume also required the HFSB seeding rake to be positioned in front of the jet in order to cover a large volume with flow tracers. Based on the measurements from Figure 4.5, we believe the effect of the seeding rake is not to be ignored. Indeed, an increase in turbulence intensity was observed when the flow was measured without the turbine present. Not only did the measured thrust levels differ from the experimentally determined thrust coefficient seen in Figure 4.2, but they also varied depending on the measurement position of the turbine. For the sake of consistency across measurements, future experiments would do better by operating the turbine at a fixed location, while moving the PIV setup to cover different parts of the wake.

4.5 Conclusions

In this chapter, we investigated the wake of a small-scale wind turbine ($D = 0.58\,\mathrm{m}$) operating with DIC. Measurements of the wake, ranging from $0.5–3.5\,D$ downstream, were taken using particle image velocimetry with helium-filled soap bubbles. The results with DIC were compared to those from a baseline controller. While the baseline controller maximizes the individual turbine power output, DIC aims to optimize the overall wind park output. Three different pitching frequencies were used for DIC at Strouhal numbers of St = 0.19, 0.24, and 0.29.

When applying DIC, time-averaged measurements showed a decrease in the wake velocity deficit, which was partially due to a lower average thrust force. The periodic excitation also resulted in higher turbulence levels towards the center of the wake compared to baseline control, indicating enhanced wake recovery. Averaging the velocity data over a single pitch cycle showed a low-velocity region traveling downstream causing the wake to expand and contract locally. The available power f_{AP} of a hypothetical turbine downstream was subsequently computed using these velocity fields, showing minor variations in power for the different Strouhal numbers. The measurements were also compared against one-dimensional actuator disk theory. Where the latter showed similar levels of f_{AP} between baseline control and DIC, a clear increase in available power with DIC was observed from the measurements. This is an additional indication of the enhanced wake recovery due to the periodic excitation.

Finally, the development of blade tip vortices was visualized using the Q-criterion. These figures identified the locations of the leapfrogging process and subsequent breakdown of vortices, which strongly influence wake mixing and hence the re-energizing of the wake. For the baseline case, we observed a stable region for the leapfrogging event between $x/D = 2$ and 3. On the other hand, DIC resulted in a periodically changing location depending on the thrust force of the turbine. Furthermore, changes in the leapfrogging process itself were observed as three successive vortices started interacting simultaneously. This alternative way of vortex breakdown is presumably one of the main drivers behind the enhanced wake recovery of periodic dynamic induction control: The effective wake recovery location is brought forward and expanded over a larger area. Further research in this area, both experimental and through simulations, is required to improve our understanding of this mechanism.

This study showed that dynamic induction control increased the wind speed and turbulence intensity in the wake. The periodic thrust force continuously changed the location of vortex breakdown, leading to enhanced wake recovery. The experimental results can be used to improve modeling dynamic excitations of the wake, with the goal of increasing the efficiency of large-scale wind farms.

5

Experimental validation and wake analysis of the helix approach

Wind farm control can play a key role in reducing the negative impact of wakes on wind turbine power production. The helix approach is a recent innovation in the field of wind farm control, which employs individual blade pitch control to induce a helical velocity profile in a wind turbine wake. This forced meandering of the wake has turned out to be very effective for the recovery of the wake, increasing the power output of downstream turbines by a significant amount. This chapter presents a wind tunnel study with two scaled wind turbine models, of which the upstream turbine is operated with the helix approach. We used tomographic particle image velocimetry to study the dynamic behavior of the wake under the influence of the helix excitation. The measured flow fields confirm the wake recovery capabilities of the helix approach compared to normal operation. Additional emphasis is put on the effect of the helix approach on the breakdown of blade tip vortices, a process that plays an important role in re-energizing the wake. Measurements indicate that the breakdown of tip vortices, and the resulting destabilization of the wake is enhanced significantly with the helix approach. Finally, turbine measurements show that the helix approach was able to increase the combined power for this particular two-turbine setup by as much as 15%.

The contents of this chapter have previously been submitted as a separate research article:
🗎 Hoek, D. van der, Van den Abbeele, B., Simao Ferreira, C. J., and Wingerden, J. W. van (2023). "Maximizing wind farm power output with the helix approach – experimental validation and wake analysis using tomographic PIV". *Wind Energy*, under review. DOI: `https://doi.org/10.48550/arXiv.2306.12849`.

5.1 Introduction

Wakes generated by upstream turbines can negatively impact the performance of downstream turbines and the wind farm as a whole. They contribute to significant losses in energy and increased loading of structural components (Barthelmie et al., 2009; Barthelmie et al., 2013). While conventional industry practice takes these negative aspects for granted, there are ways to, at least partially, mitigate wake effects. Wind farm control can play a key role in reducing wake effects by actively influencing the airflow behind turbines. Three wind farm control categories are generally recognized (Wingerden et al., 2020; Meyers et al., 2022; Houck, 2022). *Static induction control* (SIC) adjusts the induction factor of the turbine either by introducing an offset in the blade pitch angle or running the turbine at a sub-optimal tip speed ratio (Kanev et al., 2018; Houck, 2022). While SIC has proven capable of providing grid services (Aho et al., 2012; Fleming et al., 2016a; Vali et al., 2017b) and decreasing structural loading (Fleming et al., 2016c; Hoek et al., 2018), applying it for maximizing power has seen less convincing results (Annoni et al., 2016; Campagnolo et al., 2016b; Hoek et al., 2019; Frederik et al., 2020b). The second category is called *wake steering*, and has been shown numerous times to be capable of increasing the power output of wind turbine arrays. By misaligning upstream turbines with respect to the incoming wind and redirecting the wake away from downstream turbines, the latter are able to extract more power and more than overcome the losses incurred by the yaw misalignment (Gebraad et al., 2014b; Campagnolo et al., 2016b; Fleming et al., 2017a; Fleming et al., 2019b; Fleming et al., 2021; Howland et al., 2019; Howland et al., 2022; Doekemeijer et al., 2021). The last five years have seen an increasing interest in the third category, which is often referred to as *dynamic induction control* (DIC) or *wake mixing*. Methods belonging to this category make continuous adjustments to the turbines' operating setpoints to increase the level of mixing in the wake, and thereby enhance its dissipation. In this study, we will also focus on a method from this category.

DIC was first applied in large eddy simulations through dynamic variations of a wind turbine's induction factor, and showed large increases in power output (Goit and Meyers, 2015; Munters and Meyers, 2017). A simplified implementation of this concept was introduced by Munters and Meyers (2018), consisting of a periodic variation in thrust which only depends on an optimal amplitude and frequency. Frederik et al., 2020b tested this method in the wind tunnel on a three-turbine array by feeding a sinusoidal pitch reference signal to the upstream turbine. Depending on the frequency and, more importantly, the amplitude of the pitch reference, power gains in the range of 2 % were observed. Several studies on the wake recovery mechanism of dynamic induction control were made using both simulations (Yılmaz and Meyers, 2018; Brown et al., 2022; Croce et al., 2022b) and wind tunnel experiments (Hoek et al., 2022). These studies all showed that dynamic thrust adjustments affect the pairing behavior of subsequent blade tip vortices, a process that is closely associated with re-energizing the wake (Lignarolo et al., 2014). When active, DIC accelerates the vortex pairing, creating a region of high vorticity around which the surrounding flow rolls up. Subsequently, higher energy flow is entrained into the wake.

An extension of the previous method was presented by Frederik et al. (2020a), where they used dynamic individual pitch control (DIPC) to induce periodic yaw and tilt moments on the rotor plane. Due to the imposed phase difference in yaw and tilt moments, the location of the thrust force varies periodically around the center of the rotor plane with a near-constant radius. This leads to a helical structure in the velocity profile of the wake, for which this technique was dubbed the *helix approach*. By periodically pitching the blades at a slightly lower or higher frequency than the rotor frequency, a clockwise (CW) or counterclockwise (CCW) helix shape is created. Large eddy simulations with both uniform and turbulent inflow showed that this type of actuation can be very successful in enhancing wake mixing and was able to increase the power output of a two-turbine array up to 7.5 %.

The helix approach was further explored with large eddy simulations in terms of finding the optimal excitation frequency (Muscari et al., 2022) and amplitude (Korb et al., 2021; Taschner et al., 2023). The optimal frequency, usually expressed by the dimensionless Strouhal number (St), was found to be higher compared to DIC with collective pitch actuation. As for the optimal amplitude, Taschner et al. (2023) detected no saturation in the power gain in low turbulence conditions for pitch amplitudes of up to 6°, indicating that the power gains will primarily be limited by the level of turbulence and the allowed increase in structural loading caused by the helix approach. Korb et al. (2023) used large eddy simulations to investigate the wake of a single turbine and concluded that the helix approach is responsible for both increased mixing and significant wake deflection. Furthermore, simulations with three turbines demonstrated how phase differences between the helical wakes can have a significant impact on the power performance. Aero-elastic simulations have indicated significant increases in the fatigue loading of both blades and tower of the actuated turbine with the helix approach, although not as significant as in the case of DIC (Frederik and Wingerden, 2022; Taschner et al., 2023; Vondelen et al., 2023). The loads of the downstream turbine were also seen to increase by a small amount, but not comparable to the actuated turbine.

Previous work on the helix approach all agrees that the technique is most efficient in the CCW direction when considering power maximization. A similar comparison between the two helix counterparts was also made by Coquelet (2022), who simulated the performance of the helix approach using a vortex-particle-mesh code. These simulations once more showed the superiority of the CCW helix over the CW version. However, the simulation results also indicated that the potential power gain of the helix decreases significantly as the resolution of the simulations increases. This suggests that previously reported gains obtained through large eddy simulations might be largely overestimated, and in the case of the CW helix might not even be present.

The work from Coquelet (2022) highlights the importance of validating wind farm control methods in real-life scenarios, starting with wind tunnel experiments and followed by field testing. This standpoint is reinforced by experts in both academia and industry, who rank a lack of validation as the primary barrier to implementing wind farm control methods on commercial wind farms (Wingerden et al., 2020). A first step in the validation of the helix approach was taken by Heckmeier (2022), who successfully implemented it in the wind tunnel on a two-turbine array. A multi-hole pressure probe was used to measure the velocity profile of a horizontal slice of the wake, indicating increased wake recovery. While these measurements allowed for a phase-locked representation of the wake based on the azimuthal position of the blades, the true transient behavior of the helix approach was not observed.

In this chapter, we present an experimental investigation of the helix approach implemented on a scaled wind turbine model. Individual pitch control can be problematic for small-scale turbines, both due to limited space for actuators as well as higher pitch rates. To overcome this challenge, the turbine was equipped with a swashplate that enables cyclic pitch adjustments. We further expand upon the experiments carried out by Heckmeier (2022). Using a similar two-wind turbine setup, a full three-dimensional, quasi-time-resolved characterization of the wake is obtained using particle image velocimetry (PIV). The quasi-time-resolved nature of the measurement results was obtained by phase averaging the PIV data based on both the rotor azimuth angle and the phase of the helix approach. This approach differs from the work of Heckmeier (2022), which only considered phase averaged measurements based on rotor azimuth angle, thereby obscuring the tip vortex interaction at different phases of the helix excitation. Similar to previous experimental studies that incorporated PIV to investigate tip vortex interaction and the entrainment of kinetic energy into the wake (e.g., Cal et al., 2010; Rockel et al., 2014; Lignarolo et al., 2015), we will investigate how the helix method affects these aspects. This study will contribute in a major way to the existing literature in two ways. First, the work is seen as another important validation of the helix approach using an alternative turbine model and in a different wind tunnel. A contribution that will hopefully help pave the way to future field testing. Second, the PIV measurements allow for an extensive analysis of the dynamic behavior in the wake as a result of the helix approach, shedding more light on its working principles.

5.2 Experiment setup

5.2.1 Wind turbine model

For this experiment, we used two MoWiTO-0.6 wind turbines developed by the University of Oldenburg (Schottler et al., 2016). The turbine has a rotor diameter of $D = 0.58\,\mathrm{m}$. The rotor speed can be controlled by regulating the generator torque. The standard turbine model is equipped with a single stepper motor that pitches the blades collectively. To achieve the necessary individual pitch action required for replicating the helix approach, some adjustments to the turbine were made. Due to the dimensions of the turbine, using three motors to drive each pitch bearing directly was not a feasible option. The solution was to implement a swashplate mechanism that is commonly used in helicopters.

A visualization of the swashplate design is given in Figure 5.1. The swashplate consists of a non-rotating part that is actuated by three stepper motors driving three control rods along threaded shafts. The rotating component of the swashplate is connected to the blade mounting mechanism using three pitch links. Both swashplate components are fitted on the rotor shaft using spherical bearings, allowing a sufficient range of motion. By tilting the lower swashplate to an arbitrary position, the upper swashplate is forced to assume the same position, which in turn leads to a different pitch setting for each of the three blades. When the rotor is spinning, this will automatically result in a sinusoidal adjustment of the pitch angle of each blade over a single revolution.

The deformation of the tower in the fore-aft direction was measured using a set of strain gauges applied to the bottom of the tower. The strain gauges were connected in a full Wheatstone bridge configuration, with strain expressed as a single voltage measurement. Prior to testing, the strain gauges were calibrated to obtain an expression of the bending

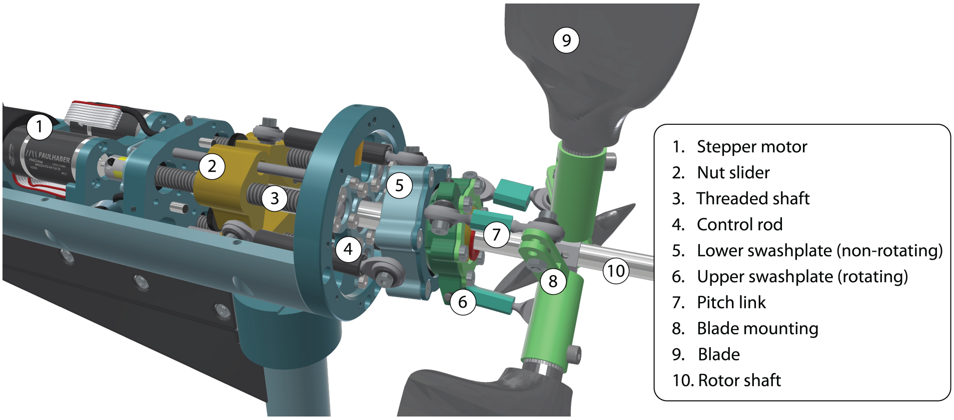

Figure 5.1: Overview of the swashplate design listing all the involved components. The stepper motors are used to move nut sliders over a threaded shaft, which are in turn connected to the lower swashplate. The upper swashplate assumes the same orientation as the lower swashplate, resulting in different pitch angles for each blade.

moment at the tower base as a function of voltage.

The control inputs for the stepper motors and generator torque were sent through a *dSPACE MicroLabBox* real-time system, which was also connected to a computer. A SIMULINK model used for operating the wind turbine was compiled on the *dSPACE* system, which was called to send and receive data using a MATLAB script. Communication took place at a frequency of 2 kHz, where besides sending the control input signals, sensor data was acquired of the stepper motor encoders, generator current, generator speed, rotor azimuth position, and tower bottom strain. At the start of the experimental campaign, the optimal operating conditions were determined empirically for both turbines. The power coefficient was determined using the measured generator current, which was multiplied by a generator-specific torque constant and the rotor speed to obtain electrical power (Schottler et al., 2016). The power coefficient was seen reaching its maximum value of $C_{P_e} \approx 0.27$ with a blade pitch angle of $\theta = 10^\circ$, and a tip-speed ratio of $\lambda = \Omega R / U_\infty = 5$. Here, Ω refers to the rotor speed, R the rotor radius, and U_∞ the free stream inflow velocity. The definition of the pitch angle is based on assigning a 0° pitch angle to the most outward position the blades could be pitched to (i.e., pitched fully into the incoming flow). The generator torque of both turbines was regulated in two different ways. For the upstream turbine, we wanted to avoid any effect a varying rotor speed could have on the thrust force. Hence, a straightforward proportional-integral feedback controller was implemented to regulate the torque based on the measured rotor speed, ensuring a near-constant rotor speed, and consequently a constant λ, during all measurements. For the downstream turbine, the incoming flow velocity was unknown, meaning that the previous strategy could not be implemented. To optimize the power extraction for the downstream turbine, the torque was regulated based on the measured rotor speed with the $K\Omega^2$-control law (Bossanyi, 2000).

5.2.2 Implementing the helix approach

With the adjusted turbine model presented in the previous section, actuating the turbine to recreate the helix is relatively straightforward. The original helix control strategy used the multi-blade coordinate (MBC) transformation (Bir, 2008) to transform the varying tilt and yaw moments into inputs for the pitch controller. The swashplate can be viewed as a mechanical counterpart to the MBC transformation, meaning that we only have to supply the desired frequency and amplitude of the swashplate motion as inputs to our wind turbine. Since the swashplate actuators are spaced 120° apart, moving the swashplate periodically in a CW or CCW motion requires applying a sinusoidal reference to all stepper motors, with offsets of ±120° and ±240° to the second and third motors relative to the first. In this case, a positive offset results in a clockwise movement of the swashplate when viewing the turbine from the front. An example of the control inputs is provided on the left side of Figure 5.2.

An initial study into the optimal amplitude and frequency of the swashplate motion was performed prior to the PIV measurements. By varying the amplitude and frequency, and recording the combined power of the two turbines, the settings were found that resulted in optimal power extraction at a wind speed of $U_\infty = 5\,\mathrm{m\,s^{-1}}$. The highest power gain for the CW case was found with an amplitude of 180° on the stepper motors, while an amplitude of 216° showed the largest gain for the CCW case. It has to be noted that the latter was the highest amplitude the stepper motors were able to reach at this particular wind speed, without faults being introduced in the tracking of the reference signals. The optimal excitation frequencies f_e, expressed by the Strouhal number $\mathrm{St} = f_e D/U_\infty$, were determined experimentally at $\mathrm{St} = 0.34$ ($f_e = 0.21 f_r$) and $\mathrm{St} = 0.28$ ($f_e = 0.18 f_r$) for the CW and CCW helix cases, respectively. Here, f_r represents the rotational frequency of the turbine. The resulting excitation frequencies are close to the optimal frequency of $f_e = 0.18 f_r$ reported by Heckmeier (2022). For the PIV measurements, we therefore decided to implement both helix cases at these optimal frequencies, while using an amplitude of 180° for the stepper motor actuation to compare both methods. Additional measurements were also taken for a CCW_{opt} case with an amplitude of 216°.

Measurements of the actual blade pitch angles were taken after the experimental campaign. By fitting a potentiometer directly to each of the blade mounting mechanisms seen

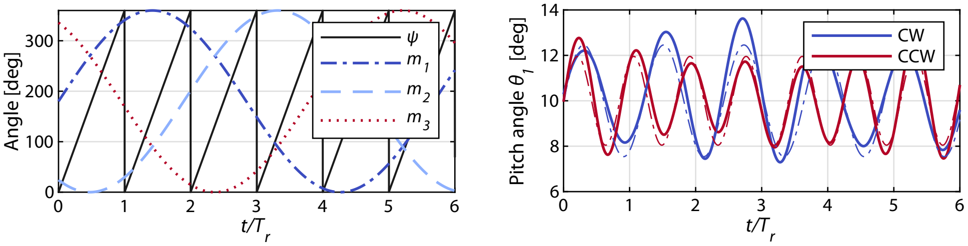

Figure 5.2: The left figure shows an example of CCW actuation of the three stepper motors (m_1, m_2, and m_3) used for controlling the motion of the swashplate. The black line indicates the rotor azimuth angle ψ. The right figure shows a comparison between a CW and CCW motion of the swashplate and the resulting pitch angles for one of the blades. The dashed lines show the ideal pitch actuation based on the average pitch amplitude of both helix cases. In both figures, time t is normalized by the turbine rotation period T_r.

in Figure 5.1, the pitch angles were recorded for different azimuth positions and orientations of the swashplate. The evolution of the pitch angle of a single blade over time is presented on the right-hand side of Figure 5.2 for one amplitude of the stepper motors. This figure shows the difference in pitch rates of the two methods. As the swashplate is moving in the CW direction, similar to the rotational direction of the rotor, the blades are not able to complete a full pitch cycle over a single rotation of the rotor. The opposite is true for the CCW case, resulting in a pitch frequency that is slightly higher than the rotational frequency. Apart from the differences in pitch rate, one can also observe that for both methods the amplitude varies over time. This is the result of some compromises that were made when designing the swashplate to allow sufficient freedom of movement. The dashed lines in the figure show the ideal pitch angles based on the average amplitudes that were measured using the potentiometer. An unexpected property of the swashplate design is that for a single motor amplitude, the resulting pitch amplitudes for the CW and CCW direction are not equal (i.e., the swashplate experiences more/less freedom of movement depending on the direction it is moving). The difference in average pitch amplitude between test cases is something that should be considered when analyzing the measurement results in Section 5.3.

The variation of the blade pitch amplitude over time will also have an impact on the quality of the yaw and tilt moments that are being exerted on the incoming flow. We can observe the extent of this variation using the MBC transformation (Bir, 2008)

$$\begin{bmatrix} \theta_0(t) \\ \theta_{\text{tilt}}(t) \\ \theta_{\text{yaw}}(t) \end{bmatrix} = \frac{2}{3} \begin{bmatrix} 0.5 & 0.5 & 0.5 \\ \cos(\psi) & \cos(\psi + \frac{2}{3}\pi) & \cos(\psi + \frac{4}{3}\pi) \\ \sin(\psi) & \sin(\psi + \frac{2}{3}\pi) & \sin(\psi + \frac{4}{3}\pi) \end{bmatrix} \begin{bmatrix} \theta_1(t) \\ \theta_2(t) \\ \theta_3(t) \end{bmatrix}, \tag{5.1}$$

where θ_0, θ_{tilt}, and θ_{yaw} represent the fixed reference frame collective, tilt and yaw angles. Figure 5.3 presents the transformed tilt and yaw angles for the CCW helix based on the measured pitch angles. The measured angles are compared to the ideal tilt and yaw reference angles, shown by the dashed lines, in case of a constant amplitude on the blade pitch inputs. From the figure, it is evident that the swashplate can move the pitch angles in such a way as to obtain a 90° offset between the tilt and yaw angles. While the tilt angle shows a good fit to the ideal reference, it seems that some imperfections in the swashplate design result in a small bias for the yaw angle. Based on this, a small warping of the helix velocity profile can be expected.

5.2.3 Wind tunnel experiment design

The experiment was carried out at TU Delft's Open Jet Facility. The wind tunnel consists of an octagonal-shaped open jet with dimensions of 2.85 m by 2.85 m, which is run in a closed circuit. The flow is passed through a radiator system to keep the flow temperature near constant. Before exiting the jet, the flow is contracted by a 3:1 ratio, reaching velocities of up to $35\,\mathrm{m\,s^{-1}}$ at turbulence intensities (TI) ranging between 0.5–2 % (Lignarolo et al., 2015). During all measurements of the experimental campaign, the wind tunnel was operated at a constant velocity of $U_\infty = 5\,\mathrm{m\,s^{-1}}$.

The two MoWiTO-0.6 turbines were placed on a large platform, set apart by a distance of 5 rotor diameters (D), similar to other studies on the helix approach (Frederik

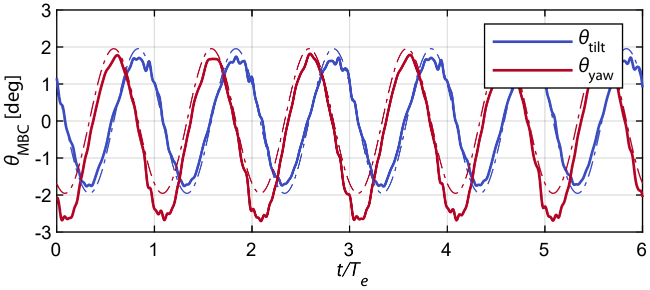

Figure 5.3: Fixed frame tilt and yaw angles for the CCW helix implementation as a function of time normalized by the excitation period $T_e = 1/f_e$. The dashed lines show the ideal tilt and yaw angles, in the case of a constant amplitude of the pitch angles in the rotating reference frame.

et al., 2020a; Heckmeier, 2022). The remaining measurement equipment is illustrated in Figure 5.4. A seeding rake was placed at the outlet of the open jet, releasing neutrally buoyant helium-filled soap bubbles (HFSBs), with an average diameter of 0.4 mm, that were used as flow tracers over an area 0.6 m wide by 0.9 m high (Scarano et al., 2015). On their way downstream, the flow tracers were illuminated by two *LaVision LED Flashlights*. The resulting reflections were recorded by a tomographic PIV system consisting of four *Photron FASTCAM SA1.1* high-speed cameras, operating with a framerate of 500 frames/s and at a resolution of 1024 by 1024 pixels. Each recording acquired 5,000 frames, resulting in approximately 24 cycles of the helix approach. Synchronization between cameras and LEDs was arranged using a *LaVision PTU-X* timing device. The measurement domain was divided into seven smaller volumes of size 0.4 x 0.7 x 0.7 m^3, which were covered by moving the construction on which the cameras and LEDs were mounted. The measurement volumes overlapped in the streamwise direction (x), resulting in a total volume of 2.1 x 0.7 x 0.7 m^3 and covering a portion of the turbine wake ranging from 0.7–4.3 D. The resulting image resolution was equal to 1.99 pixels/mm.

An overview of all the test cases that were measured is presented in Table 5.1. Different implementations of the helix approach were compared to a baseline case, where both turbines were operated using *greedy* control. This control strategy is standard industry practice and is referred to as greedy, because the turbine aims to maximize its own power production. In doing so, it disregards any impact it has on turbines operating in its wake.

Table 5.1: All test cases that were considered for the PIV measurements, indicating the Strouhal number, average pitch amplitude A_θ, the total number of frames that were recorded for each measurement volume, and the total number of helix cycles that were completed during the measurements.

Test case	Strouhal nr.	A_θ	# frames	# helix cycles
Baseline (greedy)	n.a.	n.a.	10,000	n.a.
Helix CW	0.34	2.5°	15,000	82
Helix CCW	0.28	2.0°	15,000	72
Helix CCW$_{opt}$	0.28	2.4°	5,000	24

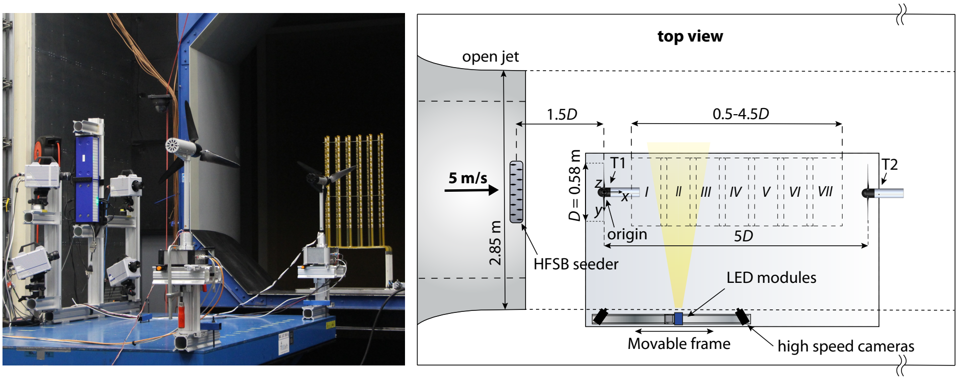

Figure 5.4: Overview of the experimental setup, highlighting the different components and the measured sections of the wake. The field of views indicated by the numbers *I–VII* are centered at distances of $1 : 0.5 : 4D$ behind the upstream wind turbine. The cameras and LEDs were mounted on a frame that could be moved along the platform accordingly.

The PIV data was processed using *LaVision's DaVis 10* software. A high-pass filter was applied to the raw data to reduce any background illumination (Sciacchitano and Scarano, 2014). A geometrical mapping of the camera positions relative to the measurement domain was obtained using a calibration plate, followed by a volume self-calibration (Wieneke, 2008) to reduce the residual measurement errors below 0.1 pixels. Next, we reconstructed the flow tracers with the Shake-The-Box algorithm (Schanz et al., 2016), resulting in approximately 20,000 identified particle tracks per time step. The final processing step consisted of mapping the particle track data onto a Cartesian grid by spatially averaging over small cells. For this binning procedure, we used 40 x 40 x 40 mm^3 cells with a Gaussian weighing function. An overlap of 75 % was selected to obtain a grid spacing of 10 mm in the resulting velocity fields. The average number of particles used in the binning procedure for each grid point consisted of 30,000 particles for the time-averaged flow fields and around 900 particles for the phase-averaged flow fields.

The measurement setup has many similarities to the one used in (Hoek et al., 2022), where we measured the effect of periodic dynamic induction control with collective pitch on a turbine wake. Some improvements that were made for the current experiment compared to the previous setup consisted of: 1) A movable construction for the cameras, as opposed to moving the turbine with respect to the jet outlet, which was seen to have some impact on the turbine inflow conditions. 2) Adding a fourth camera and increasing the tomographic angle (i.e., the subtended angle of all cameras with respect to the measurement domain). This resulted in improved reconstruction of the velocity fields and an increased field of view (FOV). 3) Multiple repetitions of the same control action were recorded for improved convergence of the velocity fields. 4) The distance to the HFSB seeder was increased somewhat to reduce its impact on the inflow conditions. 5) The total length of the measurement domain was increased to capture a larger portion of the wake.

Prior to the helix experiments, we measured the flow without any turbines at a distance of 2.5 D downstream of the seeding rake to get an approximation of the inflow conditions at the upstream turbine (T1). The average measured wind speed and TI profiles at a hy-

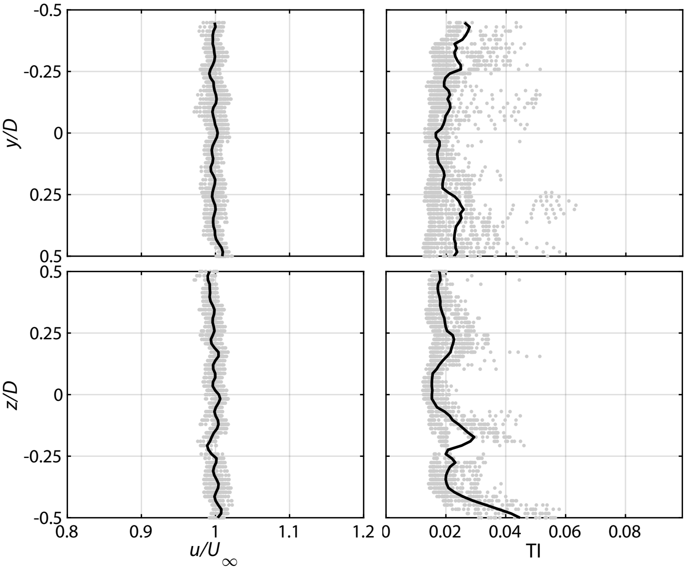

Figure 5.5: Horizontal (y) and vertical (z) profiles of the inflow obtained without the presence of a turbine. The grey dots indicate the flow measurements at different heights or widths, while the black lines represent the flow profiles averaged over all heights or widths. Note that not all parts of the measurement volume were seeded sufficiently with flow tracers, due to some blocked channels of the seeding rake.

pothetical rotor plane are given in Figure 5.5. Both the horizontal and vertical velocity profiles are seen to be centered around the specified inflow speed of $U_\infty = 5\,\mathrm{m\,s^{-1}}$. The TI in both directions slightly exceeded the earlier specified level of 2 %, indicating only a marginal increase in turbulence at the inflow of the turbine as a result of the seeding rake. A similar influence of the seeding rake on the flow conditions was reported by Jux et al. (2018).

5.3 Results

The flow fields that are presented in this section only consider the first three test cases from Table 5.1. The fourth test case consisting of the CCW$_{opt}$ helix with larger pitch amplitude had a smaller amount of measurement data, meaning that the resulting flow fields (primarily phase-averaged) are of somewhat lesser quality. For this reason, we decided to omit the flow fields from the analysis, and only consider this test case for some additional analysis of the power performance. Please note when comparing the remaining flow fields of the helix approach, that there is a small difference in average pitch amplitude between CW and CCW actuation, making a one-on-one comparison more difficult.

5.3.1 Time-averaged flow fields

The binning procedure described in Section 5.2 was initially applied to all particle data at once, providing the time-averaged flow fields. The streamwise velocity fields of the turbine operating under different control strategies are shown in Figure 5.6. For the baseline case,

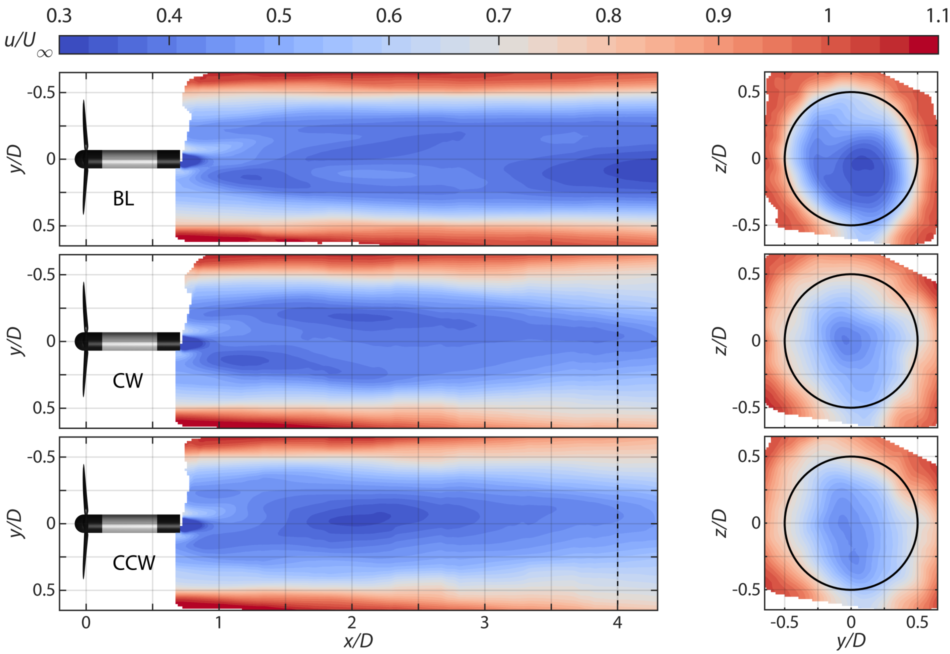

Figure 5.6: Normalized streamwise velocity contours u/U_∞ reconstructed from the time-averaged particle data. The velocity contours at $z/D = 0$ and $x/D = 4$ compare baseline operation with the CW and CCW helix implementations. The dashed line indicates the location of the wake cross-section, while the black circle shows the size of the rotor.

the horizontal cross-section of the turbine wake remains relatively constant. This indicates that there is little recovery in the portion of the wake that was measured. Both helix cases show a clear improvement in wake recovery, marked by a larger wake expansion, but a narrower wake deficit profile. This is most obvious from the vertical cross-section of the wake at $x/D = 4$. Here, we also observe some differences in the shape of the wake between the CW and CCW helix. This difference is believed to be the result of how the shape of the helix (CW or CCW) interacts with the natural rotation of the wake. Further research is needed to define how this interaction affects the shape and recovery of the wake.

An indication of the level of wake recovery or entrainment is given by the flux of mean kinetic energy across the shear layer of the wake. Starting from the transport equation for mean kinetic energy, Cal et al. (2010) showed that the flux of mean kinetic energy due to Reynolds shear stresses is the dominant factor for the entrainment of energy into a turbine wake. An expression for the flux of mean kinetic energy can be obtained using the triple decomposition for a velocity component u (Reynolds and Hussain, 1972):

$$u = \bar{u} + u', \tag{5.2}$$

with $\bar{u}$ the time-averaged velocity component, and u' the fluctuation of the velocity component. The latter term can be further decomposed as

$$u' = \tilde{u} + u_s, \tag{5.3}$$

where $\tilde{u}$ and u_s represent periodic and stochastic fluctuations in the flow, respectively. The flux of mean kinetic energy due to shear stress in the vertical plane is subsequently given by

$$\Phi = -\overline{u'w'}\,\bar{u}. \tag{5.4}$$

The term $\overline{u'w'}$ indicates the time-averaged Reynolds shear stress in the vertical plane, which is computed as

$$\overline{u'w'} = \frac{\sum_{k=1}^{N}(u(t_k)-\bar{u})(w(t_k)-\bar{w})}{N}, \tag{5.5}$$

with $u(t_k)$ and $w(t_k)$ the in-plane velocity components at time instant t_k, for a number of samples N. Entrainment of mean kinetic energy toward the center of the wake can occur when high-speed areas outside the wake move inward ($u' > 0$ and $w' < 0$), or when low-speed areas from inside the wake are ejected outward ($u' < 0$ and $w' > 0$). Hence, positive values of the mean kinetic energy flux correspond to wake recovery.

The improved wake mixing achieved with both helix methods can be seen in Figure 5.7, which shows the entrainment or flux of mean kinetic energy into the region of the wake outlined by $z/D = 0.5$. Looking at the baseline case, we initially see little entrainment across the wake shear layer. Around a distance of $x/D = 2$, one can observe a clear sign flip in the flux of mean kinetic energy. The sign flip is the result of a change in the relative orientation of two interacting tip vortices. This interaction is generally referred to as leapfrogging or vortex pairing. Following the completion of this leapfrogging motion, an increase in kinetic energy entrainment into the wake was seen (Lignarolo et al., 2014). Observing this phenomenon, Lignarolo et al. (2014) concluded that leapfrogging is closely related to the re-energizing of the wake, and that accelerated breakdown of the tip-vortices will result in earlier and thus an increased recovery of the wake velocity.

For both helix cases, Figure 5.7 shows large increases in entrainment, starting earlier than the baseline case and rising even more after $x/D = 2$. Unlike the baseline case, we do not see a clear sign flip in the entrainment indicating the leapfrogging location. This is the combined result of a varying leapfrogging location, and the forced meandering of the wake as a result of the periodic tilt and yaw moments exerted at the rotor, leading to a more diffused entrainment profile. The variation in leapfrogging location was also observed for DIC by collective blade pitch in both simulations (Croce et al., 2022b) and a wind tunnel study (Hoek et al., 2022). In the case of DIC, the periodic thrust variations lead to differences in the strength and expansion of the tip vortices. This increases the reciprocal influence of the helical tip vortices, triggering the mutual-inductance instability mode more aggressively (Sørensen, 2011). As a result, the mixing process in the wake and the resulting re-energization becomes more effective. Similar to DIC, the helix approach alters the strength of vortices that are shed from the blades due to the varying pitch angles, inserting higher levels of instability in the resulting vortex rings. Furthermore, these variations are distributed asymmetrically over the rotor.

Figure 5.7 offered a glance at the magnitude of velocity fluctuations present in the wake for the different test cases. However, given the definition of the time-averaged Reynolds stress from Equation (5.5), it does not distinguish between periodic and random contributions towards the entrainment of energy in the wake. Lignarolo et al. (2015) showed that the net periodic contribution (e.g., from tip vortices) to the transport of energy to the

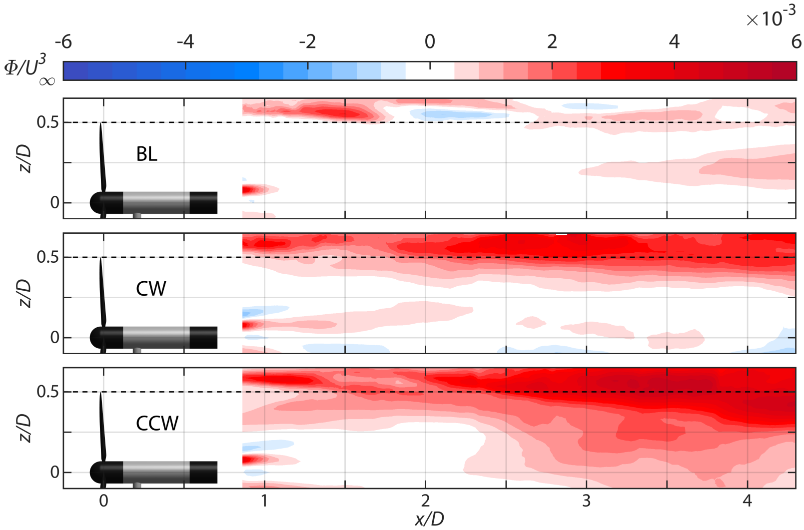

Figure 5.7: Vertical flow field ($y/D = 0$) of the normalized flux of mean kinetic energy into the wake region. Positive (red) values indicate flux of mean kinetic energy in the negative z direction (downward). We are primarily interested in the flux crossing the boundary of the wake, marked by the dashed line. The figure shows a comparison between baseline operation, CW helix, and CCW helix.

wake was nearly zero. Essentially, the tip vortices shield the wake and thereby prevent mixing of the wake with the surrounding flow. Following the completion of the leapfrogging motion, positive entrainment of energy was observed, which was solely dependent on random turbulent fluctuations in the flow. Using phase-averaged PIV measurements, we can study the contribution of turbulent fluctuations to the recovery of the wake in a similar manner for the helix cases.

5.3.2 Phase-averaged flow analysis

The PIV measurements were obtained in a time-resolved manner, and would therefore be suitable for dynamic analysis by themselves, were it not for the fact that the seeding of the flow tracers in the wake is not entirely uniform. As a result, fewer particles are recorded in some areas of the wake which means the measurement convergence might be lower in those parts. This problem can be overcome by phase-averaging the particle data during post-processing. This means that for each phase, more particles are available to each bin on the Cartesian grid, leading to a higher convergence of the velocity components.

For the baseline case, we phase-averaged the data using the measurement of the rotor azimuth angle ψ. The rotor was divided into twelve equal parts of 30°, as seen on the left side of Figure 5.8. Hence, the dynamics of the flow are now represented by twelve consecutive flow fields. On average, over 800 frames (i.e., sets of particle data at a specific time instant) were used for the averaging of each azimuth bin.

Phase-averaging measurement data for the helix approach is less straightforward than in the previous case. Again, the data initially needs to be sorted using the rotor azimuth to retain the flow information from root and tip vortices. However, due to the individual

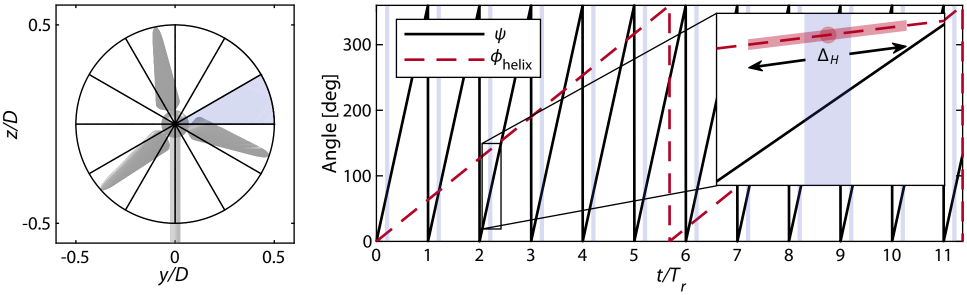

Figure 5.8: Graphical illustration of the phase-averaging procedure in case of a CCW helix implementation. Data is initially binned based on the measurement of the rotor azimuth position ψ, with bin sizes of 30°. Furthermore, measurements of the helix approach are binned based on a second criterion, which is the so-called helix azimuth angle ϕ_{helix}. For a particular rotor azimuth bin, indicated by the blue shaded area, the corresponding average helix azimuth bin is determined. All data that falls within $\pm\Delta_H/2$ of this helix azimuth bin, as well as the previously defined rotor azimuth bin, is collected for phase-averaging. Note that the figure contains a schematic representation of Δ_H, and does not correspond to the actual bin width used in this study. The rotor and helix azimuth angles are indicated as a function of the number of rotor revolutions t/T_r.

pitch action, this only delivers the average performance of the helix over a single rotation as shown in (Heckmeier, 2022). To visualize the dynamic effects of the helix approach, we used a second binning criterion that incorporates the angle between the yaw and tilt moments from Figure 5.3. This angle, referred to as the helix azimuth angle, is given by

$$\phi_{\text{helix}} = \tan^{-1}\left(\frac{\theta_{\text{tilt}}}{\theta_{\text{yaw}}}\right). \tag{5.6}$$

The new binning procedure is visualized on the right-hand side of Figure 5.8, which shows the two sawtooth waves for the rotor azimuth ψ and helix azimuth ϕ_{helix}. Unfortunately, the frequencies of the rotor and the two helix test cases did not match up perfectly. For each CCW cycle of the helix, the rotor completes $f_r/f_e = 5.68$ revolutions. This means that we have to go through three helix cycles before both the rotor and helix azimuth angles return to approximately the same initial conditions. Consequently, the number of bins used for phase-averaging is expressed by f_r/f_e × (*# of helix cycles*) × (*# of azimuth bins*), where the number of helix cycles is chosen to obtain an integer when multiplying with f_r/f_e. For the CW case, this resulted in 168 bins, while 204 bins were obtained for the CCW case due to the slightly lower excitation frequency.

A single rotor azimuth bin is plotted in Figure 5.8 for each consecutive revolution of the rotor by the light blue shaded area. Zooming in on one of these azimuth bins, we see that the range of ϕ_{helix} corresponding to this bin is limited. To increase the number of samples for each bin, an additional variable is introduced representing the width of the helix azimuth bin Δ_H. Investigating the effect of this variable on the resulting velocity fields, a bin width of $\Delta_H = 40°$ was seen to provide converged results. Summarizing the binning procedure: for each consecutive rotor azimuth bin (168 and 204 bins for the CW and CCW cases, respectively), the corresponding helix azimuth angle is determined, after which all frames that belong to this rotor azimuth angle and fall within the bin of the helix azimuth angle are collected from the full set of measurements for the averaging procedure.

On average, around 150 PIV frames were used to obtain the velocity fields of each bin in the case of the helix approach. Converting these PIV frames to velocity fields was done in the same manner as for the time-averaged flow fields.

The phase-averaged velocity fields of the baseline and CW helix cases are compared in Figure 5.9. The wake of the turbine operating under baseline control is shown for a single azimuth bin. This velocity field is similar to its time-averaged counterpart. However, the presence of tip vortices provides some additional detail in the shear layer of the wake. The velocity fields of the CW helix are given at four different phases of the helix cycle. The top view provides a clear picture of the forced meandering caused by the varying yaw and tilt moments. The CW movement of the wake is also clearly seen through the cross-sections at $x/D = 4$. Figure 5.9 also contains isosurfaces of the Q-criterion (Hunt et al., 1988), which were used to reconstruct the tip vortices. A clear difference is observed in the pairing of the tip vortices between the baseline and helix case. While the former shows an organized and gradual leapfrogging process, the latter is quite aggressive and results in an accelerated breakdown of the tip vortices. A detailed analysis of the tip vortex interaction is presented in Section 5.3.4.

The performance of the helix approach compared to baseline operation can already be quantified using the streamwise velocity fields as shown in Figure 5.9. The fraction of available power f_{AP} indicates the amount of power that is available compared to the free stream inflow to a hypothetical turbine in the wake (Vollmer et al., 2016). This performance criterion is given by

$$f_{\mathrm{AP}}(x) = \int_0^{2\pi} \int_0^R u^3(x, r, \psi)/U_\infty^3 r \mathrm{d}r \mathrm{d}\psi, \tag{5.7}$$

with x denoting the distance downstream, r the radial distance measured from the rotor center, and azimuth angle ψ. Figure 5.10 presents the f_{AP} for each of the different test cases from Table 5.1. In the figure, the CCW helix implementation with an average amplitude of $A_\theta = 2.4^\circ$ is referred to as CCW$_{opt}$. All three helix implementations initially see similar levels of available power in the wake, though below baseline operation. Under baseline operation the power decreases at a slower rate until it settles to a near-constant value around $x/D = 2$, showing no signs of recovery in the wake domain that was measured. The CW and CCW implementations reach their minimum level between $x/D = 1.5$ and $x/D = 2$, after which both start increasing at a similar rate. The variation in power level depending on the different phases in the helix actuation sequence due to the horizontal and vertical movement of the wake is also visualized by the shaded areas. The CW method was able to reach a slightly higher power level, likely as a result of the higher pitch amplitude. If we also compare it to the available power with CCW$_{opt}$, we see an even earlier recovery of the wake ($x/D = 1.5$) and higher power levels further downstream compared to the two other helix cases.

5.3.3 Kinetic energy entrainment

Next, we consider the phase-averaged entrainment into the wake due to shear stresses caused by random fluctuations. This process has been identified as the dominant factor for re-energizing the wake, following the tip vortex breakdown (Lignarolo et al., 2015).

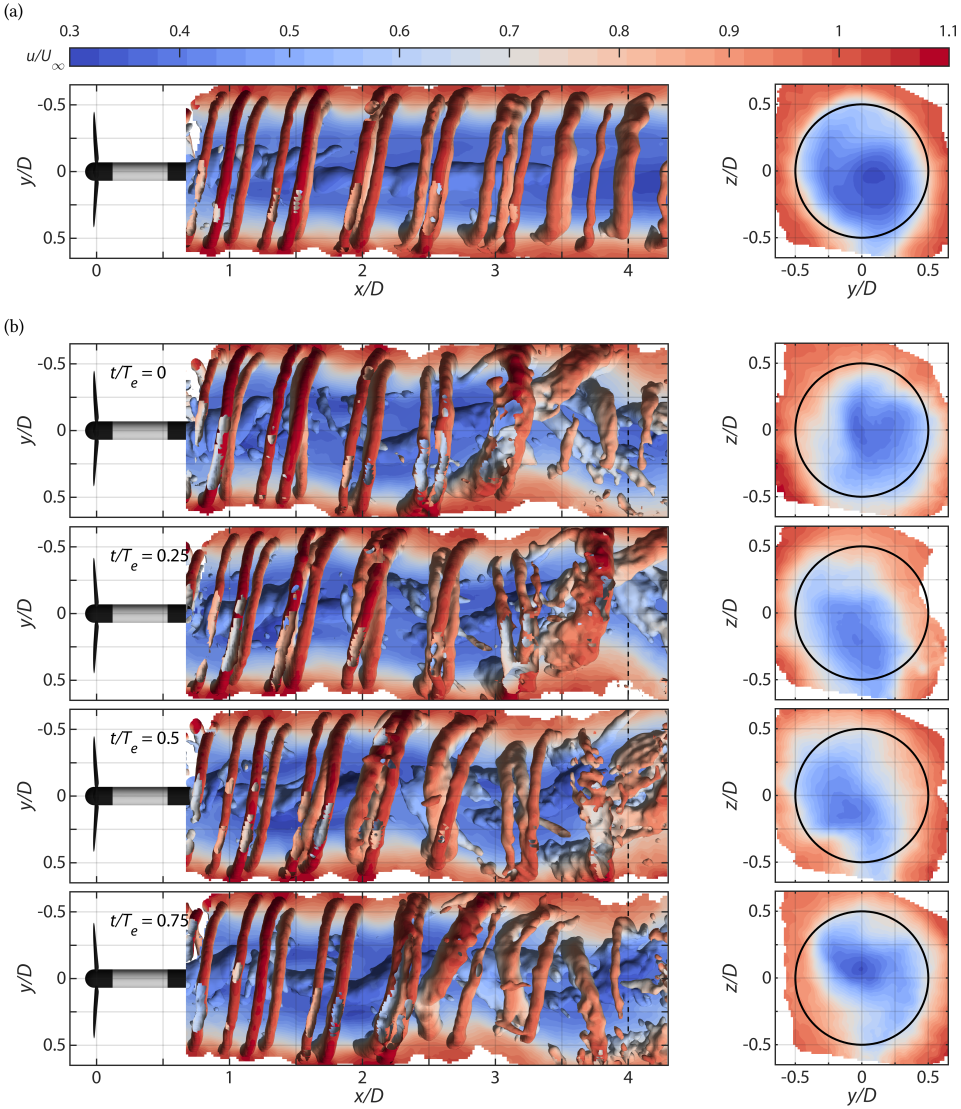

Figure 5.9: Phase-averaged velocity contours u/U_∞ at turbine hub height ($z/D = 0$) and of a cross-section of the wake at $x/D = 4$. The wake of a single azimuth bin of the baseline operation case (a) is compared to multiple phases (bins) of the CW helix cycle (b). Isosurfaces of the Q-criterion, with $Q = 30$, visualize the tip vortices and their interaction downstream.

The phase-averaged Reynolds stress in the vertical plane for a single phase ϕ is defined as

$$\langle u_s w_s \rangle_\phi = \frac{\sum_{k=1}^{N} \left(u(t_{k,\phi}) - \langle u \rangle_\phi \right) \left(w(t_{k,\phi}) - \langle w \rangle_\phi \right)}{N}, \tag{5.8}$$

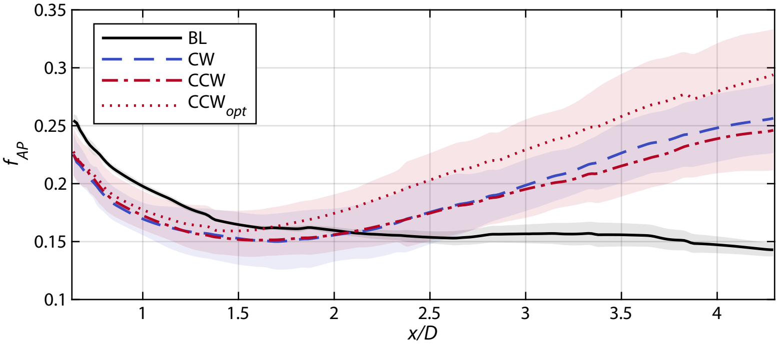

Figure 5.10: Evolution of the fraction of available power over the downstream distance x/D. The f_{AP} is based on the power extracted by a hypothetical turbine rotor using the phase-averaged velocity fields. The shaded areas indicate the variation in power levels over the different phase bins, expressed by $\pm 2\sigma$.

with $\langle u \rangle_\phi$ and $\langle w \rangle_\phi$ the phase-averaged in-plane velocity components, and $t_{k,\phi}$ the sampling time for a velocity component in phase bin ϕ. In this case, the periodic fluctuations are now an inherent part of the phase-averaged velocity $\langle u \rangle_\phi$. However, the phase-averaging procedure adopted in this work did not result in strictly phase-locked measurements, as the phase bins contain a collection of smaller phases.

Multiple phases of the phase-averaged shear stress are visualized in Figure 5.11. The dashed line indicates the edge of the wake, meaning that any red areas crossing this line represent a positive flux of kinetic energy into the wake. The solid black line in the figure indicates the streamwise velocity contour of $\langle u \rangle / U_\infty = 0.5$. The flow from the baseline case shows how saddle points mark the location of subsequent tip vortices. Furthermore, the initial onset of two pairing vortices can be observed just before $x/D = 1.5$. Judging from the sign flip of the shear stress a little further downstream, the leapfrogging motion has just been completed for another pair of vortices at that location. Moving further downstream, we now see more positive contributions of the shear stress crossing over into the turbine wake. The second part of Figure 5.11 shows the phase-averaged Reynolds stress at different phases of the CCW helix cycle, which are marked by the location of the resultant tilt and yaw angles. Considering the first phase that is presented, we initially also see some saddle points indicating the presence of tip vortices. The shear stress quickly becomes more dominant compared to the baseline case as we move further downstream, concentrating in a larger area around $x/D = 2.5$. Moving on to the next frames in the helix cycle, we can observe how more energy is accumulated as the flow moves downstream, and subsequently passes the wake boundary. This area of concentrated shear stress is seen to coincide with a local shifting of the wake, which is marked by the velocity contour.

Figure 5.11 illustrated how the entrainment of kinetic energy as shown by the phase-averaged Reynolds stress varied over different phases of the helix cycle. By averaging these results over all considered phases, we can obtain an expression for the net entrainment of kinetic energy into the wake as a result of random turbulent motions in the flow.

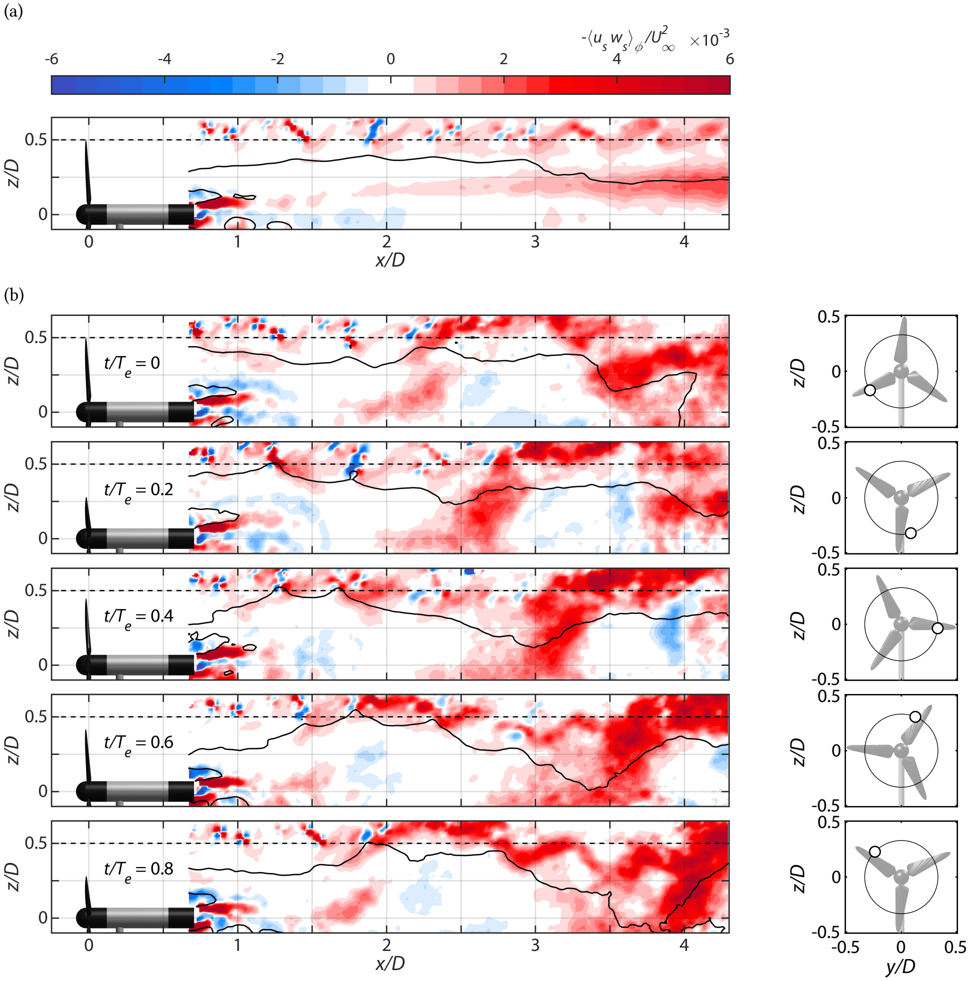

Figure 5.11: Phase-averaged Reynolds stress in the vertical plane ($y/D = 0$) for baseline operation (a) and the CCW helix approach (b). Positive (red) values indicate flux of mean kinetic energy in the negative z direction (downward). We are mostly interested in the energy that crosses the border of the wake shown by the dashed black line. The solid black contour line indicates a streamwise velocity of $\langle u \rangle_\phi / U_\infty = 0.5$. The different phases of the helix approach are illustrated on the right-hand side by the location of the resultant tilt and yaw moment over the rotor plane.

The average Reynolds stress due to random fluctuations over all phases is given by

$$\overline{u_s w_s} = \sum_{\phi=1}^{N_f} \frac{\langle u_s w_s \rangle_\phi}{N_f}, \tag{5.9}$$

for several phases N_f. Multiplying this term with the time-averaged velocity provides the flux of mean kinetic energy due to random fluctuations:

$$\Phi_s = -\overline{u_s w_s}\,\bar{u}. \tag{5.10}$$

Figure 5.12 presents the mean transport of kinetic energy into the wake as a result of random fluctuations for the three considered test cases. Comparing the baseline result to the one from Figure 5.7, we no longer observe a sign flip in the flux. This area marked the leapfrogging location, which was dominated by periodic fluctuations resulting from the tip vortices. These periodic fluctuations do not have a positive net contribution to the recovery of the wake (Lignarolo et al., 2015). This is confirmed by Figure 5.12, which shows that the entrainment is dominated by the region after the leapfrogging occurrence. Both implementations of the helix approach show a clear increase in the kinetic energy flux. The helix can achieve higher levels of mean kinetic energy flux due to the meandering movement of the wake. Furthermore, the entrainment starts at a shorter distance from the rotor plane. We believe this to be the result of enhanced interaction between tip vortices, which will be considered in the next section.

5.3.4 Tip vortex evolution

The effect of the tip vortex instability on the recovery of the wake has been mentioned several times before in this chapter. Using simulations with a vortex-particle-mesh code, Coquelet (2022) showed how the meandering of the wake was triggered differently depending on the resolution of the simulations. At low to intermediate resolution, the wake was destabilized by Kelvin-Helmholtz instabilities, resulting in a meandering wake. When a sufficiently high resolution was used to fully resolve the tip vortices, the manner of destabilization changed to vortex pairing-induced instabilities. The phase-averaged PIV flow fields also provide a good opportunity to study how the helix implementation affects the tip vortex pairing and initializes the destabilization of the wake.

The evolution of the tip vortices is compared for the baseline and CCW helix case

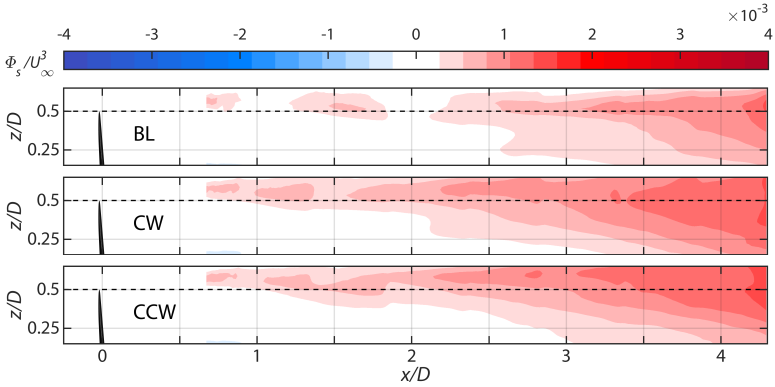

Figure 5.12: Vertical flow field ($y/D = 0$) of the normalized flux of mean kinetic energy due to random fluctuations into the wake region. Positive (red) values indicate flux of mean kinetic energy in the negative z direction (downward). We are primarily interested in the flux crossing the boundary of the wake, marked by the dashed line. The figure shows a comparison between baseline operation, CW helix, and CCW helix.

in Figure 5.13 using the three-dimensional vorticity magnitude $|\omega| = \sqrt{\omega_x^2 + \omega_y^2 + \omega_z^2}$. For each test case, the tip vortices were tracked over time using a least-squares estimate of the displacement δ in x and y direction, based on two consecutive vorticity flow fields. To account for any rotation of the vortices that could not be properly estimated, the least-squares estimates were subsequently corrected with a local peak-finding algorithm. The peak location of the vorticity magnitude was taken as the center of each vortex. For every consecutive phase bin, the positions of each vortex center along with the corresponding magnitude were recorded. Due to the quasi-steady nature of the baseline wake, only a single set of tip vortices needed to be tracked. For the helix cases, a set of vortices was tracked after the completion of each rotor revolution.

When operating the turbine using baseline control, Figure 5.13 shows a very clear evolution of the tip vortices as they convect downstream. At around $x/D = 1.75$, one can observe the leapfrogging of the first vortex pair. The first vortex is subsequently passed by the last trailing vortex, which completes the leapfrogging of the second vortex around $x/D = 3$. While the vortices are seen to interact with each other, there is no clear sign of any instability yet with all the vortices staying more or less intact. The vorticity plots of the CCW helix case show one of the sets that experience the most aggressive mutual inductance. The leapfrogging of the first vortex pair has already taken place before $x/D = 1.5$, which is earlier compared to the baseline case. Comparing the last frame of the two cases, we see that the third vortex has already jumped the first two vortices. On further inspection, we can also notice that the set of vortices has convected less far downstream. This also shows how the helix influences the convection velocity of the vortices over time, which in turn causes sets of vortices to expand outward or contract towards the center of the wake. All previously mentioned phenomena are seen to destabilize the wake at a very fast rate.

One of the responsible factors for the higher mutual inductance of the tip vortices is the strength of the vortices (i.e., stronger vortices will have a larger relative influence, and thus increased interaction). By tracking all sets of vortices over time, we can also see how the strength of each vortex evolves over time (and distance downstream). Figure 5.14 presents the average vorticity magnitude of each trailing vortex as it travels downstream. The resulting plots were obtained by fitting a third-order polynomial on all of the recorded vortex measurements. It is seen how the vorticity magnitude of both helix implementations is initially higher than the baseline case, leading to a stronger interaction initially. However, after the initial interaction between vortices, we observe that the magnitude decreases at a faster rate for the helix. Considering the magnitude of the third vortex, we see a striking difference compared to the first two vortices. For all three test cases, the initial vorticity is almost twice as low compared to the first and second vortices. Although the exact reason behind this difference is unknown, we reckon this is either the result of a slight offset in the pitch angle of one of the blades, or imperfections on the blade surface near the tip.

The tracking measurements also allow us to express the variation in the leapfrogging location of the first vortex pair as a function of the helix azimuth ϕ_{helix}. For each of the vortex pairs, this location was marked when the second vortex moves over 90° with respect to the first vortex (i.e., $x_{v_2}(\phi) > x_{v_1}(\phi)$, with x_{v_i} indicating the streamwise location of a vortex i for phase ϕ). The 90° rotation was identified by Lignarolo et al. (2015) as

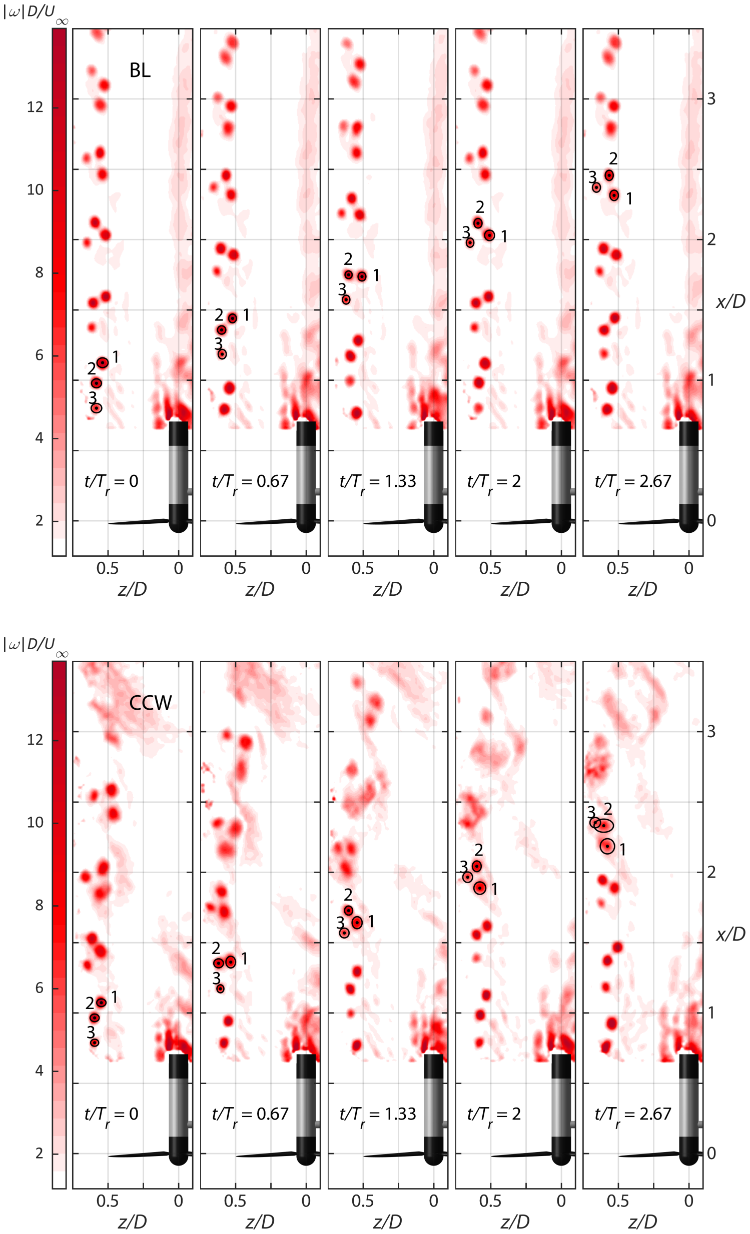

Figure 5.13: Evolution of the tip vortices, expressed by the normalized vorticity magnitude $|\omega|D/U_\infty$, as they travel downstream. The vorticity fields were reconstructed from the phase-averaged measurement data. The figure compares the interaction between the tip vortices for several phases, in the case of baseline operation (top) and the CCW helix approach (bottom). Increased interaction is visible for the helix case, resulting in accelerated diffusion of the tip vortices.

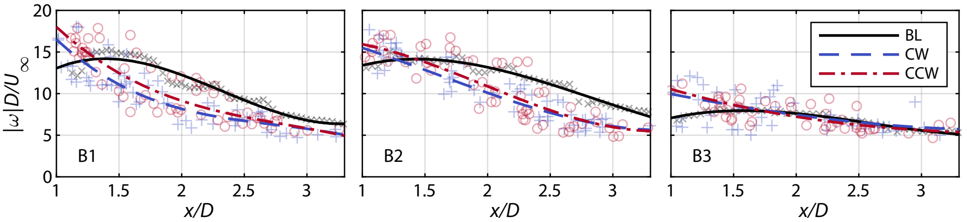

Figure 5.14: Vortex strength expressed by the normalized vorticity magnitude as a function of the displacement in the streamwise direction for three different test cases based on the phase-averaged vorticity fields. Each figure corresponds to a vortex shed by one of the blades. The measurements were fitted to a third-order polynomial to obtain the average vorticity magnitude for each test case. A subset of the measurements to which the polynomials were fitted is included for the baseline (×), CW (+), and CCW (∘) cases.

the wake location that preceded a rapid increase in kinetic energy flux. The resulting locations are presented in Figure 5.15, and compared to the constant leapfrogging location of the baseline case. The respective data points were subsequently fitted to a sine function, which shows how the pairing of the first two vortices evolves as the resultant yaw and tilt moment moves around the rotor plane. It appears that the CW helix has a slightly higher amplitude than the CCW case, probably related to the difference in pitch amplitude between the two cases. Furthermore, we show that on average the helix implementation initializes the leapfrogging at an earlier stage.

5.3.5 Turbine measurements

Besides analyzing the performance of the helix approach based on the flow fields, a more straightforward approach is to investigate the measurements of the turbines themselves. During each PIV recording, the generator power and bending moment at the tower bottom

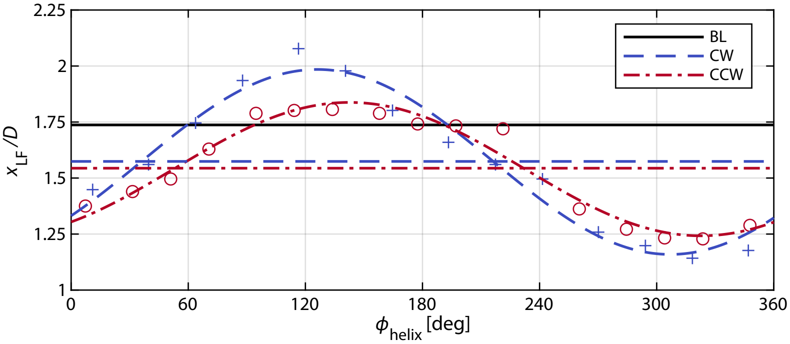

Figure 5.15: Comparison of the leapfrogging location x_{LF}/D in the vertical plane ($y/D = 0$) as a function of the helix azimuth ϕ_{helix}, which is a measure of the position of the combined yaw and tilt moment on the rotor plane. The figure was created using the phase-averaged vorticity fields. A constant x_{LF}/D is shown for the baseline case, while the varying locations for the helix approach are marked by + and ∘ for the CW and CCW cases, respectively. These data points were subsequently fitted to a sine function of the form $a_1 + a_2 \sin(a_3 t + a_4)$, with average offset a_1, amplitude a_2, frequency a_3 and phase offset a_4. The average leapfrogging locations for the CW and CCW cases are indicated by the horizontal lines in matching line styles.

were measured. For each test case, all these measurements were processed to obtain the average and standard deviations. Since each PIV measurement was triggered at the same time instant with respect to the rotor azimuth angle and helix actuation, the periodic components in the generator power and bending moment were maintained, at least for turbine T1.

Figure 5.16 provides the bending moments of both turbines. The periodic excitation of the tilt moment initiated by the helix approach is visible at T1, especially for the CCW helix cases. For all helix cases, the average bending moment experienced at the base of the tower increased. In the case of an ideal implementation of the helix approach, the collective blade pitch angle should remain the same as in the baseline case, and hence a similar average bending moment is expected. The increase in bending moment that we observe at the upstream turbine is possibly the result of the imperfect blade pitch actuation by the swashplate. The bending moment of the second turbine shows a similar response. Again, the CCW helix especially shows the effect of the periodic tilt moment very clearly. While the average bending moment experienced by the downstream turbine is smaller compared to the first turbine, the relative increase is more severe for the second turbine due to the enhanced wind speed.

The average generator power coefficients of both turbines are shown in Figure 5.17 for all test cases. The shaded areas represent the 95% confidence intervals of the measurement variance. We observe that the baseline case is operating at the expected power level, while a significant decrease in power is observed for each helix case. The largest drops in power are seen for the CW and CCW$_{opt}$ cases, which have similar pitching amplitudes of 2.5° and 2.4°, respectively. Measurements from the second turbine show that the helix approach can increase the power downstream by a large amount. In all cases, the original amount of power from the baseline case is more than doubled. As expected, the largest increase in power at T2 is observed for the Helix CCW$_{opt}$ case. Both Figures 5.16 and 5.17 make it apparent, that while large gains in power are possible with the helix implementation, this will come at the cost of increased fatigue loading of some structural components. Another observation is the periodic component present in all power measurements of T1. A closer inspection of the signal showed this as a $2P$ excitation, meaning it corresponds to two times the rotational frequency of the turbine. This $2P$ excitation in the fixed frame can be caused by an offset in pitch angle of one of the blades (Solingen and Wingerden, 2015). This

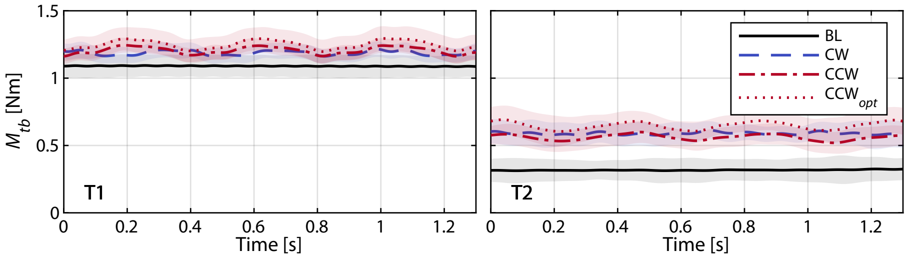

Figure 5.16: Sample of the average measured bending moment at the tower base of turbines T1 and T2. Some variation between different measurements of the same test case was observed. This variation is given by the shaded areas around the mean, indicating $\pm 2\sigma$.

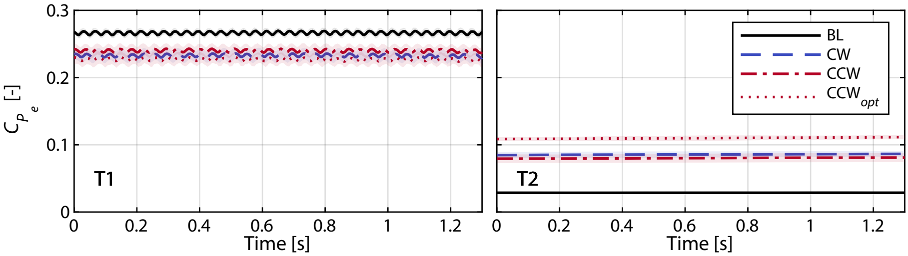

Figure 5.17: Sample of the average measured generator power coefficient of turbines T1 and T2. For both turbines, the power coefficient was determined with respect to the free stream velocity $U_\infty = 5\,\mathrm{m\,s^{-1}}$. Some variation between different measurements of the same test case was observed. This variation is given by the shaded areas around the mean, indicating $\pm 2\sigma$.

was already speculated in the previous section when observing the vorticity magnitude of one of the tip vortices.

Finally, the performance of maximizing the power output for all considered test cases is summarized in Figure 5.18. The figure presents the average power generated by each turbine, as well as the combined power of T1 and T2. Due to the periodic pitching of the blades, T1 loses some aerodynamic efficiency, decreasing the power by more than 10% for each implementation of the helix approach. Compared to previously reported power losses from simulation studies that were in the range of 1–5% (Frederik et al., 2020a; Korb et al., 2021; Coquelet, 2022; Taschner et al., 2023), these decreases are quite severe. This is primarily due to the relatively high sensitivity of the MoWiTO's steady-state power coefficient to changes in pitch angle. The largest drop in power is observed for the CCW_{opt} helix, indicating that the loss in performance can not only be ascribed to the pitch amplitude. Further study is required to find out what else is responsible for the increased performance losses. The power of the second turbine was seen to double for the first two helix approaches, and even triple for the CCW_{opt} helix. Adding up the power of both turbines, we observe that for this particular setup ($5\,D$ spacing with low turbulence), the helix approach was able to increase power by 8.0% for the CW direction, by 8.7% for the CCW direction, and by 15.1% using the CCW_{opt} helix with higher pitch amplitude. Based on the work of Taschner et al. (2023), we believe even higher gains could be achieved when larger pitch amplitudes are applied in combination with the CCW helix. However, when one considers higher levels of atmospheric turbulence, the performance of the helix approach decreases due to the enhanced wake recovery in the baseline case that is associated with increased turbulence (Korb et al., 2023).

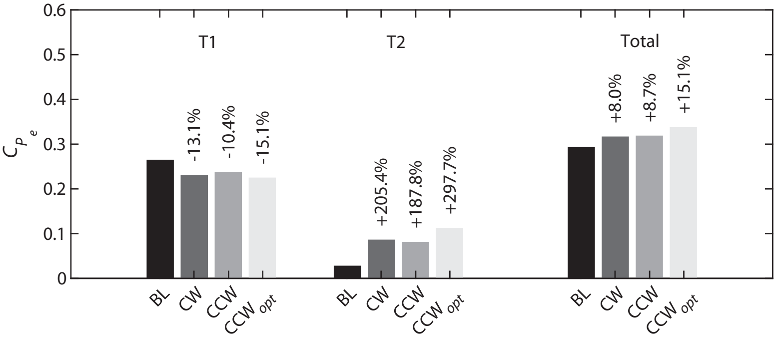

Figure 5.18: Average power production of turbines T1, T2, and the combined sum of both turbines for the different control strategies expressed by the electrical power coefficient C_{P_e}. The power coefficients of both turbines were determined with respect to the free stream inflow velocity $U_\infty = 5\,\mathrm{m\,s^{-1}}$. The total power coefficient is the sum of these two values.

5.4 Conclusions

This chapter presented the implementation of the *helix approach*, a promising control method for maximizing the power output of a wind farm, in a wind tunnel study. The experimental setup consisted of two scaled wind turbines ($D = 0.58\,\mathrm{m}$) spaced $5\,D$ apart in front of an open jet. The upstream turbine was modified with a swashplate typically used for helicopter controls, allowing the turbine to mimic dynamic individual pitch control. A tomographic particle image velocimetry setup, using helium-filled soap bubbles as flow tracers, was used to measure the effect of the helix approach on the turbine wake. A comparison was made with a baseline case, which consisted of running the first turbine at the optimal power extraction settings (greedy control). Turbine measurements of the generator power and tower bending moment were collected as well.

The helix approach uses dynamic individual pitch control to create yaw and tilt moments from the rotor plane that are acting on the incoming flow. The resultant moment is then periodically moved over the rotor plane, resulting in a helical velocity profile in the wake. Two types of implementation are possible with the helix, either moving the helical velocity profile in a clockwise or counter-clockwise direction. Previous work on the helix approach was mostly limited to simulation studies. This work contributes to the experimental validation of the control method, which in time may lead to the implementation of this method in the field. Using phase-averaged measurements of the streamwise velocity component, the amount of available power in the wake was determined for all test cases. All helix implementations that were considered showed an earlier and enhanced recovery of the wake, providing more energy for turbines downstream.

Phase-averaged flow fields were also used to investigate the wake recovery mechanism in further detail. Previous studies on the helix approach, as well as dynamic induction control with collective pitch, indicated that the performance of the control framework is related to the leapfrogging or vortex pairing instability of the shed tip vortices. It has been shown that this pairing initializes the breakdown of the tip vortices and is the onset for the re-energization of the wake. The periodic motion of the combined yaw and tilt moment results in tip vortices varying in strength and size, as well as the low-velocity wake being moved in a circular motion. Therefore, the mutual inductance between vortices will also differ depending on time and place. Overall, it is believed these local variations will trigger the breakdown of vortices and destabilization of the wake, which will subsequently result in a forced meandering of the wake. The phase-averaged measurements showed a clear increase in the entrainment of kinetic energy in the wake due to random fluctuations. Furthermore, after tracking the tip vortices over time using the vorticity magnitude, we showed that the average leapfrogging location of the first vortex pair is shortened with the helix approach.

Finally, measurements from both turbines were used to corroborate the enhanced performance of the helix approach compared to normal operation, that was obtained through the flow measurements. The turbine that was used to implement the helix approach did suffer from a loss in aerodynamic efficiency, leading to decreases in power of over 10%. However, these losses were more than made up for by the downstream turbine, enhancing the total power output of the two turbines by as much as 15%. These results are even more promising when one considers that, according to high-fidelity simulation studies, the losses at the first turbine are expected to decrease in the case of utility-scale wind turbines. The measurement results also confirm once more, that the CCW helix is the more effective of the two implementations.

6

Conclusions and recommendations

6.1 Conclusions

Wind farm flow control can be a useful tool for increasing wind farm power efficiency. Three different categories are generally recognized: static induction control, wake steering control, and wake mixing control. This thesis covered each of the different wind farm flow control concepts at their respective stages in the development cycle, to fulfill the goal of this thesis as presented in the introduction:

> **Thesis goal:** Advance the state of the art of wind farm flow control techniques for maximizing wind farm power performance.

To accomplish this goal, the state of the art of different methods was evaluated, and several knowledge gaps were identified. In subsequent chapters, these knowledge gaps were explored in further detail at the hand of four research objectives. The chapters regarding wind farm control methods contained a separate conclusion section, where the results of these studies were discussed. This chapter reiterates these conclusions to evaluate whether the research objectives have been met. Overall, this thesis has shown to contribute to the development of each of the methods that were considered.

Researching each of the available methods provided valuable insights into the positive and negative aspects of each method. SIC showed small increases in performance for very closely spaced turbines, as well as a beneficial impact on the structural loads of both the actuated as well as the downstream turbines. Although the effectiveness of this method for larger turbine distances remains unclear, potential benefits are expected to be small. Wake steering has already proven its merit in field tests, as well as in simulations for large arrays. Improvements mostly focus on the real-time application of this method under time-varying conditions. Although the effect of WSC on structural loads was not considered in this thesis, previous studies have shown that the asymmetric loading of the yawed rotor can lead to an increase in fatigue loading. Dynamic induction control has shown better performance than static induction control, especially for larger distances between turbines. However, the boost in power production comes at the expense of increased structural loading. Additionally, it is still unclear how DIC scales to larger turbine arrays compared to wake steering, which provides an increase in efficiency for each yawed turbine. So far, dynamic individual pitch control has only been applied to a two-turbine array. Consequently, implementation on a larger wind farm is still unknown. Compared to periodic dynamic induction control, higher gains are expected. However, this is achieved through a large increase in pitch activity, resulting in more fatigue damage at the pitch bearings.

In summary, not one of the methods outperforms the others in all scenarios. The most suitable actuation technique is dependent on the situation, which includes the wind farm layout, the level of ambient turbulence, wind direction (full or partial wake overlap), the structural state of the turbine, and immediate grid demands. To counter the negative aspects of each method, it might be desirable to combine multiple methods simultaneously. Above all else, the application of wind farm flow control methods introduces additional degrees of freedom to the operation and design of a wind farm. More detailed conclusions are included in the remainder of this section for each wind farm flow control method.

Static induction control

A field test on an onshore wind farm with closely spaced turbines was recently completed. The measurements from this campaign were analyzed in Chapter 2, in an attempt to meet the following research objective:

Research objective I: Examine the potential of pitch-actuated static induction control for improving wind farm power efficiency in a field test.

Based on the measurement data that was collected and carefully analyzed, several conclusions were drawn:

- Field measurement data showed that static induction control can increase the power production of a 5-turbine array by approximately 3% for a selected range of wind directions and turbulence intensity levels. It should be noted that the turbines were spaced in very close proximity, ranging between 2.3–3.1 D.
- The turbulence intensity levels at several downstream turbines were seen to decrease with SIC. This confirms the positive effect of SIC on wind turbine structural loads, which are directly related to the turbulence intensity level.
- Measurement data was collected and compared for a relatively large range of wind directions (15°), indicating that the wind farm control implementation is robust to small variations in inflow direction.
- The gain in power obtained using SIC was systematically overestimated using the employed simulation model (FarmFlow), indicating the necessity of accurate wake models, especially the near wake, to correctly estimate its benefits. Furthermore, the blade pitch settings that were adopted by the wind farm control were based on an optimization of said wind farm simulation model, indicating that these settings might not have been optimal.

- Extensive statistical analysis of the measurement results was hindered by the relatively small amount of SCADA data. This was partly due to the low probability of favorable ambient conditions, as well as calibration issues of the wind turbine sensors.

Wake steering control

Given that wake steering has been validated in the field, the next steps are to make the concept more robust to the varying conditions it will experience. This includes obtaining realistic estimates of the gain wake steering control can provide to the AEP of a wind farm. The low-fidelity analytical wake models that are generally employed for this purpose are prone to model mismatches, and often do not include dynamic effects. These challenges were considered for the next research objective.

Research objective II: Determine the effect of wind direction variations on the estimated increase in Annual Energy Production with wake steering control.

Chapter 3 presented a case study of a commercial wind farm that has previously been the subject of research on wake steering control. Based on this case study, the following conclusions were provided:

- A framework was presented that can update AEP calculations based on large-eddy simulations, or similar high-fidelity codes. This hybrid approach employs Gaussian process regression, which is a non-parametric modeling approach capable of handling uncertainties in measurements. In this case, uncertainties apply to the effect of eddies and varying wind direction on wind farm power production, as well as the difference in estimates of the analytical wake model and high-fidelity simulations.
- The large eddy simulations incorporated realistic low-frequency variations in wind direction. Despite the static yaw setpoints, wake steering was still able to achieve significant power gains under these varying ambient conditions.
- Applying the presented framework resulted in a 76% increase in the estimated AEP benefit. The overall increase in wind farm efficiency was estimated to be 0.60%. Although this increase might appear insignificant, these gains add up when one considers wind farm capacities in the order of GWs.

Periodic dynamic induction control

Dynamic induction control has previously been validated in a wind tunnel study and showed improved performance compared to static induction control. However, the mechanism that results in accelerated wake breakdown is less well understood. To this end, a third research objective was formulated:

Research objective III: Investigate the mechanism responsible for the accelerated wake breakdown when applying periodic dynamic induction control.

Chapter 4 presented a wind tunnel study where the wake of a turbine operating with DIC was measured using tomographic PIV. The variation in induction was achieved by applying a sinusoidal reference to the pitch controller. Analyzing the wake measurements resulted in the following conclusions:

- The wake of a turbine operating with DIC showed increased wake recovery based on the streamwise velocity fields. The available power in the wake was found to be significantly higher than in the baseline case, where the turbine was operated with greedy control. However, it should be noted that the average induction between the two control strategies was not equal. Furthermore, the enhanced wake recovery was supported by an increase in turbulence intensity.

- Measurements indicated that DIC affects the leapfrogging behavior of tip vortices, changing the location of vortex pairing depending on the induction of the turbine. Wake recovery is related to the breakdown of the blade tip vortices, which shield the wake from the high energy flow surrounding it. With DIC, this breakdown is accelerated, resulting in a faster wake recovery.

Dynamic individual pitch control

Large eddy simulations indicated improved wake mixing with DIPC compared to conventional DIC, while the actuated turbine also experienced smaller losses in power. The research objective given below was determined to take the next step in the development of this method:

Research objective IV: Validate the potential gain in wind farm power efficiency using dynamic individual pitch control (the helix approach) in a wind tunnel environment.

Using a similar setup as in Chapter 4, the wake dynamics were captured. Furthermore, a second wind turbine was placed at a distance of 5 rotor diameters downstream to directly measure the effect of improved wake mixing on power production. The experiment was able to provide several interesting observations:

- A helicopter inspired swashplate mechanism was successfully implemented on a small-scale wind turbine to provide cyclic individual pitch control actions.

- Both clockwise (CW) and counterclockwise (CCW) implementations of the helix approach resulted in more than doubling of the available power in the turbine wake at a distance $x/D = 4$. For similar pitch amplitudes, the CCW helix was found to be more effective than its CW counterpart.

- For a single cross-section of the wake, the leapfrogging location of the tip vortices was seen to undergo a periodic variation, similar to periodic DIC. Unlike DIC, this periodic variation is different around the wake boundary, continuously resulting in new instabilities that trigger the breakdown of the wake.

- Inspecting the flux of mean kinetic energy due to random fluctuations in the flow showed that the recovery process in the wake starts at an earlier stage, and is more effective further downstream compared to greedy control.
- Measurements with two turbines separated by 5 D showed that the combined power production can be increased by as much as 15% with the helix approach in low turbulence conditions. Increasing the pitch amplitude might even lead to higher gains, albeit at the cost of higher structural loads at the tower base, which were seen to increase when the helix was active.

6.2 Recommendations

This thesis has sought to provide new insights into the field of wind farm flow control. In doing so, it also encountered some topics that require additional study. This section contains several recommendations for future research that can aid the further development of wind farm control methods.

- The growing capacity of offshore wind energy requires a more careful balancing of the grid. This is generally achieved by curtailing wind turbine power output. By combining curtailment with static induction control, regulation of the grid can be achieved alongside an optimal balancing of the structural loads of all wind turbines in the farm.
- By incorporating closed-loop control, an additional increase in performance is expected. Ideally, this should also be taken into account for the AEP calculation. Furthermore, a larger variety of ambient conditions should be included in the high-fidelity simulation set to provide a more accurate representation of the conditions at the wind farm site. Finally, the wake steering control framework employed in this thesis only considered positive yaw misalignments. While this results in lower structural loads, an additional boost in performance might be gained when considering negative yaw misalignments as well.
- As mentioned in the previous section, the application of wake mixing control in the case of partial wake overlap has not yet been covered by the literature. This also applies to varying wind conditions. It is recommended to investigate the effect of these variables on the wind farm performance, either through wind tunnel experiments or high-fidelity simulations.
- Accurate dynamic wake models will be required for the implementation of wake mixing control in combination with a closed-loop controller. The PIV measurements of the turbine wake can help further develop such models. This also requires additional wind tunnel experiments with higher levels of turbulent inflow.
- So far, the helix approach has only been applied to a two-turbine array. The next step is to expand high-fidelity simulations to larger wind farms with differences in turbine spacing. Similar simulations for dynamic induction control revealed that it was not beneficial to vary the induction of downstream turbines as well. However, there are some indications that by properly synchronizing the actuation of the downstream turbine with the incoming wake, wake mixing can be further improved.

- After successful validation of DIPC in the wind tunnel, the next step is to implement this method in the field. As part of a tender bid for the offshore wind farm Hollandse Kust Noord in the Dutch North Sea, field tests are expected to take place in the next few years.

- While DIC and DIPC are able to improve the overall power efficiency of a wind farm, the turbines experience higher structural loads in blades and tower, among others. Combining these methods with the load-alleviating properties of SIC might reduce the impact on structural loading, while still achieving power gains. Similar work has previously been done in the case of SIC and WSC.

- The helix approach employs sinusoidal pitch references with a constant phase offset and frequency around the turbine's 1P frequency. Adjusting the shape, phase offset, or frequency of the pitch reference could result in an additional performance increase.

- Co-design of wind farms combines conventional wind farm design optimization with wind farm control technologies. Including the latter might reduce the spacing between turbines, which could reduce cabling costs. Furthermore, structural components can be optimized while considering the impact of wind farm flow control on structural loads.

- Designing a wind farm controller that can focus on different objectives depending on current needs. These objectives include power maximization, load reduction, and providing grid services.

Bibliography

Abraham, A., Dasari, T., and Hong, J. (2019). “Effect of turbine nacelle and tower on the near wake of a utility-scale wind turbine”. *Journal of Wind Engineering and Industrial Aerodynamics* 193, p. 103981. ISSN: 0167-6105. DOI: `10.1016/J.JWEIA.2019.103981`.

Adaramola, M. S. and Krogstad, P. A. (2011). “Experimental investigation of wake effects on wind turbine performance”. *Renewable Energy* 36.8, pp. 2078–2086. ISSN: 0960-1481. DOI: `10.1016/J.RENENE.2011.01.024`.

Aho, J., Buckspan, A., Laks, J., Fleming, P. A., Jeong, Y., Dunne, F., Churchfield, M., Pao, L. Y., and Johnson, K. (2012). “A tutorial of wind turbine control for supporting grid frequency through active power control”. *American Control Conference (ACC)*, pp. 3120–3131. ISSN: 0743-1619. DOI: `10.1109/ACC.2012.6315180`.

Ainslie, J., Hassan, U, Parkinson, H., and Taylor, G. (1990). “A wind tunnel investigation of the wake structure within small wind turbine farms”. *Wind Engineering*, pp. 24–31.

Annoni, J., Gebraad, P., Scholbrock, A., Fleming, P., and van Wingerden, J. W. (2016). “Analysis of axial-induction-based wind plant control using an engineering and a high-order wind plant model”. *Wind Energy* 19.6, pp. 1135–1150.

Archer, C. L. and Vasel-Be-Hagh, A. (2019). “Wake steering via yaw control in multi-turbine wind farms: Recommendations based on large-eddy simulation”. *Sustainable Energy Technologies and Assessments* 33, pp. 34–43. ISSN: 22131388. DOI: `10.1016/j.seta.2019.03.002`.

Barthelmie, R. J., Hansen, K, Frandsen, S. T., Rathmann, O, Schlez, W, Phillips, J, Hassan, G., Rados, U. K., and Zervos, A (2009). “Modelling and Measuring Flow and Wind Turbine Wakes in Large Wind Farms Offshore”. DOI: `10.1002/we.348`.

Barthelmie, R. J., Pryor, S. C., Frandsen, S. T., Hansen, K. S., Schepers, J. G., Rados, K., Schlez, W., Neubert, A., Jensen, L. E., and Neckelmann, S. (2010). “Quantifying the Impact of Wind Turbine Wakes on Power Output at Offshore Wind Farms”. *Journal of Atmospheric and Oceanic Technology* 27.8, pp. 1302–1317. DOI: `10.1175/2010JTECHA1398.1`.

Barthelmie, R. J., Hansen, K. S., and Pryor, S. C. (2013). “Meteorological controls on wind turbine wakes”. *Proceedings of the IEEE* 101.4, pp. 1010–1019. ISSN: 00189219. DOI: `10.1109/JPROC.2012.2204029`.

Bartl, J. and Sætran, L. (2016). “Experimental testing of axial induction based control strategies for wake control and wind farm optimization”. *Journal of Physics: Conference Series* 753.3, p. 032035. ISSN: 1742-6596. DOI: `10.1088/1742-6596/753/3/032035`.

Bastankhah, M. and Porté-Agel, F. (2014). “A new analytical model for wind-turbine wakes”. *Renewable Energy* 70, pp. 116–123. ISSN: 0960-1481. DOI: `10.1016/J.RENENE.2014.01.002`.

Bastankhah, M. and Porté-Agel, F. (2016). “Experimental and theoretical study of wind turbine wakes in yawed conditions”. *Journal of Fluid Mechanics* 806, pp. 506–541.

Bastankhah, M. and Porté-Agel, F. (2019). “Wind farm power optimization via yaw angle control: A wind tunnel study”. *Journal of Renewable and Sustainable Energy* 11.2. 023301. ISSN: 1941-7012. DOI: `10.1063/1.5077038`.

Becker, M., Ritter, B., Doekemeijer, B., Hoek, D. van der, Konigorski, U., Allaerts, D., and Wingerden, J. W. van (2022). “The revised FLORIDyn model: implementation of heterogeneous flow and the Gaussian wake”. *Wind Energy Science* 7.6, pp. 2163–2179. DOI: `10.5194/wes-7-2163-2022`.

Bir, G. (2008). “Multi-blade coordinate transformation and its application to wind turbine analysis”. *46th AIAA Aerospace Sciences Meeting and Exhibit.* DOI: `10.2514/6.2008-1300`.

Boersma, S., Doekemeijer, B., Gebraad, P., Fleming, P., Annoni, J., Scholbrock, A., Frederik, J., and Wingerden, J. W. van (2017). “A tutorial on control-oriented modeling and control of wind farms”. *Proceedings of the American Control Conference (ACC).* DOI: `10.23919/ACC.2017.7962923`.

Boersma, S., Doekemeijer, B., Siniscalchi-Minna, S., and Wingerden, J. W. van (2019). “A constrained wind farm controller providing secondary frequency regulation: An LES study”. *Renewable Energy* 134, pp. 639–652. ISSN: 0960-1481. DOI: `10.1016/j.renene.2018.11.031`.

Boorsma, K. (2015). *Active Wake Control by pitch adjustment. Analysis of field measurements.* Tech. rep. ECN-E–15-042. Energy research Centre of the Netherlands.

Bossanyi, E. and Ruisi, R. (2021). “Axial induction controller field test at Sedini wind farm”. *Wind Energy Science* 6.2, pp. 389–408. DOI: `10.5194/wes-6-389-2021`.

Bossanyi, E. A. (2000). “The Design of closed loop controllers for wind turbines”. *Wind Energy* 3.3, pp. 149–163. ISSN: 1095-4244. DOI: `10.1002/we.34`.

Bot, E. (2015). *FarmFlow validation against full scale wind farms.* Tech. rep. ECN-E--15-045. Energy research Centre of the Netherlands.

Broek, M. J. van den, De Tavernier, D., Sanderse, B., and Wingerden, J. W. van (2022). “Adjoint optimisation for wind farm flow control with a free-vortex wake model”. *Renewable Energy* 201, pp. 752–765. DOI: `10.4121/2027862`.

Brown, K., Houck, D., Maniaci, D., Westergaard, C., and Kelley, C. (2022). “Accelerated Wind-Turbine Wake Recovery Through Actuation of the Tip-Vortex Instability”. *AIAA Journal* 60.5, pp. 3298–3310. DOI: `10.2514/1.J060772`.

Burton, T., Sharpe, D., Jenkins, N., and Bossanyi, E. (2001). *Wind Energy Handbook.* John Wiley & Sons Ltd. ISBN: 0-471-48997-2.

Cal, R. B., Lebrón, J., Castillo, L., Kang, H. S., and Meneveau, C. (2010). “Experimental study of the horizontally averaged flow structure in a model wind-turbine array boundary layer”. *Journal of Renewable and Sustainable Energy* 2.1, p. 013106. DOI: `10.1063/1.3289735`.

Campagnolo, F., Petrović, V., Bottasso, C., and Croce, A. (2016a). “Wind Tunnel Testing of Wake Control Strategies”. *Proceedings of the American Control Conference.* Boston, MA, USA. DOI: `10.1109/ACC.2016.7524965`.

Campagnolo, F., Petrović, V., Bottasso, C. L., and Croce, A. (2016b). “Wind tunnel testing of wake control strategies”. *Proceedings of the American Control Conference* 2016-July, pp. 513–518. ISSN: 07431619. DOI: `10.1109/ACC.2016.7524965`.

Campagnolo, F., Petrović, V., Schreiber, J., Nanos, E. M., Croce, A., and Bottasso, C. L. (2016c). "Wind tunnel testing of a closed-loop wake deflection controller for wind farm power maximization". *Journal of Physics: Conference Series* 753.3. ISSN: 17426596. DOI: `10.1088/1742-6596/753/3/032006`.

Ceccotti, C., Spiga, A., Bartl, J., and Sætran, L. (2016). "Effect of Upstream Turbine Tip Speed Variations on Downstream Turbine Performance". *Energy Procedia* 94, pp. 478–486. ISSN: 1876-6102. DOI: `10.1016/J.EGYPRO.2016.09.218`.

Churchfield, M. J., Lee, S., Michalakes, J., and Moriarty, P. J. (2012). "A numerical study of the effects of atmospheric and wake turbulence on wind turbine dynamics". *Journal of Turbulence* 13.14, pp. 1–32. DOI: `10.1080/14685248.2012.668191`.

Churchfield, M., Fleming, P., Bulder, B., and White, S. (2015). "Wind Turbine Wake-Redirection Control at the Fishermen's Atlantic City Windfarm". *Offshore Technology Conference*. DOI: `10.4043/25644-MS`.

Ciri, U., Rotea, M., Santoni, C., and Leonardi, S. (2016). "Large Eddy Simulation for an array of turbines with extremum seeking control". *Proceedings of the American Control Conference (ACC)*. Boston, MA, USA, pp. 531–536. DOI: `10.1109/ACC.2016.7524968`.

Clayton, B. R. and Filby, P. (1982). "Measured effects of oblique flows and change in blade pitch angle on performance and wake development of model wind turbines". *4th BWEA Wind Energy Conference*.

Coquelet, M. (2022). "Numerical investigation of wind turbine control schemes for load alleviation and wake effects mitigation". PhD thesis. Université Catholique de Louvain.

Corten, G. and Schaak, P. (June 2003). "Heat and Flux: Increase of Wind Farm Production by Reduction of the Axial Induction". *Proceedings of the European Wind Energy Conference (EWEC)*. Madrid, Spain.

Corten, G. and Schaak, P. (Nov. 2004a). "More power and less loads in wind farms". *Proceedings of the European Wind Energy Conference (EWEC)*. London, UK.

Corten, G., Lindenburg, K., and Schaak, P. (2004). "Assembly of energy flow collectors, such as windpark, and method of operation". Pat. WO 2004/011799 A1.

Corten, G. and Schaak, P. (2004b). "Method and installation for extracting energy from a flowing fluid". Pat. WO 2004/111446 A1.

Crespo, A and Hernandez, J (1996). "Turbulence characteristics in wind-turbine wakes". *Journal of Wind Engineering and Industrial Aerodynamics* 61, pp. 71–85. DOI: `https://doi.org/10.1016/0167-6105(95)00033-X`.

Croce, A., Cacciola, S., and Sartori, L. (2022a). "Evaluation of the impact of active wake control techniques on ultimate loads for a 10 MW wind turbine". *Wind Energy Science* 7.1, pp. 1–17. DOI: `10.5194/wes-7-1-2022`.

Croce, A., Cacciola, S., Montero Montenegro, M., Stipa, S., and Praticó, R. (2022b). "A CFD-based analysis of dynamic induction techniques for wind farm control applications". *Wind Energy*. ISSN: 10991824. DOI: `10.1002/WE.2801`.

Damiani, R., Dana, S., Annoni, J., Fleming, P., Roadman, J., Van Dam, J., and Dykes, K. (2018). "Assessment of wind turbine component loads under yaw-offset conditions". *Wind Energ. Sci* 3, pp. 173–189. DOI: `10.5194/wes-3-173-2018`.

Diffenbaugh, N. S. and Barnes, E. A. (2023). "Data-driven predictions of the time remaining until critical global warming thresholds are reached". *Proceedings of the National*

Academy of Sciences of the United States of America 120.6. ISSN: 10916490. DOI: `10.1073/PNAS.2207183120`.

Dijk, M. van, Wingerden, J. W. van, Ashuri, T., and Li, Y. (2017). "Wind farm multi-objective wake redirection for optimizing power production and loads". *Energy* 121, pp. 561–569.

Doekemeijer, B. M. and Storm, R. (2020). *FLORIS repository.* English. `https://github.com/TUDelft-DataDrivenControl/FLORISSE_M`.

Doekemeijer, B. M., Hoek, D. van der, and Wingerden, J. W. van (2020). "Closed-loop model-based wind farm control using FLORIS under time-varying inflow conditions". *Renewable Energy* 156, pp. 719–730. ISSN: 0960-1481. DOI: `10.1016/J.RENENE.2020.04.007`.

Doekemeijer, B. M., Kern, S., Maturu, S., Kanev, S., Salbert, B., Schreiber, J., Campagnolo, F., Bottasso, C. L., Schuler, S., Wilts, F., Neumann, T., Potenza, G., Calabretta, F., Fioretti, F., and Wingerden, J. W. van (2021). "Field experiment for open-loop yaw-based wake steering at a commercial onshore wind farm in Italy". *Wind Energy Science* 6.1, pp. 159–176. ISSN: 23667451. DOI: `10.5194/WES-6-159-2021`.

Doekemeijer, B. M., Wingerden, J. W. van, and Fleming, P. A. (2019). "A tutorial on the synthesis and validation of a closed-loop wind farm controller using a steady-state surrogate model". *Proceedings of the American Control Conference* 2019, pp. 2825–2836. ISSN: 07431619. DOI: `10.23919/ACC.2019.8815126`.

Eurek, K., Sullivan, P., Gleason, M., Hettinger, D., Heimiller, D., and Lopez, A. (2017). "An improved global wind resource estimate for integrated assessment models". *Energy Economics* 64, pp. 552–567. ISSN: 0140-9883. DOI: `10.1016/j.eneco.2016.11.015`.

European Comission (2014). *Technology readiness levels (TRL).* Accessed: 2023-06-03. URL: `https://ec.europa.eu/research/participants/data/ref/h2020/wp/2014_2015/annexes/h2020-wp1415-annex-g-trl_en.pdf`.

Fleming, P., Gebraad, P. M. O., Lee, S., van Wingerden, J. W., Johnson, K., Churchfield, M., Michalakes, J., Spalart, P., and Moriarty, P. (2015). "Simulation comparison of wake mitigation control strategies for a two-turbine case". *Wind Energy* 18(12), pp. 2135–2143. DOI: `https://doi.org/10.1002/we.1810`.

Fleming, P. A., Aho, J., Gebraad, P. M. O., Pao, L. Y., and Zhang, Y. (2016a). "Computational fluid dynamics simulation study of active power control in wind plants". *American Control Conference (ACC)*, pp. 1413–1420. DOI: `10.1109/ACC.2016.7525115`.

Fleming, P. A., Annoni, J., Scholbrock, A. K., Quon, E., Dana, S., Schreck, S., Raach, S., Haizmann, F., and Schlipf, D. (2017a). "Full-scale field test of wake steering". *Journal of Physics: Conference Series* 854.1. DOI: `10.1088/1742-6596/854/1/012013`.

Fleming, P. A., Annoni, J., Shah, J. J., Wang, L., Ananthan, S., Zhang, Z., Hutchings, K., Wang, P., Chen, W., and Chen, L. (2017b). "Field test of wake steering at an offshore wind farm". *Wind Energy Science* 2.1, pp. 229–239. DOI: `10.5194/wes-2-229-2017`.

Fleming, P., Sinner, M., Young, T., Lannic, M., King, J., Simley, E., and Doekemeijer, B. (Dec. 2021). "Experimental results of wake steering using fixed angles". *Wind Energy Science* 6.6, pp. 1521–1531. ISSN: 23667451. DOI: `10.5194/WES-6-1521-2021`.

Fleming, P. et al. (Feb. 2019b). "Initial Results From a Field Campaign of Wake Steering Applied at a Commercial Wind Farm: Part 1". *Wind Energy Science Discussions*, pp. 1–22. DOI: `10.5194/wes-2019-5`.

Fleming, P. et al. (2019a). “Initial results from a field campaign of wake steering applied at a commercial wind farm-Part 1”. *Wind Energ. Sci* 4, pp. 273–285. DOI: `10.5194/wes-4-273-2019`.

Fleming, P. A., Aho, J., Buckspan, A., Ela, E., Zhang, Y., Gevorgian, V., Scholbrock, A., Pao, L., and Damiani, R. (2016b). “Effects of power reserve control on wind turbine structural loading”. *Wind Energy* 19, pp. 453–469.

Fleming, P. A., Aho, J., Buckspan, A., Ela, E., Zhang, Y., Gevorgian, V., Scholbrock, A., Pao, L., and Damiani, R. (Mar. 2016c). “Effects of power reserve control on wind turbine structural loading”. *Wind Energy* 19.3, pp. 453–469. ISSN: 10991824. DOI: `10.1002/WE.1844`.

Fleming, P. A., Gebraad, P. M., Lee, S., van Wingerden, J. W., Johnson, K., Churchfield, M., Michalakes, J., Spalart, P., and Moriarty, P. (2014). “Evaluating techniques for redirecting turbine wakes using SOWFA”. *Renewable Energy* 70, pp. 211–218. ISSN: 09601481. DOI: `10.1016/j.renene.2014.02.015`.

Frandsen, S., Barthelmie, R., Pryor, S., Rathmann, O., Larsen, S., and Højstrup, J. (2006). “Analytical Modelling of Wind Speed Deficit in Large Offshore Wind Farms”. *Wind Energy.* DOI: `10.1002/we.189`.

Frederik, J. A. and Wingerden, J. W. van (2022). “On the load impact of dynamic wind farm wake mixing strategies”. *Renewable Energy* 194, pp. 582–595. ISSN: 0960-1481. DOI: `10.1016/J.RENENE.2022.05.110`.

Frederik, J. A., Doekemeijer, B. M., Mulders, S. P., and Wingerden, J. W. van (2020a). “The helix approach: using dynamic individual pitch control to enhance wake mixing in wind farms”. *Wind Energy.* DOI: `10.1002/we.2513`.

Frederik, J. A., Weber, R., Cacciola, S., Campagnolo, F., Croce, A., Bottasso, C., and van Wingerden, J.-W. (Feb. 2020b). “Periodic dynamic induction control of wind farms: proving the potential in simulations and wind tunnel experiments”. *Wind Energy Science* 5.1, pp. 245–257. ISSN: 2366-7451. DOI: `10.5194/wes-5-245-2020`.

Gebraad, P. M. O., Teeuwisse, F., Wingerden, J. W. van, Fleming, P. A., Ruben, S. D., Marden, J. R., and Pao, L. Y. (2014a). “A data-driven model for wind plant power optimization by yaw control”. *2014 American Control Conference*, pp. 3128–3134. DOI: `10.1109/ACC.2014.6859118`.

Gebraad, P. M. O., Teeuwisse, F., Wingerden, J. W. van, Fleming, P. A., Ruben, S. D., Marden, J. R., and Pao, L. Y. (2014b). “Wind plant power optimization through yaw control using a parametric model for wake effects - a CFD simulation study”. *Wind Energy* 19.1, pp. 95–114. DOI: `10.1002/we.1822`.

Gebraad, P. M. O. and Wingerden, J. W. van (2015). “Maximum power-point tracking control for wind farms”. *Wind Energy* 18.3, pp. 429–447. DOI: `10.1002/we.1706`.

Gebraad, P., Thomas, J. J., Ning, A., Fleming, P., and Dykes, K. (Jan. 2017). “Maximization of the annual energy production of wind power plants by optimization of layout and yaw-based wake control”. *Wind Energy* 20.1, pp. 97–107. ISSN: 10954244. DOI: `10.1002/we.1993`.

Goit, J. P. and Meyers, J. (2015). “Optimal control of energy extraction in wind-farm boundary layers”. *Journal of Fluid Mechanics* 768, pp. 5–50. DOI: `10.1017/jfm.2015.70`.

Grant, I, Parkin, P, and Wang, X (1997). “Optical vortex tracking studies of a horizontal axis wind turbine in yaw using laser-sheet flow visualisation”. *Experiments in Fluids* 23, pp. 513–519. DOI: `https://doi.org/10.1007/s003480050142`.

Heckmeier, F. M. (2022). “Multi-Hole Probes for Unsteady Aerodynamics Analysis”. PhD thesis. Technische Universität München, p. 223.

Hoek, D. van der, Kanev, S., Allin, J., Bieniek, D., and Mittelmeier, N. (2019). “Effects of axial induction control on wind farm energy production - A field test”. *Renewable Energy* 140. ISSN: 18790682. DOI: `10.1016/j.renene.2019.03.117`.

Hoek, D. van der, Kanev, S., and Engels, W. (2018). “Comparison of Down-Regulation Strategies for Wind Farm Control and their Effects on Fatigue Loads”. *Proceedings of the American Control Conference*. Vol. 2018-June. ISBN: 9781538654286. DOI: `10.23919/ACC.2018.8431162`.

Hoek, D. van der, Frederik, J., Huang, M., Scarano, F., Simao Ferreira, C., and Wingerden, J. W. van (2022). “Experimental analysis of the effect of dynamic induction control on a wind turbine wake”. *Wind Energy Science* 7.3, pp. 1305–1320. ISSN: 23667451. DOI: `10.5194/WES-7-1305-2022`.

Houck, D. R. (2022). “Review of wake management techniques for wind turbines”. *Wind Energy* 25.2, pp. 195–220. ISSN: 1099-1824. DOI: `10.1002/WE.2668`.

Howland, M., Lele, S., and Dabiri, J. (2019). “Wind farm power optimization through wake steering”. *Proceedings of the National Academy of Sciences* 116, p. 201903680. DOI: `10.1073/pnas.1903680116`.

Howland, M. F., Bas Quesada, J., José Pena Martínez, J., Palou Larrañaga, F., Yadav, N., Chawla, J. S., Sivaram, V., and Dabiri, J. O. (2022). “Collective wind farm operation based on a predictive model increases utility-scale energy production”. *Nature Energy*. DOI: `10.1038/s41560-022-01085-8`.

Howland, M. F., Bossuyt, J., Martínez-Tossas, L. A., Meyers, J., and Meneveau, C. (2016). “Wake structure in actuator disk models of wind turbines in yaw under uniform inflow conditions”. *Journal of Renewable and Sustainable Energy* 8.4. ISSN: 1941-7012. DOI: `10.1063/1.4955091`.

Hunt, J., Wray, A., and Moin, P. (1988). “Eddies, streams, and convergence zones in turbulent flows”. *Proceedings of the Summer Program (Center for Turbulence Research)*, pp. 193–208.

IEA (2019). *Offshore Wind Outlook 2019*. Tech. rep. Accessed: 2023-06-08. International Energy Agency. URL: `https://www.iea.org/reports/offshore-wind-outlook-2019`.

IEA (2022). *Wind Electricity*. Tech. rep. Accessed: 2023-06-03. International Energy Agency. URL: `https://www.iea.org/reports/wind-electricity`.

International Electrotechnical Commission (IEC) (2005). *IEC 61400-12-1: Wind turbines – Part 12.1: Power performance measurements of electricity producing wind turbines*. Geneva: IEC.

IPCC (2014). *Climate Change 2014: Synthesis Report. Contribution of Working Groups I, II and III to the Fifth Assessment Report of the Intergovernmental Panel on Climate Change*. Tech. rep. Accessed: 2023-06-03. Intergovernmental Panel on Climate Change. URL: `https://archive.ipcc.ch/pdf/assessment-report/ar5/syr/SYR_AR5_FINAL_full_wcover.pdf`.

IPCC (2022). *Climate Change 2022: Mitigation of Climate Change. Contribution of Working Group III to the Sixth Assessment Report of the Intergovernmental Panel on Climate Change.* Tech. rep. Intergovernmental Panel on Climate Change. DOI: `doi:10.1017/9781009157926`.

IPCC (2023). *Climate Change 2023: Synthesis Report. A Report of the Intergovernmental Panel on Climate Change.* Tech. rep. Accessed: 2023-06-03. Intergovernmental Panel on Climate Change. URL: `https://www.ipcc.ch/report/ar6/syr/downloads/report/IPCC_AR6_SYR_LongerReport.pdf`.

Jensen, N. (1983). *A note on wind generator interaction.* Tech. rep. Risø-M-2411. Risø National Laboratory.

Jeon, Y. J., Schneiders, J. F. G., Müller, M., Michaelis, D., and Wieneke, B (2018). "4D flow field reconstruction from particle tracks by VIC+ with additional constraints and multigrid approximation". *Proceedings 18th International Symposium on Flow Visualization.* DOI: `10.3929/ETHZ-B-000279199`.

Jimenez, A., Crespo, A., and Migoya, E. (2009). "Application of a LES technique to characterize the wake deflection of a wind turbine in yaw". *Wind Energy* 13, pp. 559 –572. DOI: `10.1002/we.380`.

Jonkman, J., Butterfield, S., Musial, W., and Scott, G. (2009). "Definition of a 5-MW Reference Wind Turbine for Offshore System Development". *National Renewable Energy Laboratory (NREL).* DOI: `10.2172/947422`.

Jux, C., Sciacchitano, A., Schneiders, J. F. G., and Scarano, F. (2018). "Robotic volumetric PIV of a full-scale cyclist". *Experiments in Fluids* 59.4, p. 74. ISSN: 0723-4864. DOI: `10.1007/s00348-018-2524-1`.

Kanev, S. and Savenije, F. (2015). *Active Wake Control: loads trends.* Tech. rep. Energy research Centre of the Netherlands.

Kanev, S., Savenije, F., and Engels, W. (2018). "Active wake control: an approach to optimize the lifetime operation of wind farms". *Wind Energy* 21, pp. 488–501. DOI: `10.1002/we.2173`.

Katić, I., Højstrup, J., and Jensen, N. (1987). "A Simple Model for Cluster Efficiency". *Proceedings of the European wind energy association conference and exhibition.*

Kazda, J., Zendehbad, M., Jafari, S., Chokani, N., and Abhari, R. (2016). "Mitigating adverse wake effects in a wind farm using non-optimum operational conditions". *Journal of Wind Engineering and Industrial Aerodynamics* 154, pp. 76–83. ISSN: 0167-6105. DOI: `10.1016/j.jweia.2016.04.004`.

Kheirabadi, A. and Nagamune, R. (2019). "A quantitative review of wind farm control with the objective of wind farm power maximization". *Journal of Wind Engineering and Industrial Aerodynamics* 192. DOI: `10.1016/j.jweia.2019.06.015`.

King, J., Fleming, P., King, R., Martínez-Tossas, L. A., Bay, C. J., Mudafort, R., and Simley, E. (2021). "Control-oriented model for secondary effects of wake steering". *Wind Energy Science* 6.3, pp. 701–714. ISSN: 23667451. DOI: `10.5194/WES-6-701-2021`.

Knudsen, T., Bak, T., and Svenstrup, M. (2015). "Survey of wind farm control power and fatigue optimization". *Wind Energy* 18(8), pp. 1333–1351.

Korb, H., Asmuth, H., and Ivanell, S. (June 2023). “The characteristics of helically deflected wind turbine wakes”. *Journal of Fluid Mechanics* 965, A2. ISSN: 0022-1120. DOI: `10.1017/JFM.2023.390`.

Korb, H., Asmuth, H., Stender, M., and Ivanell, S. (2021). “Exploring the application of reinforcement learning to wind farm control”. *Journal of Physics: Conference Series* 1934.1, p. 012022. ISSN: 1742-6596. DOI: `10.1088/1742-6596/1934/1/012022`.

Larsen, G. (1988). *A simple wake calculation procedure.* Risø National Laboratory. ISBN: 9788755014848.

Lhotka, O. and Kyselý, J. (2022). “The 2021 European Heat Wave in the Context of Past Major Heat Waves”. *Earth and Space Science* 9.11. ISSN: 2333-5084. DOI: `10.1029/2022EA002567`.

Lignarolo, L. E. M., Ragni, D., Krishnaswami, C., Chen, Q., Simão Ferreira, C. J., and Bussel, G. J. W. van (Oct. 2014). “Experimental analysis of the wake of a horizontal-axis wind-turbine model”. *Renewable Energy* 70, pp. 31–46. ISSN: 09601481. DOI: `10.1016/j.renene.2014.01.020`.

Lignarolo, L. E., Ragni, D., Scarano, F., Simão Ferreira, C. J., and Bussel, G. J. W. van (2015). “Tip-vortex instability and turbulent mixing in wind-turbine wakes”. *Journal of Fluid Mechanics* 781, pp. 467–493. DOI: `10.1017/JFM.2015.470`.

Marten, D., Paschereit, C. O., Huang, X., Meinke, M., Schröder, W., Müller, J., and Oberleithner, K. (2020). “Predicting wind turbine wake breakdown using a free vortex wake code”. *AIAA Journal* 58.11, pp. 4672–4685. DOI: `10.2514/1.J058308`.

Martínez-Tossas, L. A., Annoni, J., Fleming, P. A., and Churchfield, M. J. (2019). “The aerodynamics of the curled wake: a simplified model in view of flow control”. *Wind Energy Science* 4.1, pp. 127–138. DOI: `10.5194/wes-4-127-2019`.

Medici, D. and Dahlberg, J.-Å. (2003). “Potential improvement of wind turbine array efficiency by active wake control (AWC)”. *European Wind Energy Conference.*

Meyers, J., Bottasso, C., Dykes, K., Fleming, P., Gebraad, P., Giebel, G., Göçmen, T., and Wingerden, J. W. van (2022). “Wind farm flow control: Prospects and challenges”. *Wind Energy Science* 7.6, pp. 2271–2306. ISSN: 23667451. DOI: `10.5194/WES-7-2271-2022`.

Ministerie van Economische Zaken en Klimaat (2022). *Ontwikkelkader windenergie op zee.* Accessed: 2023-06-03. URL: `https://www.rvo.nl/sites/default/files/2022-06/Ontwikkelkader-windenergie-op-zee_juni_2022.pdf`.

Munters, W. and Meyers, J. (2016). “An optimal control framework for dynamic induction control of wind farms and their interaction with the atmospheric boundary layer”. *Philosophical Transactions of the Royal Society of London A: Mathematical, Physical and Engineering Sciences* 375. DOI: `10.1098/rsta.2016.0100`.

Munters, W. and Meyers, J. (2017). “An optimal control framework for dynamic induction control of wind farms and their interaction with the atmospheric boundary layer”. *Philosophical Transactions of the Royal Society of London A: Mathematical, Physical and Engineering Sciences* 375.2091. ISSN: 1364-503X. DOI: `10.1098/rsta.2016.0100`.

Munters, W. and Meyers, J. (2018). “Towards practical dynamic induction control of wind farms: Analysis of optimally controlled wind-farm boundary layers and sinusoidal induction control of first-row turbines”. *Wind Energy Science* 3, pp. 409–425. ISSN: 23667451. DOI: `10.5194/WES-3-409-2018`.

Muscari, C., Schito, P., Viré, A., Zasso, A., Hoek, D. van der, and Wingerden, J. W. van (2022). “Physics informed DMD for periodic Dynamic Induction Control of Wind Farms”. *Journal of Physics: Conference Series* 2265.2, p. 022057. ISSN: 1742-6596. DOI: `10.1088/1742-6596/2265/2/022057`.

National Renewable Energy Laboratory (NREL) (2018). *SOWFA Github repository*. English. `https://github.com/NREL/SOWFA`.

Nilsson, K., Ivanell, S., Hansen, K. S., Mikkelsen, R., Sørensen, J. N., Breton, S. P., and Henningson, D. (2015). “Large-eddy simulations of the Lillgrund wind farm”. *Wind Energy* 18.3, pp. 449–467. ISSN: 10991824. DOI: `10.1002/WE.1707`.

NoordzeeWind (2005-2006). *Wheater data*. English. Accessed: 2019-10-01. URL: `https://www.noordzeewind.nl/en_nl/knowledge/weather-data.html`.

Office of Aeronautical and Space Technology (1991). *Integrated Technology Plan for the Civil Space Program*. Tech. rep. NASA.

Parkin, P., Holm, R. G., and Medici, D. (2001). “The application of PIV to the wake of a wind turbine in yaw”. *4th International Symposium on Particle Image Velocimetry*.

Quick, J., King, J., King, R. N., Hamlington, P. E., and Dykes, K. (2020). “Wake steering optimization under uncertainty”. *Wind Energy Science* 5.1, pp. 413–426. ISSN: 23667451. DOI: `10.5194/WES-5-413-2020`.

Raach, S., Boersma, S., Wingerden, J. W. van, Schlipf, D., and Cheng, P. W. (2017). “Robust lidar-based closed-loop wake redirection for wind farm control”. *Proceedings of the IFAC World Congres 2017*. Vol. 50. 1, pp. 4498–4503.

Rasmussen, C. E. and Williams, C. K. I. (2006). *Rasmussen and Williams - Gaussian Processes for Machine Learning*. ISBN: 026218253X. DOI: `10.1142/S0129065704001899`.

Reynolds, W. C. and Hussain, A. K. (July 1972). “The mechanics of an organized wave in turbulent shear flow. Part 3. Theoretical models and comparisons with experiments”. *Journal of Fluid Mechanics* 54.2, pp. 263–288. ISSN: 14697645. DOI: `10.1017/S0022112072000679`.

Rockel, S., Camp, E., Schmidt, J., Peinke, J., Cal, R. B., and Hölling, M. (2014). *Experimental study on influence of pitch motion on the wake of a floating wind turbine model*. Vol. 7. 4, pp. 1954–1985. ISBN: 4944179839. DOI: `10.3390/en7041954`.

Rotea, M. (2014). “Dynamic programming framework for wind power maximization”. *IFAC Proceedings Volumes*. Vol. 47, pp. 3639–3644. DOI: `10.3182/20140824-6-ZA-1003.02071`.

Rott, A., Doekemeijer, B., Seifert, J. K., Wingerden, J. W. van, and Kühn, M. (2018). “Robust active wake control in consideration of wind direction variability and uncertainty”. *Wind Energy Science* 3.2, pp. 869–882. DOI: `10.5194/wes-3-869-2018`.

Santoni, C., Carrasquillo, K., Arenas-Navarro, I., and Leonardi, S. (2017). “Effect of tower and nacelle on the flow past a wind turbine”. *Wind Energy* 20.12, pp. 1927–1939. DOI: `10.1002/WE.2130`.

Santoni, C., Ciri, U., Rotea, M., and Leonardi, S. (2015). “Development of a high fidelity CFD code for wind farm control”. *Proceedings of the American Control Conference* 2015-July, pp. 1715–1720. ISSN: 07431619. DOI: `10.1109/ACC.2015.7170980`.

Scarano, F., Ghaemi, S., Caridi, G. C. A., Bosbach, J., Dierksheide, U., and Sciacchitano, A. (2015). “On the use of helium-filled soap bubbles for large-scale tomographic PIV in wind tunnel experiments". *Experiments in Fluids* 56.2. DOI: `10.1007/S00348-015-1909-7`.

Schaak, P. (2006). "Heat and Flux: Enabling the Wind Turbine Controller". *Technical Report. Ecn-E-06-017, ECN.*

Schanz, D., Gesemann, S., and Schröder, A. (2016). "Shake-The-Box: Lagrangian particle tracking at high particle image densities". *Experiments in Fluids* 57, p. 70. DOI: `10.1007/s00348-016-2157-1`.

Schepers, J. G. and Van Der Pijl, S. P. (2007). "Improved modelling of wake aerodynamics and assessment of new farm control strategies". *Journal of Physics: Conference Series* 75.1, p. 012039. ISSN: 1742-6596. DOI: `10.1088/1742-6596/75/1/012039`.

Schneiders, J. F. G. and Scarano, F. (2016). "Dense velocity reconstruction from tomographic PTV with material derivatives". *Exp Fluids* 57, p. 139. DOI: `10.1007/s00348-016-2225-6`.

Schottler, J., Hölling, A., Peinke, J., and Hölling, M. (2016). "Design and implementation of a controllable model wind turbine for experimental studies". *Journal of Physics: Conference Series* 753.7. ISSN: 17426596. DOI: `10.1088/1742-6596/753/7/072030`.

Sciacchitano, A. and Scarano, F. (2014). "Elimination of PIV light reflections via a temporal high pass filter". *Measurement Science and Technology* 25.8. DOI: `10.1088/0957-0233/25/8/084009`.

Shahriari, B., Swersky, K., Wang, Z., Adams, R. P., and de Freitas, N. (2016). "Taking the Human Out of the Loop: A Review of Bayesian Optimization". *Proceedings of the IEEE* 104.1, pp. 148–175. DOI: `10.1109/JPROC.2015.2494218`.

Shapiro, C. R., Gayme, D. F., and Meneveau, C. (2018). "Modelling yawed wind turbine wakes: a lifting line approach". *Journal of Fluid Mechanics* 841. DOI: `doi:10.1017/jfm.2018.75`.

Siemens Gamesa Renewable Energy (2019). *Siemens Gamesa now able to actively dictate wind flow at offshore wind locations.* Accessed: 2023-06-02. URL: `https://www.siemensgamesa.com/en-int/newsroom/2019/11/191126-siemens-gamesa-wake-adapt-en`.

Siemens Gamesa Renewable Energy (2023). *SG 14-222-DD offshore wind turbine.* Accessed: 2023-06-03. URL: `https://www.siemensgamesa.com/products-and-services/offshore/wind-turbine-sg-14-222-dd`.

Silva, J. G., Doekemeijer, B., Ferrari, R., and Wingerden, J. W. van (2021). "Active Power Control of Waked Wind Farms: Compensation of Turbine Saturation and Thrust Force Balance". *2021 European Control Conference (ECC)*, pp. 1223–1228. DOI: `10.23919/ECC54610.2021.9655154`.

Simley, E., Fleming, P., and King, J. (2020). "Design and analysis of a wake steering controller with wind direction variability". *Wind Energy Science* 5.2, pp. 451–468. DOI: `10.5194/wes-5-451-2020`.

Solingen, E. van and Wingerden, J.-W. van (2015). "Linear individual pitch control design for two-bladed wind turbines". *Wind Energy* 18.4, pp. 677–697. ISSN: 10991824. DOI: `10.1002/WE.1720`.

Sommer, C., Malz, P., Seehaus, T. C., Lippl, S., Zemp, M., and Braun, M. H. (2020). "Rapid glacier retreat and downwasting throughout the European Alps in the early 21st century”. *Nature Communications* 11.1, pp. 1–10. ISSN: 2041-1723. DOI: `10.1038/s41467-020-16818-0`.

Sørensen, J. N. (2011). “Instability of helical tip vortices in rotor wakes”. *Journal of Fluid Mechanics* 682, pp. 1–4. ISSN: 1469-7645. DOI: `10.1017/JFM.2011.277`.

Spruce, C. J. (1993). “Simulation and Control of Wind farms”. PhD thesis. University of Oxford.

Steinbuch, M., Boer, I. de, Bosora, O., Peters, I., and Ploeg, J. (1988). “Optimal control of wind power plants”. *Journal of Wind Engineering and Industrial Aerodynamics* 27, pp. 237–246. DOI: `https://doi.org/10.1016/0167-6105(88)90039-6`.

Stips, A., Macias, D., Coughlan, C., Garcia-Gorriz, E., and Liang, X. S. (2016). “On the causal structure between CO2 and global temperature”. *Nature Scientific Reports*. DOI: `10.1038/srep21691`.

Taschner, E, Vondelen, A. A. W. van, Verzijlbergh, R, and Wingerden, J. W. van (2023). “On the performance of the helix wind farm control approach in the conventionally neutral atmospheric boundary layer”. *Journal of Physics: Conference Series* 2505, p. 12006. DOI: `10.1088/1742-6596/2505/1/012006`.

UNFCCC (1997). *Kyoto Protocol to the United Nations Framework Convention on Climate Change.* Tech. rep. Accessed: 2023-06-03. United Nations. URL: `https://unfccc.int/sites/default/files/resource/docs/cop3/l07a01.pdf`.

United Nations (2015). *Adoption of the Paris Agreement.* Tech. rep. Accessed: 2023-06-03. United Nations. URL: `https://unfccc.int/sites/default/files/english_paris_agreement.pdf`.

Vali, M, Petrović, V, Boersma, S, Wingerden, J. W. van, and Kühn, M (2017b). “Adjoint-based model predictive control of wind farms: Beyond the quasi steady-state power maximization”. *IFAC World Congress* 50.1, pp. 4510 –4515. DOI: `10.1016/j.ifacol.2017.08.382`.

Vali, M., Petrović, V., Boersma, S., Wingerden, J. W. van, and Kühn, M. (2017a). “Adjoint-based model predictive control of wind farms: Beyond the quasi steady-state power maximization”. *IFAC World Congres.* Vol. 50 (1), pp. 4510–4515.

Vali, M., Petrović, V., Steinfeld, G., Y. Pao, L., and Kühn, M. (2019a). “An active power control approach for wake-induced load alleviation in a fully developed wind farm boundary layer”. *Wind Energy Science* 4.1, pp. 139–161. DOI: `10.5194/wes-4-139-2019`.

Vali, M, Petrović, V, Pao, L. Y., and Kühn, M (2019b). “Lifetime extension of waked wind farms using active power control”. *Journal of Physics: Conference Series* 1256.1, p. 012029. DOI: `10.1088/1742-6596/1256/1/012029`.

Veers, P. et al. (2022). “Grand Challenges in the Design, Manufacture, and Operation of Future Wind Turbine Systems”. *Wind Energy Science Discussions* 2022, pp. 1–102. DOI: `10.5194/wes-2022-32`.

Vollmer, L., Steinfeld, G., Heinemann, D., and Kühn, M. (2016). “Estimating the ake deflection donstream of a ind turbine in different atmospheric stabilities: An les study”. *Wind Energy Science* 1.2, pp. 129–141. DOI: `10.5194/WES-1-129-2016`.

Vondelen, A. A. van, Navalkar, S. T., Kerssemakers, D. R., and Wingerden, J. W. van (May 2023). “Enhanced wake mixing in wind farms using the Helix approach: A loads sensitivity study”. *2023 American Control Conference (ACC)*, pp. 831–836. DOI: `10.23919/ACC55779.2023.10155965`.

Wagenaar, J. and Eecen, P. J. (2011). “Dependence of Power Performance on Atmospheric Conditions and Possible Corrections”. *EWEA*. Brussels.

Wang, C, Campagnolo, F, Sharma, A, and Bottasso, C. L. (2020). “Effects of dynamic induction control on power and loads, by LES-ALM simulations and wind tunnel experiments”. *Journal of Physics: Conference Series* 1618.2, p. 022036. DOI: `10.1088/1742-6596/1618/2/022036`.

Wang, F. and Garcia-Sanz, M. (2018). “Wind farm cooperative control for optimal power generation”. *Wind Engineering* 42.6, pp. 547–560. DOI: `10.1177/0309524X18780377`.

Westergaard, C. H. (2015). *Method for improving large array wind park power performance through active wake manipulation reducing shadow effects.*

Wieneke, B. (2008). “Volume self-calibration for 3D particle image velocimetry”. *Experiments in Fluids 2008 45:4* 45.4, pp. 549–556. ISSN: 1432-1114. DOI: `10.1007/S00348-008-0521-5`.

Wingerden, J. W. van et al. (2020). “Expert Elicitation on Wind Farm Control”. *Journal of Physics: Conference Series* 1618.2, p. 022025. ISSN: 1742-6596. DOI: `10.1088/1742-6596/1618/2/022025`.

World Weather Attribution (2021). *Rapid attribution of heavy rainfall events leading to the severe flooding in Western Europe during July 2021.* Tech. rep. Accessed: 2023-06-05. World Weather Attribution. URL: `https://www.worldweatherattribution.org/wp-content/uploads/Scientific-report-Western-Europe-floods-2021-attribution.pdf`.

Wu, Y. T. and Porté-Agel, F. (2011). “Large-Eddy Simulation of Wind-Turbine Wakes: Evaluation of Turbine Parametrisations”. *Boundary-Layer Meteorology* 138, pp. 345–366. DOI: `10.1007/s10546-010-9569-x`.

Yılmaz, A. E. and Meyers, J. (2018). “Optimal dynamic induction control of a pair of inline wind turbines”. *Physics of Fluids* 30.8. ISSN: 10897666. DOI: `10.1063/1.5038600`.

List of abbreviations

ADM-R Rotating Actuator Disk Model.
AEP Annual Energy Production.
AP Available Power.
AWC Active Wake Control.

CCW counterclockwise.
CFD Computational Fluid Dynamics.
CW clockwise.

DIC Dynamic Inducion Control.
DIPC Dynamic Individual Pitch Control.

FLORIS FLOw Redirection and Induction in Steady-state.
FOV Field of View.

HFSBs Helium-Filled Soap Bubbles.

IPCC Intergovernmental Panel on Climate Change.

LCoE Levelized Cost of Energy.
LES Large Eddy Simulation.
LPT Lagrangian Particle Tracking.

MBC Multi-Blade Coordinate.

NREL National Renewable Energy Laboratory.

OJF Open Jet Facility.

PIV Particle Image Velocimetry.

SIC Static Induction Control.

SOWFA Simulator fOr Wind Farm Applications.

SSPs Shared Socioeconomic Pathways.

STB Shake-The-Box.

TI Turbulence Intensity.

TRL Technology Readiness Level.

VIC+ Vortex-In-Cell Plus.

WMC Wake Mixing Control.

WSC Wake Steering Control.

Acknowledgments

After graduating from TU Delft in 2017, I started working as a control engineer in the wind energy group of the Energy research Centre of the Netherlands (now TNO). Working on research projects together with partners from academia meant that I kept seeing some familiar faces from my old university, such as my MSc supervisor Professor Jan-Willem van Wingerden, and my fellow student Bart Doekemeijer, who had already started his PhD. I had never seriously considered doing a PhD, but after several conversations with Bart, the idea started growing on me. In 2018, when Bart told me a new position might be opening soon, I decided to contact Jan-Willem to let him know I was interested. As it turned out, I was lucky enough to be awarded the position. During the past 5 years, there may have been times I asked myself why I ever wanted to do a PhD, but looking back I do not regret it. For this, my gratitude goes out to Jan-Willem, for giving me the opportunity to pursue a PhD. Thank you as well for all the support and positive encouragement you provided, for being considerate and involved concerning my personal life events, and for ensuring a pleasant working atmosphere for the PhDs in your group. I would also like to thank Bart for sparking my interest in a PhD, and for the countless times you let me bother you with questions on crashing simulations or other software-related issues. Furthermore, my thanks go to my second promotor, Professor Carlos Simão Ferreira, for his supervision related to the wind tunnel experiments, and for always being available for a meeting whenever I wanted to discuss something.

During my PhD, I spent quite some time in the wind tunnels at TU Delft's High Speed Laboratory. For those who are not familiar with wind tunnels, the industrial environment and lack of sunlight can make them appear quite bleak. When you add the frustration of equipment not doing what you want it to do and constant time pressure to this, doing wind tunnel experiments does not sound like much fun. In my experience, having people to help you face the challenges you encounter while doing experiments is a must. The experiments presented in this thesis would not have been as successful, and definitely not as much fun, without the help of some great colleagues. Thank you very much Ming, Joeri, Maarten, Alessandro, Livia, Bert and Daniël! I am also indebted to Edoardo Saredi, Dr. Andrea Sciacchitano, and Prof. Fulvio Scarano for their assistance with the PIV equipment. A lot of work went into the preparation of the scaled wind turbine models prior to the wind tunnel experiments. I cannot thank Will van Geest and Wim Wien enough for all their efforts in this regard.

Besides the obvious hard work, I believe luck plays a big role in the successful completion of a PhD. I was very lucky to be involved with so many people who let me contribute to their work, or who were willing to contribute to mine. A big thank you to all my co-authors, some of whom have already been mentioned, and additionally to Marcus, Mees van Vondelen, Jean, Claudia, Mees Al, Misha, Leif and Stoyan. Furthermore, I would like to thank all the people from DCSC, and especially the wind energy crew, for being great colleagues and making our department a great place to work.

I could not have finished this PhD without the continuous support of my close family. I'm particularly grateful to my parents Henk and Len, and my parents-in-law Gert-Jan and Anja, whose loving support over the years has been invaluable. Finally, my love and thanks go to my wife Claire, who has been my greatest supporter from the start. Thank you for encouraging me to follow this path, and for giving me a positive kick in the butt whenever I needed it. During this period, our lives have also changed considerably. We bought a house, got married, and we now have two beautiful sons, Jules and Lou. Coming home from work every day is a joy, and Jules always puts a smile on my face when he asks if I had fun at work that day. I am very grateful that I get to share all of this with you.

Daan
Vlaardingen, November 2023

Curriculum Vitæ

Daan Cornelis van der Hoek

1990	Born in Rotterdam, The Netherlands

Education

2003–2009	Secondary school - Gymnasium Stedelijk Gymnasium, Schiedam
2010–2014	Bachelor of Science in Mechanical Engineering Delft University of Technology, The Netherlands
2014–2017	Master of Science in Mechanical Engineering Delft University of Technology, The Netherlands
2018–2023	Doctor of Philosophy in Systems & Control Delft University of Technology, The Netherlands *Thesis*: Advances in actuation techniques for wind farm flow control *promotors*: Prof. dr. ir. J.W. van Wingerden and Prof. dr. ir. C.J. Simao Ferreira

Work experience

2016-2017	Graduate Intern Siemens Gamesa Renewable Energy, The Hague
2017-2018	Junior Control Engineer TNO Wind Energy, Petten

List of publications

Journal publications

🗎 8. **Hoek, D. van der**, Van den Abbeele, B., Simao Ferreira, C. J., and Wingerden, J. W. van (2023). “Maximizing wind farm power output with the helix approach – experimental validation and wake analysis using tomographic PIV”. *Wind Energy*, under review. DOI: `https://doi.org/10.48550/arXiv.2306.12849`.

🗎 7. **Hoek, D. van der**, Frederik, J. A., Huang, M., Scarano, F., Simao Ferreira, C. J., and Wingerden, J. W. van (2022). “Experimental analysis of the effect of dynamic induction control on a wind turbine wake”. *Wind Energy Science* 7.3, pp. 1305–1320. DOI: `https://doi.org/10.5194/wes-7-1305-2022`.

🗎 6. **Hoek, D. van der**, Kanev, S., Allin, J., Bieniek, D., and Mittelmeier, N. (2019). “Effects of axial induction control on wind farm energy production - A field test”. *Renewable Energy* 140, pp. 994–1003. DOI: `https://doi.org/10.1016/j.renene.2019.03.117`.

5. Broek, M. J. van den, De Tavernier, D., Hulsman, P., **Hoek, D. van der**, Sanderse, B., and Wingerden, J. W. van (2023). “Free-vortex models for wind turbine wakes under yaw misalignment–a validation study on far-wake effects”. *Wind Energy Science Discussions.* DOI: `https://doi.org/10.5194/wes-2023-57`.

4. Vondelen, A. A. W. van, Iliopoulos, A., Navalkar, S. T., **Hoek, D. van der**, Wingerden, J. W. van (2023). “Modal analysis of an operational offshore wind turbine using enhanced Kalman filter-based subspace identification”. *Wind Energy* DOI: `https://doi.org/10.1002/we.2849`.

3. Becker, M., Ritter, B., Doekemeijer, B., **Hoek, D. van der**, Konigorski, U., and Wingerden, J. W. van (2022). “The revised FLORIDyn model: Implementation of heterogeneous flow and the Gaussian wake”. *Wind Energy Science* 7.6, pp. 2163-2179. DOI: `https://doi.org/10.5194/wes-7-2163-2022`.

2. Vondelen, A. W. van, Navalkar, S. T., Iliopoulos, A., **Hoek, D. van der**, and Wingerden, J. W. van (2022). “Damping identification of offshore wind turbines using operational modal analysis: a review”. *Wind Energy Science* 7.1, pp. 161–184. DOI: `https://doi.org/10.5194/wes-7-161-2022`.

1. Doekemeijer, B., **Hoek, D. van der**, and Wingerden, J. W. van (2020). “Closed-loop model-based wind farm control using FLORIS under time-varying inflow conditions”. *Renewable Energy* 156, pp. 719–730. DOI: `https://doi.org/10.1016/j.renene.2020.04.007`.

Conference papers

11. **Hoek, D. van der**, Sinner, M., Simley, E. L., Pao, L., and Wingerden, J. W. van (2021). “Estimation of the Ambient Wind Field From Wind Turbine Measurements Using Gaussian Process Regression”. *2021 American Control Conference (ACC)*, pp. 558–563. DOI: `https://doi.org/10.23919/ACC50511.2021.9483088`.

🗎 10. **Hoek, D. van der**, Doekemeijer, B., Andersson, L. E., and Wingerden, J. W. van (2020). "Predicting the benefit of wake steering on the annual energy production of a wind farm using large eddy simulations and Gaussian process regression". *Journal of Physics: Conference Series* 1618.2. DOI: https://doi.org/10.1088/1742-6596/1618/2/022024.

9. **Hoek, D. van der**, Kanev, S., and Engels, W. (2018). "Comparison of down-regulation strategies for wind farm control and their effects on fatigue loads". *2018 American Control Conference (ACC)*, pp. 3116–3121. DOI: https://doi.org/10.23919/ACC.2018.8431162.

8. Silva, J. G., **Hoek, D. van der**, Mulders, S.P., Ferrari, R., and Wingerden, J. W. van (2022). "A switching thrust tracking controller for load constrained wind turbines". *2022 American Control Conference (ACC)*, pp. 4230–4235. DOI: https://doi.org/10.23919/ACC53348.2022.9867888.

7. Muscari, C., Schito, P., Viré, A., Zasso, A., **Hoek, D. van der**, and Wingerden, J. W. van (2022). "Physics informed DMD for periodic Dynamic Induction Control of Wind Farms". *Journal of Physics: Conference Series* 2265.2. DOI: https://doi.org/10.1088/1742-6596/2265/2/022057.

6. Engels, W. P., **Hoek, D. van der**, Yu, W., Reyes Baez, R. (2020). "Scheduled state feedback control of a wind turbine". *Journal of Physics: Conference Series* 1618.2. DOI: https://doi.org/10.1088/1742-6596/1618/2/022064.

5. Fontanella, A., Al, M., **Hoek, D. van der**, Liu, Y., Wingerden, J. W. van, and Belloli, M. (2020). "A control-oriented wave-excited linear model for offshore floating wind turbines". *Journal of Physics: Conference Series* 1618.2. DOI: https://doi.org/10.1088/1742-6596/1618/2/022038.

4. Al, M., Fontanella, A., **Hoek, D. van der**, Liu, Y., Belloli, M., and Wingerden, J. W. van (2020). "Feedforward control for wave disturbance rejection on floating offshore wind turbines". *Journal of Physics: Conference Series* 1618.2. DOI: https://doi.org/10.1088/1742-6596/1618/2/022048.

3. Andersson, L. E., Doekemeijer, B., **Hoek, D. van der**, and Wingerden, J. W. van (2020). "Adaptation of engineering wake models using gaussian process regression and high-fidelity simulation data". *Journal of Physics: Conference Series* 1618.2. DOI: https://doi.org/10.1088/1742-6596/1618/2/022043.

2. Doekemeijer, B., **Hoek, D. van der**, and Wingerden, J. W. van (2019). "Model-based closed-loop wind farm control for power maximization using Bayesian optimization: a large eddy simulation study". *2019 IEEE Conference on Control Technology and Applications (CCTA)*, pp. 284–289. DOI: https://doi.org/10.1109/CCTA.2019.8920587.

1. Aubrun, S., Bastankhah, M., Cal, R.B., Conan, B., Hearst, R. J., **Hoek, D. van der**, Hölling, M., Huang, M., Hur, C., Karlsen, B., Neunaber, I., Obligado, M., Peinke, J., Percin, M., Saetran, L., Schito, P., Schliffke, B., Sims-Williams, D., Uzol, O., Vinnes, M.K., Zasso, A. (2019). "Round-robin tests of porous disc models". *Journal of Physics: Conference Series* 1256.1. DOI: https://doi.org/10.1088/1742-6596/1256/1/012004.

🗎 Included in this thesis.